CRANFIELD UNIVERSITY

DIMITRIOS VITLARIS

REAL LIFE CAR AERODYNAMICS

SCHOOL OF AEROSPACE, TRANSPORT AND MANUFACTURING
Computational Fluid Dynamics

MSc
Academic Year: 2017–2018

Supervisor: Dr Panagiotis Tsoutsanis
August 2018

CRANFIELD UNIVERSITY

DIMITRIOS VITLARIS

REAL LIFE CAR AERODYNAMICS

SCHOOL OF AEROSPACE, TRANSPORT AND MANUFACTURING
Computational Fluid Dynamics

MSc
Academic Year: 2017–2018

Supervisor: Dr Panagiotis Tsoutsanis
August 2018

CRANFIELD UNIVERSITY

SCHOOL OF AEROSPACE, TRANSPORT AND MANUFACTURING
Computational Fluid Dynamics

MSc

Academic Year: 2017–2018

DIMITRIOS VITLARIS

Real Life Car Aerodynamics

Supervisor: Dr Panagiotis Tsoutsanis
August 2018

This thesis is submitted in partial fulfilment of the requirements for the degree of MSc.

Abstract

Vehicles have become essential in our lives and they need to satisfy the ever-increasing demands of our society. Fuel efficiency has become the most important factor leading the companies to build light cars as hybrid power units are still in experimental phase. This causes the cars to be more sensitive to aerodynamic loads. Moreover, aerodynamic forces and distributions are obtained in wind tunnel facilities where the conditions are controlled and differ from the real life ones. Another equally important aspect, is the fact that there is a variety of used numerical methods with the most complicated ones being the modelling of the rotation of the wheels. To address this topic, the differences between real-world conditions and wind tunnel ones using different wheel modelling techniques are assessed. The detailed Fastback DriVaer geometry is used and transient simulations utilizing Improved Delayed Detached-Eddy Simulation scheme are conducted in ANSYS Fluent. Only a handful of previous studies involved investigations at realistic cruise speed (100 km/h) while the used wheel modelling methods in this project are considered to be state-of-the-art.

In detail, body forces are obtained using three wheel models with the simplest one being the rotating boundary condition. Flow structures are studied utilizing the Multiple Reference Frames method and the Sliding Mesh technique. The implementation of each model is discussed as certain limitations apply to them. The differences between these models are underlined while the latter two seem to have more similarities even though all results are comparable. Regarding the real-world conditions, statistical data related to highway average vehicle speed provided by the Department for Transport of United Kingdom was taken into account. Also, a real life crosswind gust is implemented with

special attention paid to the turbulent properties.

Initially, three meshes were generated and a grid sensitivity study was undertaken. The overall results showed that the wheel modelling methods affect all parts of the car while the main body is strongly affected by each method accordingly. Differences are obtained at flow structures generated by the wheels while the affect of the models is decreased when real world conditions are applied. At these conditions, an increase of 20% is noticed in the drag while the lift is affected immensely and is increased by 80% approximately. Significant differences are obtained at the flow structures close to the car, such as A pillar vortices, with the overall flow moving to the direction of the gust.

Keywords

Automotive flows; IDDES; rotating; sliding; sheared wind; underhood flows

Contents

List of Figures

List of Tables

List of Abbreviations

CFD	Computational Fluid Dynamics
DES	Detached Eddy Simulation
DDES	Delayed Detached Eddy Simulation
E	Estateback configuration of the DrivAer Model
EARSM	Explicit Algebraic Reynolds Stress Model
F	Fastback configuration of the DrivAer Model
GCI	Grid Convergence Index
IDDES	Improved Delayed Detached Eddy Simulation
LBM	Lattice-Boltzmann Method
LES	Large Eddy Simulation
MRF	Multiple Reference Frames
N	Notchback configuration of the DrivAer Model
PIV	Particle Image Velocimetry
RANS	Reynolds Averaged Navier-Stokes
RWBC	Rotating Wall Boundary Condition
SATM	School of Aerospace, Technology and Manufacturing
SM	Sliding Mesh
URANS	Unsteady Reynolds Averaged Navier-Stokes
VLES	Very Large Eddy Simulation
WMLES	Wall-Modelled Large Eddy Simulation

Acknowledgements

I am sincerely thankful to my family, Hlias, Lina and Pepi, who support me whatever my decisions are and I know they will never stop supporting me. Also, I would like to thank my supervisor Panagiotis Tsoutsanis for his guidance throughout all year and my collegues Enrique, Kamil and Khalid for the strong relationship and cooperation we have developed through this project. Last but not least, I would like to thank Athanasia for the immense patience that showed and the helpful advices/hardware that she gave me.

Chapter 1

Introduction

Road vehicles have been developing since the mid-1800s and they have become elemental and necessary in our lives. Noticeably, their shape is changing often proving the fact that automotive aerodynamics plays a critical role in their development. Vehicle characteristics such as handling, speed, noise, fuel efficiency and driving comfort are strongly affected by aerodynamics and one of the essential goals that automotive engineers try to achieve, is perfecting aerodynamics in current road vehicles according to their needs.

Nowadays, new laws have been introduced restricting the automotive industry to produce environmental friendly vehicles by reducing carbon dioxide emissions and supporting renewable energy resources. Inevitably, fuel efficiency became a top priority and many resources were spent for research and development. Accompanying these restrictions, hybrid power units are evolved while the use of light materials improved fuel consumption even though the cars become more sensitive to aerodynamic forces. However, the key is found in optimizing the flow of the air around the vehicles causing the companies to invest and form appropriate departures.

Experimental methods have been used for developing road vehicles but they are very costly. On the other hand, computers are evolving constantly and can be used for the development process of vehicles. Computational Fluid Dynamics (CFD) methods are used widely to analyse numerically the flow around bodies and it is understandable that many

factors affect the accuracy of a simulation. Different modelling and numerical approaches are utilized to set up the problem in the computer as close to the reality as possible with the least error introduced. So, in order to achieve high accuracy in a simulation, appropriate modelling techniques should be applied.

1.1 Aims and Objectives

The aims of this project are divided into two main categories in which the detailed Fastback DriVaer model is used. Firstly, the differences of wheel modelling techniques are investigated identifying body forces and flow features for each model. Since the wheel rotation plays a crucial role in automotive aerodynamics, the effect of each wheel model to the overall car aerodynamics is highlighted. Moreover, two flow conditions are implemented and the behavior of the car on each one of them is studied thoroughly. In detail, the first flow conditions resemble the ones obtained at a wind tunnel while a real-world crosswind scenario, which comes from a statistical analysis provided by the Department for Transport in United Kingdom, is utilized. Transient simulations are performed for every case while the Multiple Reference Frames and Sliding Mesh methods are used to model the rotation of the wheels. Finally, the results are provided in the form of comparisons of different parameters.

Chapter 2

Literature Review

This section consists of three parts with the first one being a historical report that highlights the progress of automotive vehicles' shapes that have been studied over the years. In detail, simple bodies were initially investigated and they have been reshaped plenty times to become more realistic until a model which represents current production cars was finally designed. The second part concerns the experimental investigations of the DrivAer model that have taken place from 2011 and they are reported with chronological order. Finally, special attention is paid to computational analysis in which previous studies have investigated the influence of the wheels in vehicle aerodynamics while numerical studies related to the Fastback configuration utilizing different modelling techniques are critically discussed.

2.1 Brief History

Automotive aerodynamics took a huge leap forward back in the early 1900s when streamlined cars were initially developed. The innovative Chrysler Airflow which was built in 1935, changed the philosophy of automotive aerodynamics and styling. However, experimental methods and numerical investigations were introduced later with the attention being paid to the understanding of the fundamental flow phenomena around bluff bodies. Morel [1] was the very first to study the flow around a simplified car geometry in 1978

followed by Ahmed [2] and his well-known contribution of the Ahmed body. Since then, numerous studies have investigated the flow structure of the Ahmed body nominating it as a basic test case for numerical approaches. Figure 2.1 shows the geometry of this model indicating the rounded front while four columns support the body to the ground. Also, the angle of the rear part is adjustable allowing the examination of flow features at different slant angles.

According to Le Good et al. in [3], automotive reference models can be distributed into three main categories: **Simple Bodies**, **Basic Car Shapes** and **Variable Geometry Models**. Apart from the Ahmed body, another simple body that is used widely is the NRCC/SAE geometry introduced by SAE as seen in figure 2.2. This specific model combines the average characteristics of North American automobiles but most importantly, diffuser performance investigations were conducted by Cooper et al. [4]. Moreover, the Rover model was designed in the late 1980s and it includes interchangeable back-ends with the backlight angle varying from 0^0 to 40^0. Howel et al. [5] published a breakthrough paper examining the influence of the ground on diffusers using this model.

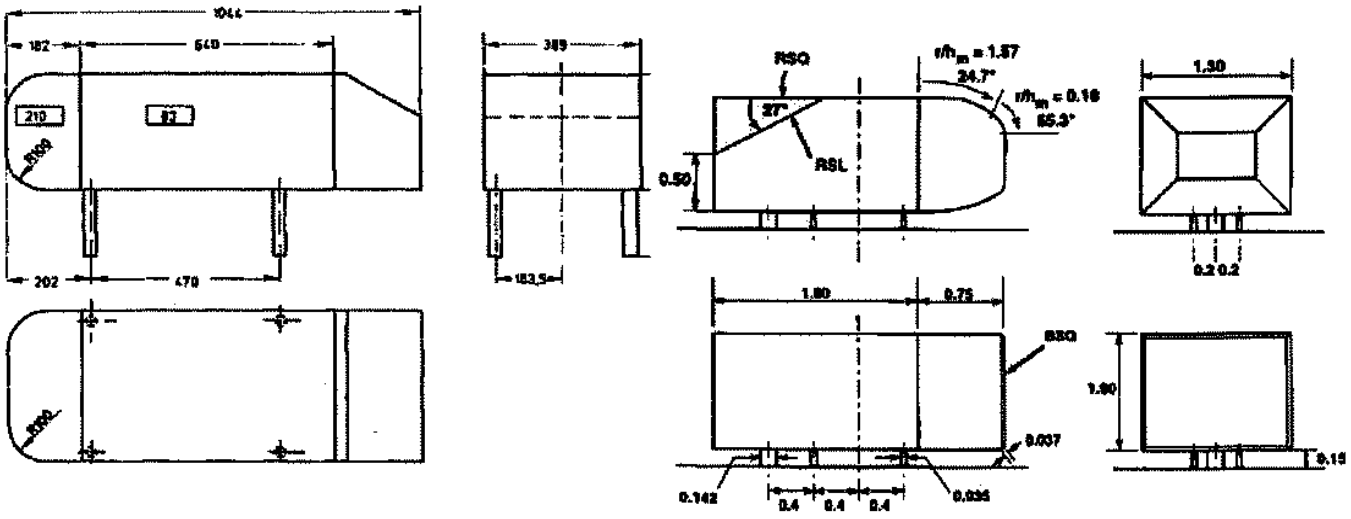

Figure 2.1: Geometry of the Ahmed body [2]

Figure 2.2: Geometry of the NRCC/SAE model [6]

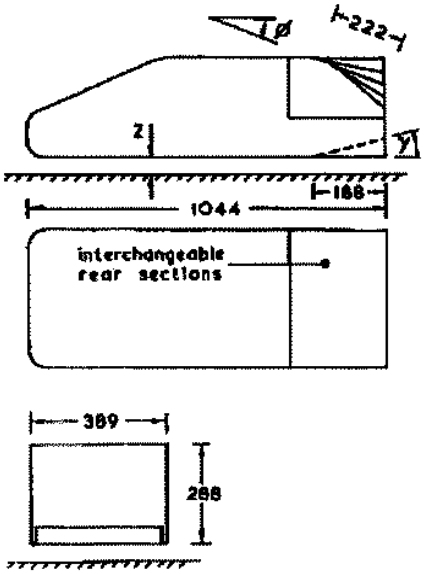

Figure 2.3: Geometry of the Rover model[5]

The second category provides a more realistic approach to the automotive geometry. A basic car geometry that has been used extensively is the MIRA reference car which includes many configurations. Wind tunnels were developed for automotive usage utilizing this model and many investigations have been undertaken such as blockage correction techniques and ground plane simulation techniques. Also, many experimental data are available for the MIRA reference model nominating it as a basic test case for numerical validation.

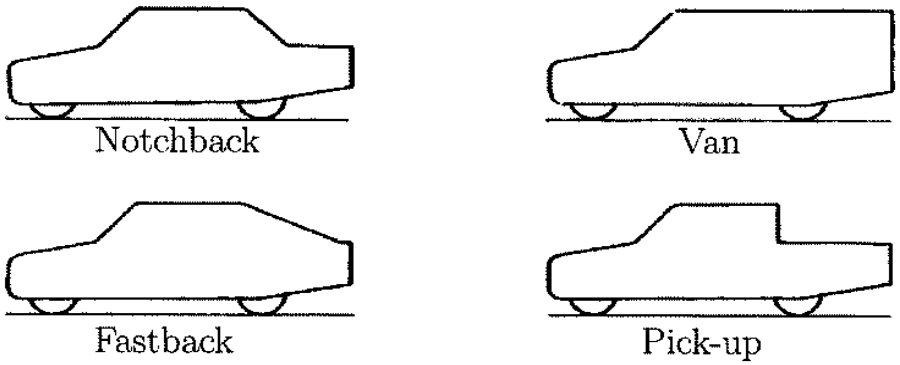

Figure 2.4: MIRA Reference Car [7]

Finally, simple models with interchangeable parts have been designed to study how the flow structure is affected due to geometry changes. The MIRA/ROVER Variable Geometry Model has been used broadly for the investigation of the aerodynamic forces acting on the car according to its geometry changes and the affect of crosswind conditions as well. Another geometry that has been studied is the SAE/PININFARINA model which includes rounded edges and interchangeable back-ends, as seen in figure 2.6, and data from different wind tunnels was compared using this model. It is worth mentioning that the work of Cogotti [8] highlighted the need for more accurate ground simulations.

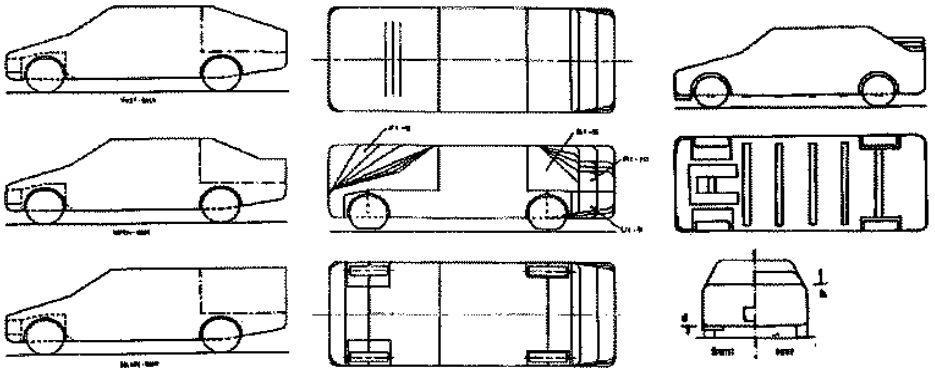

Figure 2.5: MIRA/Rover Variable Geometry Model [5]

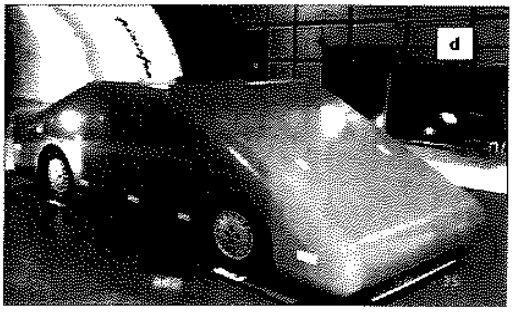

Figure 2.6: Full-Scale SAE Model by Pininfarina [8]

Many simplified models have been designed but the ones that have been studied extensively are mentioned above. Their geometry is simple enabling researchers to manufacture them and design them electronically while they can be set-up easily for wind tunnel testing. Also, their investigation has direct impact to the design of actual automotive cars in spite of their simplicity. Their contribution is significant as their usage helped to understand important aerodynamic characteristics such as:

- Investigation of fundamental flow phenomena
- Development of test techniques
- Wind tunnel calibration
- CFD code validation

Even though many automotive models have been developed and tested, the need for more realistic car models has arose. The flow around simplified geometries is similar to these around production cars but most importantly, the aerodynamic forces, the pitching moment and the yawing moment differ significantly. Also, studies have shown that the luck of basic flow features (e.g. A-pillars) due to their simple geometry, leads to the loss of information as the flow is not completely realistic. Moreover, further studies such as underhood or cooling flows can not be performed as well as the influence of the ground effect. Nowadays, geometries of real production car are not available as they are confidential. However, a new model is becoming famous - the DrivAer model - and it is used widely by the academia and industry.

2.1.1 DrivAer model

Simplified models, such as the Ahmed body and the NRCC/SAE model, are still used for automotive aerodynamics research offering a reasonable experimental and computational effort. However, their shapes are different from the real car geometries and an optimization process is undertaken to make them look like actual cars. After several attempts

having tried to satisfy the above needs, a new realistic generic car model was introduced. Initially, the Institute of Aerodynamics and Fluid Mechanics at the TUM was developed this model with collaboration with their industrial partners. The first appearance of the model was in 2011 by Heft et al [9] aiming to close the gap between real car geometries and simplified ones.

The geometry of the DrivAer model is a combination of an AUDI A4 (front part) and a BMW 3 Series (rear part) and geometries with different configurations, as seen in figure 2.7, is available publicly. Apart from the fact that it offers models with three particular rear ends, two underbody geometries, one smooth and one detailed, geometries with side view mirrors and engine bay are also found to study underhood flows. Additionally, realistic features such as the A- and C-pillars and the wheelhouse region are present proving the fact that the DrivAer model can be used for investigations of mid-class production cars.

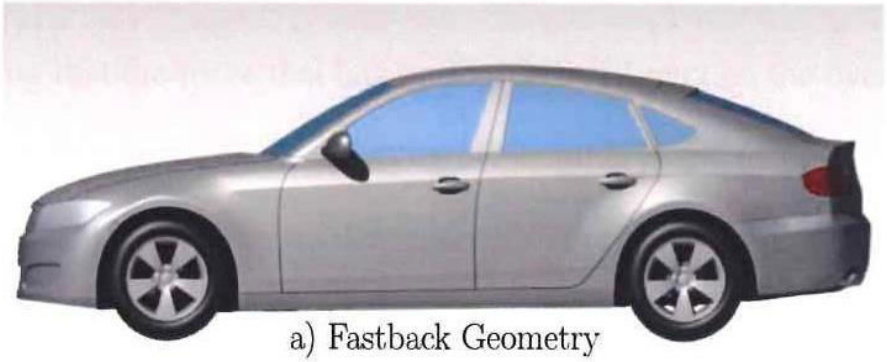

a) Fastback Geometry

b) Notchback Geometry c) Estate Back Geometry

Figure 2.7: DrivAer Model with three different configurations [10]

DriVaer model advantages
Modularity
Open source CAD files
Represents current production cars
Continually expanding database containing experimental and numerical results

Table 2.1: Advantages that DriVaer model has

Overview of DrivAer aerodynamics

As mentioned above, industry is focusing on fuel efficiency which can help them to produce environmental friendly cars. Joseph Katz [11] studied the forces that a vehicle experience in road conditions and his work highlighted the fact that rolling resistance and aerodynamic drag are the most significant forces. However, the first one is greater only at low speeds proving that the force that has undoubtedly impact on the overall performance of a vehicle is the drag force. So, aerodynamic engineers try to optimize the flow over the exterior of the vehicle in order to decrease this force and increase the fuel efficiency. Nonetheless, engineers use unit-less values to quantify certain properties and thus the drag coefficient is used preferably for automotive aerodynamics which quantifies the aerodynamic sleekness of the vehicle configuration. The drag coefficient can be expressed as:

$$C_d = \frac{2D}{\rho u^2 S} \quad , \tag{2.1}$$

where D is the drag force, ρ is the density, u is the vehicle speed and S is the frontal area.

Another crucial force that is generated due to the flow around a vehicle is the lift force. It plays a substantial role to the stability of the vehicle and it is a key factor in racing cars' performance. Racing aerodynamic engineers try to design a car with great stability by achieving negative lift or downforce as is famously known [12]. The design of the underfloor of a car can strongly affect the overall lift force as the pressure difference between lower and upper surfaces causes the generation of the lift force. Once again,

the lift coefficient is preferred rather than the lift force as non-dimensional values are easily handled in the engineering world. The lift coefficient express the amount of the aerodynamic lift created by a vehicle's shape and it is defined in a similar way as the drag coefficient:

$$C_L = \frac{2L}{\rho u^2 S} \quad . \tag{2.2}$$

Multiple zones of reattachment and flow separation characterize the flow around a bluff body moving in close proximity of a static ground. Particular attention has been paid to the rear of the cars where these phenomena occur. During the past years, many studies have investigated the flow structure at the rear of Fastback vehicles but the full picture is not yet understood [13]. Typically, if the angle between the roof and the rear window is small, the flow is attached to the latter due to the smooth transition. Also, this specific area is characterized by low pressure while two counter-rotating longitudinal vortices are developed at the C-pillars starting from the separation point and travelling downstream to form an unsteady wake pattern. At the rear end of the car, a recirculatory region is detected as a result of the shear layers rolling up from the bottom surface.

It is worth mentioning that the aforementioned phenomena are observed only in vigorously generic vehicles with **other flow structures neglected**, such as the influence of the A-pillars that start sideways the windscreen and propagate to the rear. Figure 2.9 shows a more representative flow field for the Fastback DrivAer model as the A-pillar vortices emanate sideways the windscreen and travel over the roof forming a cylindrical vortex structure that affects the C-pillar vortices.

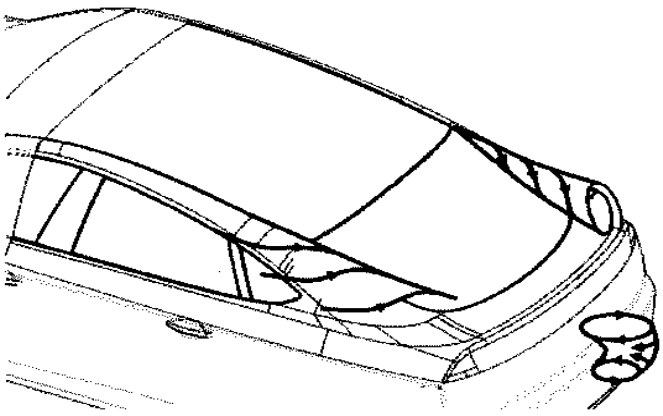

Figure 2.8: Typical flow field observed at the rear of Fastback generic vehicles neglecting other phenomena such as A-pillar vortices [14]

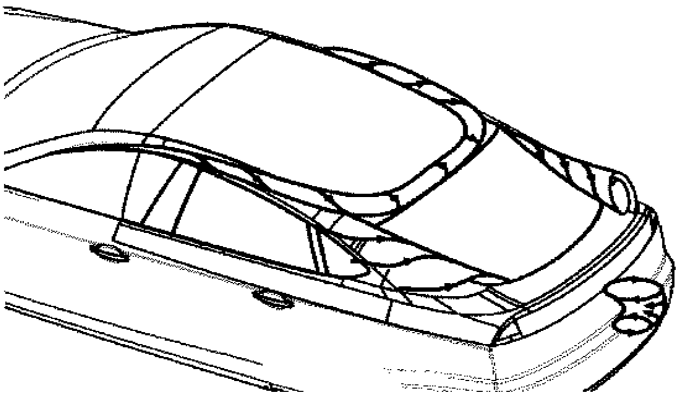

Figure 2.9: More realistic representation of the flow field at the rear of the Fastback DrivAer model [14]

Another important factor that should be mentioned is the fact that all the above vortex structures are unsteady phenomena and are affected strongly by the speed of the vehicle. Generally, the described flow structures are dominant in every Fastback vehicle but the difference is noticed in the unsteadiness of them, e.g. as the Reynolds number increases, the vortices become stronger and their shape and formation point may change.

2.2 Experimental Investigations

In this section, key experimental investigations are discussed with attention being paid to aerodynamic coefficients and flow phenomena. Many configurations were examined and the Reynolds number varies from 1.22 to 4.87 million. Also, some of the experiments were focused on body forces while others on flow structures leading to a huge data base. Table 2.2 shows some of the experimental features while drag and lift coefficients are provided for the Fastback geometry, since this projects investigates this specific configuration.

Heft et al. [10] were the very first to conduct experimental investigations for all DrivAer models and their work was published in 2011. The wind tunnel A of the Institute of Aerodynamics and Fluid Mechanics at the Technical University of Munich (TUM) was used and a system of moving belts was utilized in order to rotate the wheels. Detailed

information about the wind tunnel and the belt system can be found in the paper of Mack et al. [15]. Experiments were undertaken using 1:2.5 scaled models as it has been observed that as the Reynolds number increases, the drag coefficient remains quite stable after a certain value. Results were obtained with the Reynolds number varying from 1.22 $\times 10^6$ to 4.87 $\times 10^6$ which correlates to 10 m/s and 40 m/s velocity respectively. One of the most significant deductions was that the drag coefficient for each model converges towards a specific value as the Reynolds number increases. Also, different configurations were tested (e.g. detailed and smooth underbody, with and without mirrors and wheels) and the influence of various elements was detected using drag counts as measuring system. Finally, the distribution of pressure and pressure coefficient on different parts was evaluated proving that the influence of the ground plays minor role to the pressure distribution at the top of the car while the mirrors have a significant impact on the pressure distribution on the windshield and the side windows. Their studies were continued and a paper was published in 2012, which will be discussed below, but this time emphasis was given to the numerical investigation of the flow around the models.

Moreover, the first experimental results regarding crosswind sensitivity were published by Theissen et al. [16] in 2011. Unsteady time-dependent phenomena and aerodynamic loads were observed and analysed using a 50% scale Notchback DrivAer model under realistic Reynolds number of about 10^7. A yawing motion of +/- 3^0 oscillating at a frequency of 2Hz was applied but it is worth mentioning that a real-world gust was not produced successfully due to the fact that the rear of the car was entering the gust firstly. Their findings showed that as the model was rotating, the reaction of the wake flow was delayed by $\Delta t/T \approx 0.15$. Also, the yaw moment was under-predicted while side force and roll moment were over-predicted confirming previous studies. Finally, the differences between unsteady and quasi steady aerodynamic loads were examined as can be seen in figure 2.10. The study was continued to a second part, published by Wojciak et al. [17] in 2011, in which three different geometries were tested at several wind speeds and aerodynamic loads were observed for each model. The unsteady mechanism that was proposed

in the first part, was confirmed to the second one and the differences between unsteady and quasi-steady moments were examined proving that as the oscillations varied, roll and yaw moment remain constant for both cases while the side force was increased.

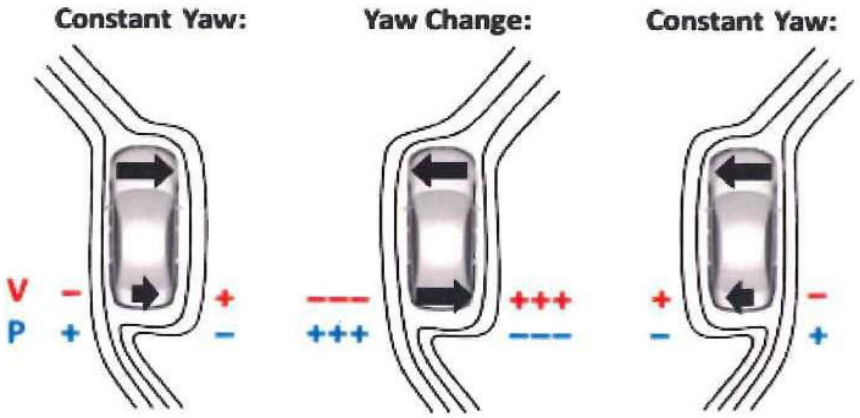

Figure 2.10: Representation of the two-dimensional flow field at constant yaw(left and right) and during a crosswind event(centre) - Initially, the flow is developed and as the crosswind is introduced, the wake flow reacts delayed resulting in higher velocities on the right side. A quasi-steady state is reached when the flow adapts to the oncoming flow [16]

A year later, the first investigation of 40% scaled DrivAer models was undertaken in the upgraded wind tunnel of TUM by Mack et al. [18]. Scaled models are preferably used due to their reduced size and cost. In this study, special attention was paid inside the engine bay where a model heat exchanger was placed in order to study underhood and cooling air flows. Different configurations were examined and the influence of the wheels to the total drag of the vehicle was highlighted. The results showed that the moving ground strongly affects the aerodynamic performance of all models as it causes a reduction of the total drag force, while values of drag coefficient for each geometry were calculated and provided. It is worth mentioning that the drag generated at the rear axis is greater than the one of front axis for all models.

In the following years, three studies were conducted at the same wind tunnel facility using the PIV method to examine the flow features at the wake of Fastback and Notchback models at different yaw angles. The work of Strangfeld et al. [19]. emphasises the unsteady flow structures at the weak of the Fastback DrivAer model, as can be seen in figure 2.11. Also, aerodynamic coefficients were examined under crosswind conditions

at different angles and pressure coefficient distribution was observed at various parts confirming results from previous studies. A separation bubble was detected at $x/L = 0.81$ which was represented by a peak at the pressure coefficient distribution while the lift coefficient reached a minimum value of $C_L = 0.02$ at $\beta = 7.5^0$.

A comparable study was published by Wieser et al. [20] in 2014 in which a Fastback and a Notchback configuration of the DrivAer model were used and aerodynamic coefficients were observed, the pressure distribution at the rear part was analysed with yaw angles up to $\beta = -10^0$ while the flow visualization showed the trace pattern at the rear surfaces highlighting the separation of the flow. For the Fastback geometry, the drag increased about $\Delta C_D = 7.5\%$ with the yaw angle while the minimum value of lift coefficient was $C_L = -0.11$ at $\beta = 4^0$ for $Re_L = 3.2 \cdot 10^6$. A symmetric separated flow field was detected at the rear of the Fastback model while the field was asymmetrical for the Notchback configuration. Both investigations deducted that the drag coefficient increases linearly for yaw angles of $0^0 < \beta < 10^0$ and the pressure recovery at the rear part was observable for every condition.

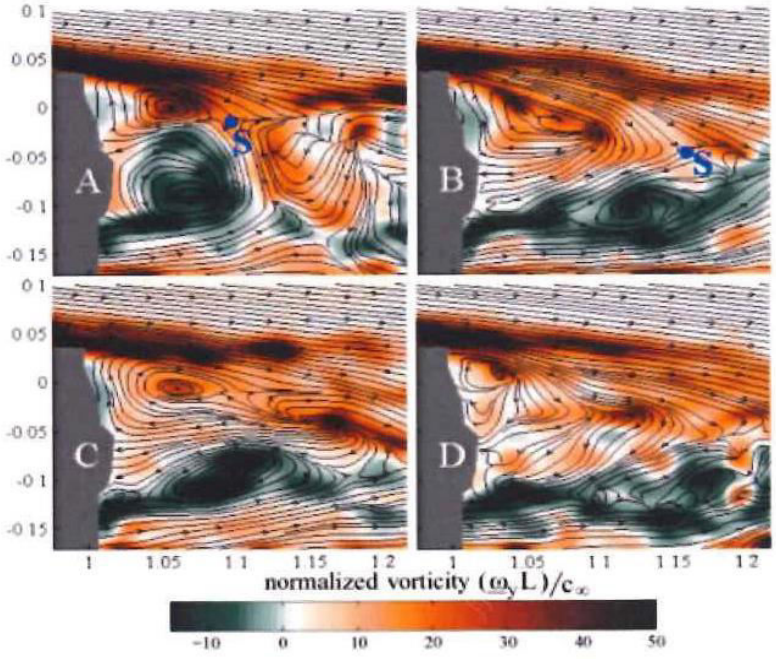

Figure 2.11: PIV pictures of the wake of the Fastback model at zero yaw angle taken randomly - In snapshot A the large green vortex emanating from the underbody is dominant while the opposite case is shown in snapshot B. In these pictures the stagnation point S can be seen as well. The other two snapshots show a more chaotic behaviour [19]

The third study involved the investigation of a 25% scaled Notchback DrivAer model which was equipped with fluidic actuators in order to generate high frequency sweeping jet, as can be seen in figure 2.12. Two inflow conditions were utilized, $\beta = 0^0$ and $\beta = 5^0$, and the influence of the actuators to the wake were examined. For low momentum inputs, the pressure surface at the base and the roof is increased but the pressure difference was negligible at high momentum inputs. However, the drag was decreased for both cases with the largest drop being at the latter case. Meanwhile, the separation bubble at the back windscreen, which is reported from previous studies, vanishes while separation was taken place on the C-pillars.

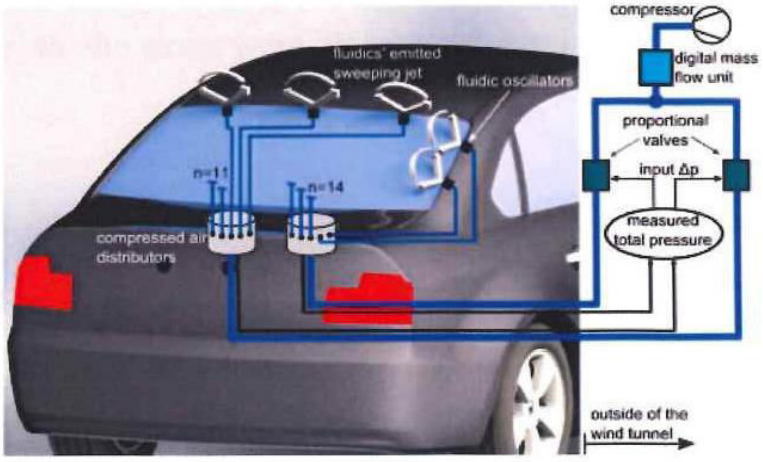

Figure 2.12: Representation of the internal and external system of the active flow control [21]

Experimental investigations were also conducted by Miao et al. [22] and their paper was published in 2015. Upgraded wind tunnel DrivAer models were used with the difference being on the rotation of the wheels as a new suspension system was introduced making the calculation of drag and lift forces possible while the wheels were rotating. Getting rid of the wheel struts, which is a more realistic approach, the influence of the wheels to the overall car performance was examined. Aerodynamic loads were observed for all three DrivAer models creating a more close-truth data base. Overall, their deduction was that the wheel struts lead to 4 lift counts to all configurations and 4 drag counts to the Fastback configuration.

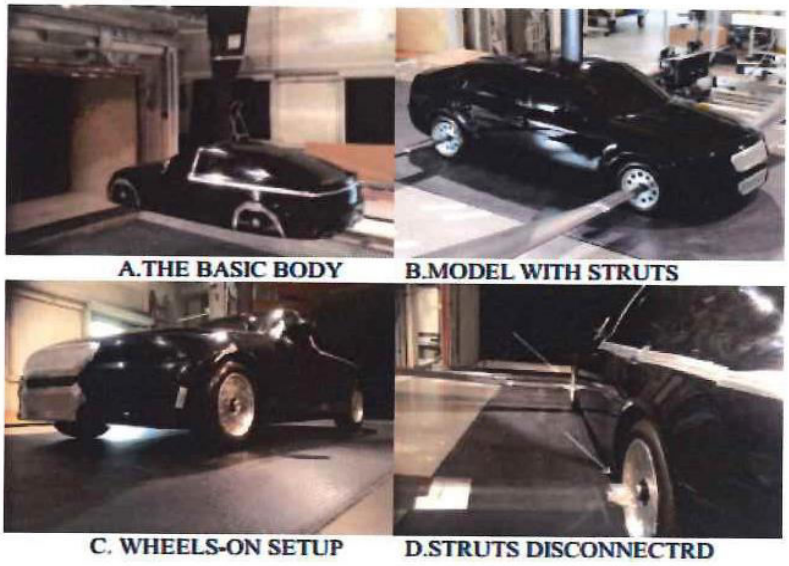

Figure 2.13: Four different experimental set up - The basic vehicle was used in wind tunnel test A while the vehicle with struts was tested in figure B. The above experiment is shown in figure C while the struts were disconnected but present in previous experiments [22]

Another equally important investigation was conducted at the aeroacoustic wind tunnel at Audi by Collin et al. [23] in 2016, in which the influence of the walls of wind tunnels were examined. All 25% scaled DrivAer models were used and the importance of a widespread test section, thus a low blockage ratio, was highlighted. Their results were compared with the ones created by TUM wind tunnel and it was found that a difference of drag and lift of $\Delta C_D < 0.008$ and $\Delta C_L < 0.024$ respectively, was present consistently.

Finally, experiments were conducted by Wittmeier and Kuthada [28] and Kuthada et al. [29] in order to investigate cooling/underhood flows as the models were upgraded with cooling air inlets. The drag was increased for all configurations with the difference of the drag coefficient for the Fastback geometry being $\Delta C_D = 0.01$. Also, the cooling air volume flow was dropped massively when both wheel houses were closed while lateral losses and increased velocities in the center of the vehicle were noticed due to the air cooling flow.

The above experiments offer a big data base in which many flow structures are described and many aerodynamic values are provided. Nevertheless, more experimental studies have been conducted even though they examined loads and flow features that have

already been available in the above data base. Their purpose was served to examine CFD codes by comparing numerical and experimental results and one of this is the work of John et al. [40] which published in 2018. Since this project uses the Fastback configuration of the DrivAer models, table 2.2 summarizes some features of the conducted experiments and provides values of drag and lift coefficients as well. It is worth noting that results with great accuracy have been obtained in wind tunnels with very small blockage ratio [13].

Study	Percentage of scaled model	Reynolds number (x10^6)	Velocity (m/s)	Blockage ratio (%)	C_D	C_L
Heft et al.	25	1.22 - 4.87	10 - 40	8	0.33 - 0.275	
Theissen et al.	50	10	up to 65	-	-	-
Mack et al.	40	5.2	45	8.3	0.274	-
Strangfeld et al.	40	0.75 - 2.8	up to 42	5.4	provided in a range of Re_L	
Wieser et al.	25	up to 3.2	up to 41	5.4	provided in a range of yaw angles	
Miao et al.	25	5.2	65	8	0.244	-0.031
Collin et al.	25	5.2	65	3.15	0.251	-0.039
Kuthada et al.	25	3.6	50	-	0.28	-

Table 2.2: Overview of experimental studies - Wind tunnel features and aerodynamic coefficients are provided only for the Fastback model. The last two studies involve the Fastback geometry with smooth underbody while the others with the detailed one.

2.3 Effects of wheel rotation to the overall vehicle aerodynamic performance

Wheels are one of the most influential components affecting vehicle aerodynamics and it is estimated that up to 25% of the total drag is caused by the wheels [13]. The first numerical and experimental investigation regarding the influence of rotating wheels was undertaken by Wäschle [24] who tested the effects of wheel rotation using three different rim geometries in a simplified quarter scale model and a Mercedes-Benz E-Class production car. A comparison between LDV measurements and CFD results was undertaken indicating that a good agreement could be achieved. The rotation of the wheels was mod-

elled using the MRF method and the results showed that due to the rotation, drag and lift were reduced locally at the front wheels while less flow separation was occurred at the contact patches. Moreover, the outer wheel squash vortex at the front wheels was larger when stationary wheels were used, leading to bigger wakes and affecting strongly the rest of the car. When rotation was applied, some of the vortices became weaker and some disappeared causing a significant drag reduction. Finally, it was highlighted that the wheels affected strongly the diffuser as it could not work efficiently with the stationary wheels underlining the importance of wheel rotation.

The evaluation of aerodynamic forces on a BMW car with different rear configurations was undertaken by Kandasamy et al. [25] conducting both experimental and numerical investigations. Particular attention was paid to the modelling of the rotating wheels as RWBC and MRF were utilized as well as the SM method that was used for the rotation of the non-axisymmetric parts of the wheel rims. In all methods, the tyre treads were represented by a RWBC and the results showed that the SM method is the most accurate. In detail, a maximum drag error of 5% was noticed for RWBC and MRF techniques while the error was reduced to 2% with the use of the SM method. However, the last two techniques produced almost similar front and rear lift values with the RWBC being the method with the largest error introduced. All in all, the SM method was proved to be the most robust and efficient.

A computational study was conducted by Koitrand et al. [26] in which different wheel modelling techniques were tested using two different tyre geometries in a Jaguar XF. For the rotation of the rim, the MRF and SM methods were used alongside with the RWBC for the rotation of the tyres. The first two techniques produced similar results regarding the drag coefficient despite the fact that small vortices were noticed with the use of the SM method while in the MRF method, they merged to form one large vortex. Generally, the SM method is proposed for future studies as it was the most accurate since the lift error was larger in the MRF method.

The most recent study that investigates different wheel rotating modelling methods

and includes the DriVaer model was published in 2018 by Yu [27]. RWBC, MRF and SM methods were utilized with Reynolds number up to $5.89 \cdot 10^6$. The MRF and SM methods were applied to the spokes resulting in higher velocity in that area than the RWBC technique and higher ventilation drag. Ventilation drag and lift coefficient were strongly affected by each method even though drag coefficients were comparable. Furthermore, the pressure distribution of the spokes were analysed indicating that the MRF method produced results with higher pressure than the ones using RWBC. Results produced by the SM method, were between the two techniques. Finally, the SM method was suggested for future use but its computational cost was highlighted as a simulation took 10 times longer than the other methods.

2.4 Numerical Investigations

This section includes various numerical studies related to the Fastback DrivAer model and special attention is paid to the wheel rotation modelling. Firstly, the influence of underhood flows are discussed and then, studies are categorized by the use of wheel modelling methods in their approach. There are four methods that can be used to model the rotation of the wheels and the ones that are utilized in the present work are described in section 4.1. Finally, studies that have implemented a crosswind scenario are reviewed since industry have been focusing on the influence of realistic conditions during the last years.

2.4.1 The influence of underhood flows

Another geometry feature that has been studied partially is the engine bay and its influence to the aerodynamics. In this section, previous works that have investigated underhood/cooling flows are discussed.

Having conducted an experiment, the work of Wittmeier and Kuthada [28] included a numerical investigation that the underhood flow was evaluated using the Notchback and

the Estateback geometries. The LBM (Lattice-Boltzmann Method) was used and a grid of 150 million cells was generated. The MRF method was utilized for the rotation of the wheels while a porous media was imposed to simulate the cooling package. Transient simulations were undertaken and attention was paid to the influence of the cooling flow to the aerodynamic forces. The numerical results showed that 3/4 of the cooling flow was exiting through the wheel houses while the drag was increased for both models but it was over-predicted.

Similar work was conducted by Kuthada et al. [29] in which all configurations were tested. A grid containing 300 million cells was used while the flow was solved using the LBM. Also, the SM method was imposed to model the rotating wheels while the radiator was modelled using porous media. Results showed that the cooling air exiting the wheel houses affected strongly the wake of the cars while high velocity regions were detected underneath the cars and flow loses in lateral areas were observed due to the cooling airflow.

The work of Simmonds et al. [30] which was published in 2017, investigated the cooling flow in three different cars including the Notchback DriVaer model. Initially, Notchback RANS simulations were conducted testing three turbulence models while the work was expanded using transient simulations only for the Notchback geometry utilizing IDDES and LBM. Three meshes were generated with the finest cell size being 1.25 mm and commercial CFD solvers, STARCCM+ and PowerFLOW, were used. The flow velocity was set to 100 km/h while the rotating wheels were modelled using MRF and SM methods. Firstly, it was deducted that the SA (Spalart-Allmaras) model was the most robust one predicting the cooling delta drag values with great accuracy. Moving to the unsteady results, only the IDDES with the SM method and the LBM could produce trustworthy results. Due to the smaller wheel houses, the exiting cooling flow through the wheel houses was computed to be 45% while the rest ended up underneath the car. Finally, the fact that further work should be done to compare the accuracy of IDDES and LBM was highlighted.

Paper of Matsumoto et al. [31] presented the influence of different engine bay configurations to the steady and unsteady aerodynamics using the Notchback configuration. The turbulence was modelled using DDES-SA while Dynamic Mode Decomposition (DMD) was performed on the walls of the car to study the unsteadiness. A grid of 66 million elements was generated with $y^+ = 31.9$ while simulations were conducted using OpenFOAM. Also, the flow velocity was set to 40 m/s which corresponds to $Re_L = 7.1 \cdot 10^6$. The drag was increased with the engine bay flow but it was noticed that it was greater with leakage around the radiator than without leakage. An increase to the lift of the frontal axis was detected due to the cooling flow, as well as to the pressure distribution of the underbody. DMD was performed and analysed but it is not a suitable reference for the present work since it focuses on other features.

2.4.2 Investigations with no rotating wheels

Numerical investigations using the Fastback configuration with no moving ground and rotating wheels have been conducted focusing on alternative aspects other than flow structures and body forces; namely studies of Guilmineau [32], Ashton and Alistair [33] and Ashton et al. [34]. All of them examined the accuracy of different turbulence models including RANS, EARSM and DES approaches. The results showed that the lift was predicted well only by the DES approach and that was the reason of the wake differences noticed between RANS and DES approaches. Also, the $k - \omega$ SST model was found to be the most accurate one achieving the least error on the prediction of both lift and drag. Overall, the SST-IDDES approach proved to be the most efficient and robust as it predicted correctly all forces and flow structures at the wake.

2.4.3 Investigations using Rotating Wall Boundary Condition

It has been proved that investigations with vehicles using RWBC for rotating wheels are adequate to produce results comparable to experimental tests [35], [36]. Moreover, due to the fact that the RWBC method is not computationally demanding and has low computa-

tional cost, it has been used for studies with computational limitations.

A year after the introduction of the DriVaer model, a numerical investigation was undertaken by Heft et al. [14] using the full scale Fastback geometry. Notchback RANS simulations were conducted at $Re_L = 4.87 \cdot 10^6$ using the $k-\omega$ SST model while slip boundary condition was imposed to the ground. Three mesh were generated with the finest being 19.4 million elements while the y^+ values were $30 < y^+ < 70$. Even though the forces were calculated with high accuracy, the surface pressure distribution varied significantly. The need for time-dependent simulations was highlighted in order to get a better agreement between numerics and experiments. Flow structures were examined as well but the accuracy of their characteristics is questionable since Notchback simulations were undertaken.

Paper of Jakirlic et al. [37] presented the differences between numerical approaches using all configurations of the DriVaer model. Notchback and unsteady simulations were conducted using RANS and a hybrid RANS-LES approach named PANS, respectively. Initially the grid was initialized with Notchback RANS, then URANS was enabled followed by PANS at the end. The generated mesh contained 24 million cells while wall functions were used since $y^+ \approx 30$. Special attention was paid to the complex structures of the wake of the cars and the accuracy of the unsteady method was highlighted. Drag coefficients were comparable with the ones obtained by experiments but variations were detected on the lift coefficients. Overall, the PANS method is adequate to produce results with high accuracy.

The differences between smooth and detailed underbody of the Notchback configuration as well as the differences between stationary and rotating wheels were investigated by Jakirlic et al. [38] in 2016. The VLES (Very Large Eddy Simulation) formulation was used along with the CFD software AVL-FIRE. Polyhedral cells were generated in the surface of the car and the grid contained 24 million cells with $0.5 < y^+ < 30$. The results showed that both lift and drag coefficients were increased with the use of the detailed underbody but the rotation of the wheels contributed to the reduction of these forces. A

detailed analysis highlighting the different recirculation regions in the wake of the car was conducted while the VLES method produced results with high accuracy.

Another numerical investigation comparing LES and wall-modelled LES (WMLES) schemes was conducted by Aljure et al. [39]. The Fastback geometry with simplified wheels was used and four meshes were generated with the finest one containing 79 million cells. A fractional-step algorithm was utilized for the pressure-velocity coupling and a linear explicit scheme was implemented for both convective and diffusive operators while the pressure gradient was solved implicitly. The results showed that the LES method is computationally expensive while the computational requirements were reduced with the use of WMLES as a drop of 70% in CPU time was observed. Drag and lift coefficients were obtained with differences from experimental results though. Having used simplified wheels with RWBC, some errors were introduced and that was the reason of the large discrepancy noticed in the coefficients. Both LES and WMLES produced similar results with the differences being noticed in the pressure coefficient profiles in areas with flow separation. Overall, the ability of both schemes to resolve flow structures was underlined but the WMLES was suggested for future use.

2.4.4 Investigations using Multiple Reference Frames

A computational study was undertaken by John et al. [40] along with the experiment in order to investigate the accuracy of the numerical scheme and the flow around the Dri-Vaer models. The flow was solved using LBM and one mesh of 227 million cells was generated. Modifications to the geometry (morphing) allowed to examine the influence of many parts leading to a study of 14 variants. The flow parameters were the same as previous experiments and the overall results showed a great correlation between numerics and experiments. Drag and lift coefficients were calculated for all cases but most importantly, the influence of the underbody was examined indicating an increase of 22 counts on drag by applying the detailed one. Also, the lift was increased by 31 counts due to the underhood flow, complying with previous studies. The study was focused on trying

to achieve the most accurate numerical scheme and showed the differences on the flow between numerics and experiments but it is not an acceptable reference for this work even though force coefficients are provided.

2.4.5 Investigations using Sliding Mesh and Overset Mesh

The MRF wheel modelling technique has been used widely due to its high accuracy and low computational time. However, the SM method is becoming more famous and it has been proven to be more robust and efficient with the cost of higher computational time required. Initially, this method was used for comparison between different modelling techniques but only few investigations have used this method recently in order to introduce the least error from the modelling of the rotating wheels; namely studies of Kandasamy et al. [25], Koitrand et al. [26], Yu et al. [27], Simmonds et al. [30] and Kuthada et al. [29] which were discussed in above sections.

Even though the SM is considered to be a state-of-the-art method, the overset mesh technique has been developed to model the rotation of the wheels and it is used by few researchers. Structured finite difference overset grid was examined by Peters et al. [41] in 2015 using the Fastback DriVaer model and the NASA's solver, Overflow. The grid consisted of 81 million points and special attention was paid to the rotation of the tyres in which unique boundary conditions were imposed. The results were promising having computed forces with great accuracy using 5^{th} order spatial accuracy. Also, a comparison was undertaken with previous numerical works indicating the fact that this method could produce more trustworthy results in less time than the volume mesh RANS approaches. Another work that used the overset method is the numerical study of Forbes et al. [42] which is discussed in section 2.4.6. It is worth mentioning that this method is the most computational demanding since overlapping meshes are used to solve the flow.

2.4.6 Realistic-Crosswind conditions

There are differences between wind tunnel and real-world conditions, such as the large energy-containing eddies in the flow which are present in the latter conditions along with non-uniform flow. During the last years, the need to explore the aerodynamic behaviour of vehicles under real-world conditions has arose. The effect of non-uniform flow was studied by Gaylard et al. [43] in 2014 using high turbulent properties (turbulence intensities of 4% and 7% and turbulence length scale of 2 meters) as fluctuations to the free-stream flow. Due to high turbulence intensities, velocity fluctuations were added to the wakes reducing their pressure while mixing led the high velocity jets to become weaker. Flow structures were affected by mixing and diffusion and the overall drag was increased. Also, the velocity of the flow under the car was decreased resulting in higher lift force. Moreover, wheel deflectors were examined in order to provide design propositions while the real-world conditions were considered to be necessary to the optimization process of a vehicle in order to get a good correlation between "expected" and "real world" performance.

The Fastback geometry of the DriVaer model was modelled under crosswind conditions and a six degrees-of-freedom vehicle handling simulation was undertaken as well by Forbes et al. [42]. The simulated crosswind followed the parameters of ISO 12021:2010 prescribing a 20 m/s crosswind velocity and 27.8 m/s vehicle speed that resulted in a 36^0 yaw which can be considered as a severe gust. The boundary conditions at the domain were updated as two inlets and two outlets were imposed and the overset method was utilized for the rotation of the wheels in order to measure accurately the experienced moments of the car. Also, in order to prevent dissipation of the wind profile, the mesh was refined in upstream direction. Even though, mesh strategies and the implementation of a crosswind were discussed, this study was focused on flow structures induced by unsteady conditions so it is not a suitable reference for the present work.

Paper of Howel et al. [44] presented results for a sheared crosswind flow using the Fastback and Estateback configurations of the DrivAer model. Even though the vehicle speed was equal with the above study of Forbes, the wind velocity was set to be 4.9

m/s generating a 10^0 yaw and a 28.23 m/s resultant velocity. The wind velocity profile was described by a power law relation and a mesh of 69 million elements was generated with asymmetrical refinement box suited for the crosswind profile, as seen in figure 2.14. Unsteady IDDES simulations were conducted while the cases were initialized using a Notchback RANS solver. Results showed that variations of the drag and lift coefficients were noticed locally leading to the conclusion that the difference between sheared and unsheared conditions is not negligible. However, pressure and velocity distributions were almost identical while the velocity distribution became uniform over the height of the car as the sheared flow approached it.

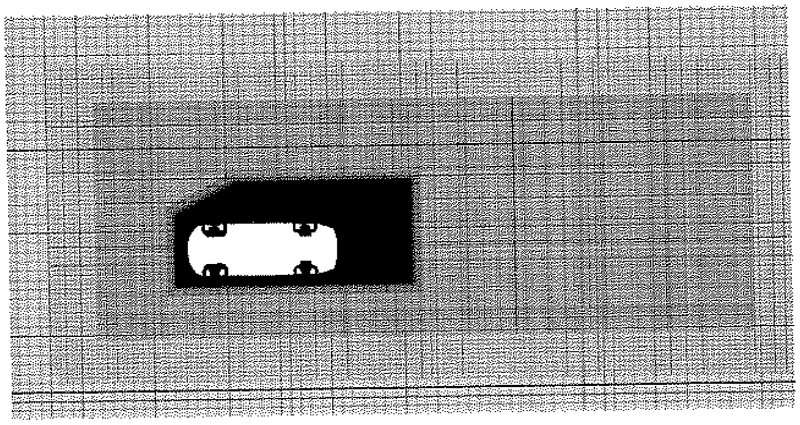

Figure 2.14: Slice of the volume grid used in Howel's study [44] - The refinement is noticed on the one side of the car due to the crosswind profile

The most recent study is the one from Duncan et al. [45] that investigated the effect of light and strong winds using squareback, Notchback and SUV vehicles with engine bay included. Three values for turbulence intensity were used and unsteady simulations were undertaken using the LBM. The results proved that the turbulence intensity was affected by the presence of the vehicle (it was higher near the car) and the drag coefficient was increased for all cases. Also, sedan-like cars seemed to be less sensitive in real-world conditions as the rear-lift was increased slightly without causing a huge instability. Mixing and dissipation were taken place while wakes were broken up and shortened with the increase of the turbulence intensity.

As can be seen, researchers have drawn their attention to realistic scenarios in recent years in order to get a better correlation between "expected" and real-world results. Table

2.3 shows the numerical investigations which involved the DriVaer models and provides some detailed values of the numerics of each study.

Overall, it can be seen that the the MRF and SM methods yield better results with the last one being the least used but most importantly the one that represents the real-world. However, it is computationally expensive and that's why the MRF method is still used. As far as the real-world conditions concern, the present work is taking account on actual conditions provided by the Department from Transport of the United Kingdom for British highways. Therefore, the obtained results will give a clear picture of body forces and fuel consumption in real-world conditions.

Study	Configurations of DriVaer	Finest grid (millions)	Turbulence scheme	Turbulence model
Wind-Tunnel Conditions				
Heft et al.	F	19.4	RANS	$k-\omega$ SST
Wittmeier and Kuthada	N,E	150	Particle-based	LBM
Kuthada et al.	All	300	Particle-based	LBM
Simmonds et al.	N	1.25 mm cell size on the car	IDDES & Particle-based	Spalart-Allmaras $k-\omega$ SST Realizable $k-\varepsilon$
Matsumoto et al.	N	66	DDES	Spalart-Allmaras
Guilmineau	All	38.7	RANS & DES	EARSM
Ashton and Alistair	All	300	RANS & DES	Spalart-Allmaras Realizable $k-\varepsilon$ $k-\omega$ SST
Ashton et al.	E,F	100	RANS & DES & IDDES	Spalart-Allmaras Realizable $k-\varepsilon$ $k-\omega$ SST Elliptic Blending $k-\varepsilon$ v^2-f Elliptic Blending Reynolds Stress
Jakirlic et al. [37]	All	24	RANS & RANS-LES	Elliptic-Relaxation Method $\zeta-f$
Jakirlic et al. [38]	N	24	VLES	near-wall eddy-viscosity 4-equation
Aljure et al.	F	79	LES-WMLES	-
John et al.	All	227	Particle-based	LBM
Peters et al.	F	81	RANS	-
Crosswind/Realistic Conditions				
Forbes et al.	F	20.3	DDES	Spalart-Allmaras
Howell et al.	F,E	69	IDDES	Spalart-Allmaras

Table 2.3: Overview of numerical studies related to the DriVaer models

Chapter 3

Flow physics

3.1 Governing Equations

CFD is essentially based on the governing equations which describe all fluid motions. Even though the flow can exhibit complex motions, the governing equations were derived by elementary laws of physics - mass conservation, Newton's second law and first law of thermodynamics. Basically, they represent the mathematical statement upon which all of fluid dynamics is based. From a numerical viewpoint, they can be obtained in many different forms (conservation, convective etc.) and the use of a specific form may cause oscillations to the numerical solution while another form could be more appropriate [46]. The governing equations can be written as follows with the use of invariant notations:

- Continuity equation:

$$\frac{\partial \rho}{\partial t} + \nabla(\rho \mathbf{u}) = 0 \ . \tag{3.1}$$

- Momentum equation:

$$\underbrace{\frac{\partial(\rho \mathbf{u})}{\partial t}}_{1} + \underbrace{\nabla(\rho \mathbf{u} \otimes \mathbf{u})}_{2} = \underbrace{\mathbf{F}}_{3} \underbrace{- \nabla p}_{4} + \underbrace{\mu \nabla^2 \mathbf{u}}_{5} + \underbrace{\frac{1}{3}\mu \nabla(\nabla \cdot \mathbf{u})}_{6}$$

where the terms can be expressed as follows:

1. unsteady term
2. convective term
3. body forces
4. pressure gradient
5. viscous dissipation
6. compressibility effect

- Energy equation:

$$\rho\frac{\partial E}{\partial t}+\rho(\mathbf{u}\nabla)E=-\nabla\cdot(\mathbf{u}p)+\nabla\cdot(\lambda\nabla T)+\mathbf{u}\cdot(\nabla\bar{\bar{\tau}})+\bar{\bar{\tau}}\cdot\cdot(\nabla\otimes\mathbf{u})+\varphi_s\ , \quad (3.2)$$

where the two terms in the left-hand side represent the thermodynamic and mechanical power, since E equals to internal plus kinetic energy. On the right-hand side of the equation, the terms are expressed as heat energy induced by surface forces, heat transfer due to conduction, heat transfer due to viscous forces (two terms included) and external heat sources or reactions.

For the present study, an incompressible solver is used and thus the above equations are simplified since the density is constant. The reason lies on the fact that the Mach number is very low and there are no shock waves propagating to the domain, so a compressible solver would be inappropriate to solve the flow [47]. Also, the work focuses on the study of flow phenomena generated by incompressible features so the energy equation is not used while the continuity and momentum equations can be written as follows respectively:

$$\nabla\cdot\mathbf{u}=0\ , \quad (3.3)$$

$$\rho\frac{\partial(\mathbf{u})}{\partial t}+\nabla(\rho\mathbf{u}\otimes\mathbf{u})=-\nabla p+\mu\nabla^2\mathbf{u}\ . \quad (3.4)$$

It is worth noting that the gravitational force is considered to be negligible and it is not taken into account, so this term is removed from equation 3.4.

3.2 Turbulence modelling

RANS model

Osborne Reynolds derived the so called RANS (Reynolds Averaged Navier-Stokes) equations in 1895 which are used widely by CFD applications. Due to the fact that it was not feasible to calculate every fluctuation in the fluid, averaging was necessary and led to the derivation of the aforementioned equations which are based on statistical turbulence models. The averaging procedure was undertaken by decomposing variables into the fluctuating and mean components. So, the instantaneous velocity component was decomposed to the averaged velocity component and the fluctuating velocity component which can expressed as:

$$\mathbf{u} = \bar{\mathbf{u}} + u' \ . \tag{3.5}$$

Inevitably, rules related to the simplification of the equations were created (e.g. the fluctuating component becomes zero if the instantaneous component is averaged over a sufficient amount of time) and were applied to the continuity and momentum equations leading to the following equations:

$$\nabla \cdot \bar{\mathbf{u}} = 0 \ , \tag{3.6}$$

$$\rho \frac{\partial \bar{\mathbf{u}}}{\partial t} + \rho \nabla (\bar{\mathbf{u}} \otimes \bar{\mathbf{u}}) = \rho g - \nabla p + \mu \nabla \bar{\mathbf{u}}^2 - \underbrace{\nabla (\overline{\rho u' \otimes u'})}_{F_R} \ .$$

The second one is the RANS equation and the last term is the Reynolds stress tensor F_R which is an additional term in order to provide closure to the problem of multiple

unknown variables. The term can be written as:

$$F_R = -\rho \begin{bmatrix} \overline{u'u'} & \overline{u'v'} & \overline{u'w'} \\ \overline{v'u'} & \overline{v'v'} & \overline{v'w'} \\ \overline{w'u'} & \overline{w'v'} & \overline{w'w'} \end{bmatrix} . \tag{3.7}$$

Three normal stresses are noticed in the main diagonal while ten variables are unknown in total in which six shear stresses are included. Assuming isotropic turbulence, more simplifications can be applied and the following can be deducted:

$$\overline{u'u'} = \overline{v'v'} = \overline{w'w'} , \tag{3.8}$$

$$\overline{u'v'} = \overline{v'w'} = \overline{u'w'} \neq 0 . \tag{3.9}$$

Closure can be achieved by the Boussinesq approximation which is used by the most common turbulence models. The difference between all turbulence models lies in the fact that the eddy viscosity is calculated differently on each model. This approximation puts together the Reynolds stress tensor, the mean strain rate tensor, S_{ij}, and the eddy viscosity, μ_t, in the following way:

$$F_R = 2\mu_t S_{ij} . \tag{3.10}$$

SST $k-\omega$ turbulence model

Even though many turbulence models were tested, as mentioned in the Literature, the $k-\omega$ SST model proved to be the most efficient by predicting accurately forces and flow structures. Therefore, this model was chosen for the present work. It was derived by Menter in 1994 and it is a two-equation eddy-viscosity model. Also, it provides closure to the RANS equations in an elegant way as it allows to model the viscous sub-layer of the boundary layer and it behaves neatly in the free-stream due to the $k-\omega$ and SST formulations respectively. Initially, the model was too sensitive to the inlet turbulence

properties but this problem was solved adding the SST equation which provides an efficient $k-\varepsilon$ behavior. Many researchers have examined this model and acknowledged its great behavior in separating flow and adverse pressure gradient.

The transport equations, the turbulent kinetic energy and the dissipation rate, are written as follows, respectively:

$$\frac{\partial k}{\partial t}+U_j\frac{\partial k}{\partial x_j}=P_k-\beta^* k\omega+\frac{\partial}{\partial x_j}\left[(\nu+\sigma_k\nu_T)\frac{\partial k}{\partial x_j}\right] \quad , \tag{3.11}$$

$$\frac{\partial \omega}{\partial t}+U_j\frac{\partial \omega}{\partial x_j}=aS^2-\beta\omega^2+\frac{\partial}{\partial x_j}\left[(\nu+\sigma_\omega\nu_T)\frac{\partial \omega}{\partial x_j}\right]+2(1-F_1)\sigma_{\omega^2}\frac{1}{\omega}\frac{\partial k}{\partial x_i}\frac{\partial \omega}{\partial x_i} \quad . \tag{3.12}$$

Many closure coefficients are used and the explanation of them is extensive but it is beyond the framework of this section, so readers can find their values and more information in Menter's paper [48]. The kinetic eddy viscosity was derived by using a blending function, F_2, in order to limit the SST formulation to wall bounded flows and is expressed as:

$$\nu_T=\frac{a_1 k}{max(a_1\omega, SF_2)} \quad . \tag{3.13}$$

Detached Eddy Simulation

The DES method was proposed by Spalart et al. [49] in 1997 and it is a hybrid method that combines RANS and LES approaches. The near-wall regions are treated with a RANS approach while the flow in the rest of the domain is solved using LES approach. The need for a computational efficient model led to the formulation of DES as LES requires a huge computational budget. Initially, it was derived using the SA model for the RANS region along with a Smagorinsky-like LES approach. Also, it can be used with other turbulence models with the restriction that the turbulence length scale must be defined appropriately. Numerous researchers have used Menter's SST model proving the fact that it works well with the DES method.

Since the SA model is used for the near-wall region, the eddy viscosity is adjusted to scale with the local deformation rate, S, and the distance to the closest wall, d.

$$\nu \propto Sd^2 \tag{3.14}$$

However, in the Smagorinsky Sub-Grid Scale (SGS) model the eddy viscosity is proportional to the grid spacing, Δ.

$$\nu_{SGS} \propto S\Delta^2 \tag{3.15}$$

Therefore, d in the SA model was replaced by a length formulation that uses Δ in the following way:

$$\tilde{d} \equiv min(d, C_{DES}\Delta) \ , \tag{3.16}$$

where C_{DES} is a constant. This formulation allows the flow to be modelled with the SA model when $d \ll \Delta$ and a SGS model when $\Delta \ll d$. The constant was calibrated later by Shur [50] by conducting many numerical investigations and the value of 0.65 was finalized.

Even though, DES had a robust behavior in thin boundary layers - it was derived for simulations using airfoils - the model proved to be quite inaccurate in shallow separation regions as well as in regions with thick boundary layer. The problem has been solved by Spalart et al. [51] in 2007 by updating the previous model and ending up to a new formulation called Delayed-Detached Eddy Simulation (DDES). A delayed parameter r_d which is the ratio of the model length scale to the wall distance, was modified to apply to any eddy-viscosity model and can be expressed as:

$$r_d \equiv \frac{\nu_T + \nu}{\sqrt{U_{i,j}U_{i,j}}\kappa^2 d^2} \ , \tag{3.17}$$

where $U_{i,j}$ is the velocity gradients, κ is the Karman constant and d is the distance to the wall. This parameter expresses logarithmically the boundary layer profile being 0 on the edge of the boundary layer and gradually increases to 1. Also, the following function is

used and takes values between 0 and 1.

$$f_d \equiv 1 - tanh([8r_d]^3) \tag{3.18}$$

In the LES region the function f_d equals to 1 while elsewhere equals to 0. According to the above, the length scale d is updated as follows:

$$\tilde{d} \equiv d - f_d max(0, d - C_{DES}\Delta) \ . \tag{3.19}$$

A year later Shur et al. [52] derived a model that combined DDES and WMLES called Improved Delayed-Detached Eddy Simulation (IDDES). The DDES branch is activated when inflow conditions do not have any turbulent content while the WMLES branch is active in a simulation when the inflow conditions exhibit unsteadiness. The blending could not be done directly and the following formulation was derived:

$$l_{IDDES} = \tilde{f}_d(1 + f_e)l_{DDES} + (1 - \tilde{f}_d)l_{LES} \ , \tag{3.20}$$

where the two ingredients of the length scale $\tilde{f}_d$ and f_e are written as:

$$\tilde{f}_d = max[(1 - f_d), f_\beta] \ , \tag{3.21}$$

$$f_e = max[(f_{e1} - 1), 0]\Psi f_{e2} \ . \tag{3.22}$$

When inflow turbulent conditions are applied, the formulation 3.20 reduces to $l_{IDDES} = l_{WMLES}$ because f_d equals to 1 and thus $\tilde{f}_d = f_\beta$. On the other hand, when DDES is activated, f_e equals to 0 leading to $l_{IDDES} = l_{DDES}$. One of the advantages of this model is the fact that the mismatch between the modelled log layer and the resolved log layer has been resolved. Also, this model is used widely in different applications as different regions are solved with RANS and LES efficiently indicating the robustness of the model.

Another difference is noticed in the prediction of body forces in which the IDDES model has proved to be superior [53] and that is why this model was selected for the present work. Furthermore, Simmonds et al. [30] and Ashton et al. [34] have recommended this approach for future use.

Chapter 4

Methodology

4.1 Wheel Modelling Techniques

One of the main investigations of this thesis is the influence of the rotating wheels to the overall car aerodynamics and thus the modelling methods for the wheels play a crucial role. Due to the fact that ANSYS Fluent was selected, four wheel modelling techniques can be used. The simplest ones are the Rotating Wall Boundary Condition (RWBC) along with the Multiple Reference Frames (MRF) while the Sliding Mesh (SM) method and the Overset Mesh method are considered to be more complicated. The first three methods were used in the present work as the last method is computational expensive and requires a huge computational budget.

4.1.1 Rotating Wall Boundary Condition

The most common method for modelling the rotation of the wheels is the RWBC in which an angular velocity is imposed to the surface of the wheels to specify the rotation. This technique can be used in both steady-state and transient simulations and for the present work, is applied to all rotating surfaces including the contact patch. As far as the set-up is concerned, the direction and origin of the axis of rotation must be specified along with the rotational speed.

4.1.2 Multiple Reference Frames

The MRF technique and the RWBC method exhibit similarities as both can be applied to steady-state and transient simulations and they do not affect the mesh. The MRF technique is applied to cell zones which are chosen by the user and it allows these zones to move at different rotational speeds. The moving reference frame equations are solved in user-defined zones in which a rotating system moves with constant angular speed with respect to the stationary system. Variables are calculated in such a way that points from the CFD domain are specified by position vectors from the origin of the rotating frame.

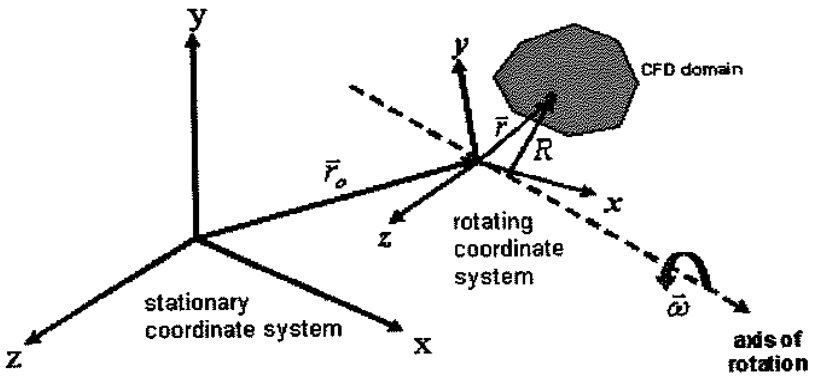

Figure 4.1: Stationary, Rotating Frames and CFD Domain - The origin of the rotating frame is located by the vector $\vec{r_0}$ while vector $\vec{r}$ is used to locate a point from the CFD domain [54]

Therefore, the updated fluid velocities are implemented to the governing equations and are expressed as:

$$\vec{u}_{\vec{r_0}} = \vec{u} - \vec{u}_{\vec{r}} \ , \tag{4.1}$$

where

$$\vec{u}_{\vec{r}} = \vec{\omega} \times \vec{r} \ . \tag{4.2}$$

The $\vec{u}$ velocity component is the absolute velocity, $\vec{u}_{\vec{r_0}}$ is the relative velocity viewed from the rotating frame and the other one is the velocity due to the moving frame.

Although, it is clearly understandable that this method is an approximation, it has been used widely producing results with good accuracy, as discussed in the Literature. However, the motion between moving zones is not taken into account, as the mesh is

fixed, which sometimes is the case in real-life conditions.

4.1.3 Sliding Mesh

The SM method is used preferably for simulating flows in multiple moving reference frames where unsteady interactions are present and important and a time-accurate solution is required. This method allows the motion of user-defined zones and thus the movement of the mesh. For this purpose, an interface must be defined so as the user will specify the moving zones which slide relative to one another along the interface.

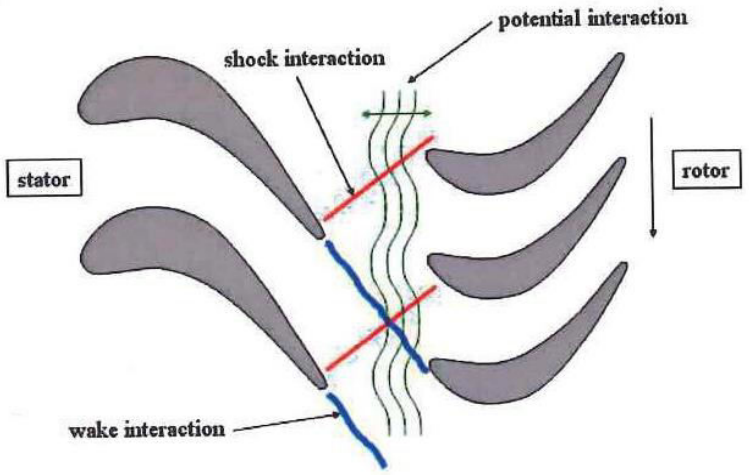

Figure 4.2: Unsteady interactions [54]

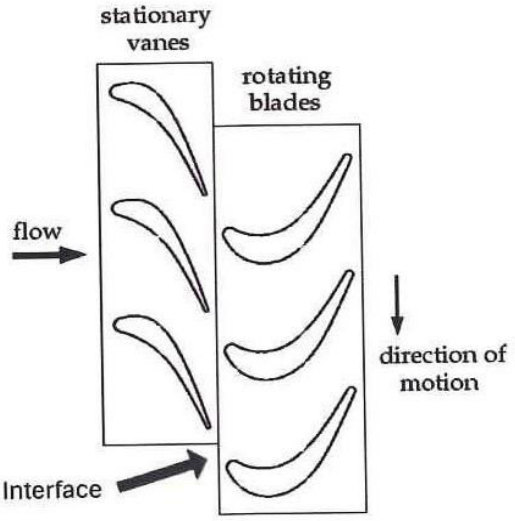

Figure 4.3: Sliding mesh represantation in two dimensions - The interface separates the rotating zone with the stationary one [54]

An advantage of this method is the fact that node alignment is not needed as the time passes and the mesh is moving. So, this method is used in time-dependent simulations and the movement of the mesh is accomplished in discrete steps.

The transferred fluxes across the interface are simplified as the motion of the moving zones is calculated with respect to the stationary frame and thus no moving reference frames are required. Also, the control volume remains constant between time levels, $V^{n+1} = V^n$, and the conservation equation for a scalar ϕ can be written as follows in an

integral form:

$$\frac{d}{dt}\int_V \rho\phi dV + \int_{dV} \rho\phi(\vec{u}-\vec{u}_g)\cdot d\vec{A} = \int_{\partial V} \Gamma\nabla\phi\cdot d\vec{A} + \int_V S_\phi dV \ , \tag{4.3}$$

where $\vec{u}$ is the flow velocity, $\vec{u}_g$ is the mesh velocity, Γ is the diffusion coefficient and S_ϕ is a source term.

In automotive aerodynamics, this method produces the most trustworthy results but it is computational expensive, as previous investigations have proven. Allowing the mesh of the rims of the wheels to move has secured a way of not losing any information and thus the prediction of body forces and flow structures is achieved with great accuracy. For the present work, the wheels are split into regions where different methods are imposed. The MRF and SM methods are applied to a specific area of the wheel while RWBC is imposed to the rest of it. In detail, the rims are described by the MRF and SM methods while RWBC is applied to the tyres and contact patches, as seen in figure 4.4.

Figure 4.4: Wheel with highlighted MRF/SM region enclosing the spokes

4.2 Contact patch

The modelling of the contact patch between the wheels and the ground is of the utmost importance and remains one of the biggest challenges that automotive aerodynamicists face. Generally, the wheels are not modelled with the same way as in real world, since they are placed above the ground in a specific height. The reason lies in the fact that really

small elements have to be generated in that region causing a bad quality mesh, so a height is introduced in order to overcome this problem. For the present work, a height of 15 mm was chosen since results from a step height sensitivity study showed that this height was the optimal one. Predicted lift and drag were comparable with the experimental ones with the lift taking the exact value as experiment [55]. It is worth noting that the height is considered to be an extension of the tyre, so a RWBC is imposed to it as well. Finally, there is only one modelling technique that allows the modelling of the wheel without any height - overset mesh (chimera) - but it is very demanding computationally and it is not examined in this project.

Figure 4.5: Wheel with highlighted step height

4.3 Geometry

The used geometry was discussed in section 2.1.1 along with its advantageous usage. Recently, the model was updated with an engine bay configuration in order to examine underhood/cooling flows. The present investigation involves only one model which includes the Fastback configuration with a detailed underbody, engine bay, engine, exhaust and a radiator, as seen in figure 4.6. Also, the full scale model is used with its total length, height and width being 4.613 m, 1.404,73 m and 2.025,44 m respectively, while the frontal area is 2.17 m^2.

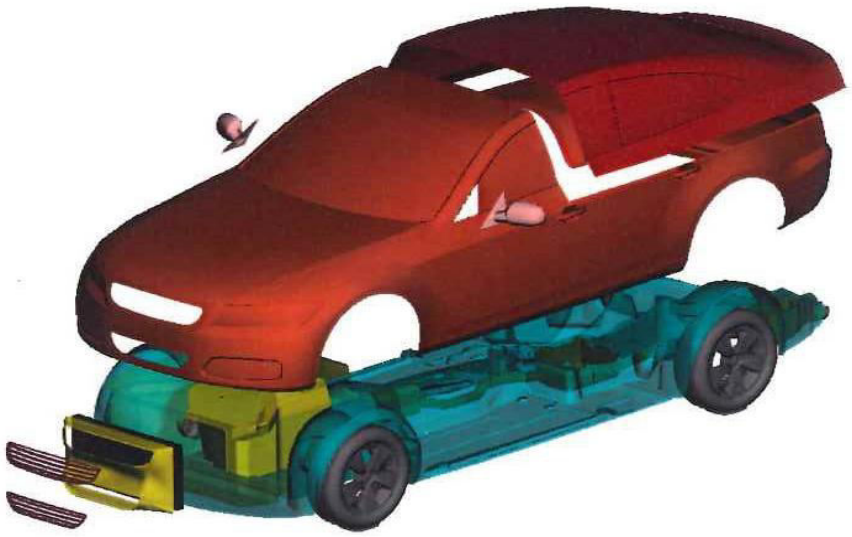

Figure 4.6: Examined model with all parts

Features	Colours
Fastback End	
Main Body	
Mirrors	
Grilles	
Engine Bay	
Radiator	
Engine-Exhaust	
Detailed Underbody	
Detailed Wheels	

Table 4.1: Parts of the DriVaer model viewed in the above figure

4.4 Grid Generation Strategy

In this section, the mesh strategy is described starting from the selection of the domain size. Three unstructured meshes were generated using the ANSA software by BETA CAE Systems. The vehicle's surfaces are represented by triangular elements while the boundary layer consists of prismatic cells and the rest of the volume is filled with tetrahedral

elements.

4.4.1 Computational Domain

The computational domain plays a critical role to the computational analyses especially in the case of external aerodynamics. Ideally, the domain should be as far as possible, so as the flow will not interfere with the test subject, but its size should be limited in order to achieve low computational cost. In automotive aerodynamics, the flow around the car is not restricted naturally and thus the chosen domains are sufficiently large to achieve free-stream conditions. Moreover, many wind tunnel facilities can not mimic these conditions causing a nozzle effect which accelerates the flow and producing corrupted results. For this reason, the blockage ratio ϕ was derived to assess the size of the domain:

$$\phi = \frac{A_{ref}}{W_N \cdot H_N} \ , \tag{4.4}$$

where A_{ref} is the frontal area of the test subject, W_N and H_N are the width and height of the domain respectively. So, the smaller the number of ϕ, the closer the conditions are to the free-stream ones. From the Literature, numerous numerical studies used blockage ratio of 1% except the one from Simmonds et al. in which 0.05% blockage ratio was set. However, a drop to the blockage ratio is noticed in the investigations concerned crosswind scenarios with the use of 0.03% blockage ratio being the smallest one [17]. Of course, the scale of the car affects this value so the domain was chosen accordingly for each study.

Taking into consideration all previous investigations, the domain size used by Forbes et al. [42] was selected since the objectives of that work coincide with the ones of the present project. The length of the domain is set to 21L (where L is the length of the car) and the vehicle is placed 6L behind the inlet. Also, the height is equal to 2L which corresponds to about 6.5 times the height of the car, and the width is 13L. This domain results in a sufficient blockage ratio of 0.39%.

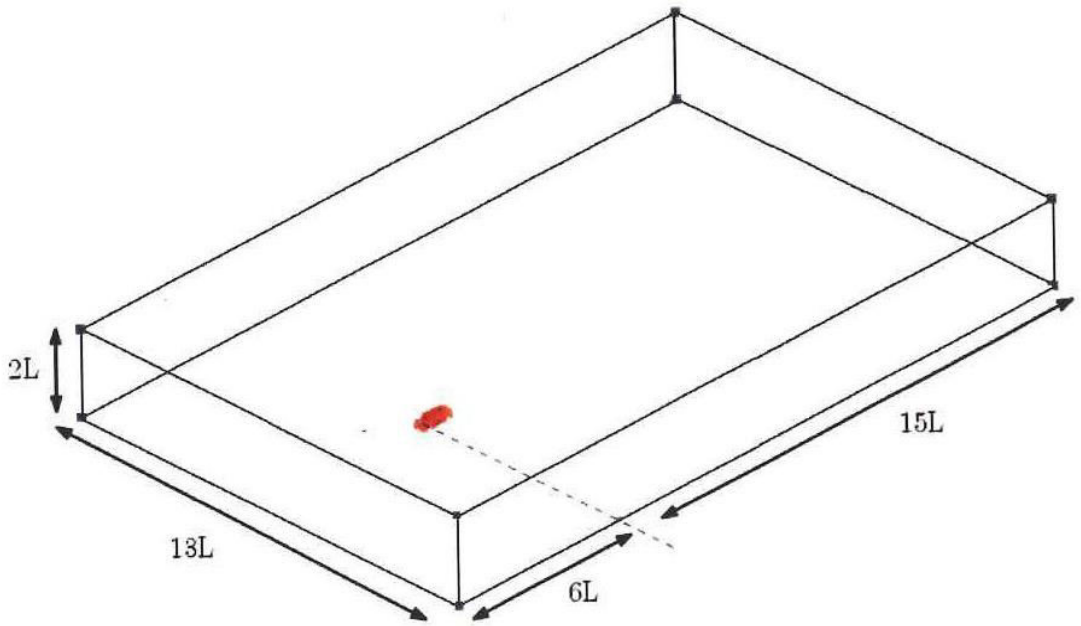

Figure 4.7: Dimensions of the chosen domain

4.4.2 Surface Mesh

After the selection of the domain size, the nest step is the surface mesh generation. The surfaces should be meshed in such a way so that the geometry would not change (e.g. curved regions should remain as they are with the same curvature). Also, good surface mesh quality is needed otherwise the boundary layer will be problematic and excessive numerical errors will be introduced. The number of generated surface elements varied on each numerical investigation discussed in the Literature with the highest one being 2.9 million [32].

Due to the complex geometry of some parts triangular elements were generated providing a good quality surface mesh. The minimum spacing was set to 2 mm in order to preserve the shape of curved and complex regions. Since three meshes were generated, the surface mesh was refined gradually by changing the maximum spacing. Table 4.2 provides the number of elements of the three generated surface meshes.

	Coarse	Medium	Fine
Main Body	833,628	1,059,258	1,142,539
Wheels	643,368	643,368	702,044

Table 4.2: Number of surface elements on the car and the wheels of each mesh

4.4.3 Volume Mesh

Once the surface mesh was generated and checked, then the generation of the boundary layer took place. According to previous studies, values of y^+ were ranging from $1 < y^+ < 200$. Turbulence models and computational budget were the most influential components for the chosen value of y^+. As mentioned above, the $k-\omega$ SST turbulence model is chosen and its use allows the flow to be resolved up to the wall. Therefore, the y^+ is set to be equal to 1 on the main body of the car following the studies that used this value alongside the $k-\omega$ SST model. Different number of layers was chosen for the meshes but the first 10 layers were generated with 1.2 growth factor while the rest of them with aspect ratio of 1. In this way the total height of the boundary layer is increased and the goal of 8 cm total height was achieved. The reason of this height lies in the capture of flow structures that occur close to the surfaces of the car.

As far as the wheels concern, different value of y^+ was used. A compromise had to be made due to the limited computational resources and it was decided to use $y^+ = 12$ on the wheels in order to generate fewer cells on these regions but at the cost of the mesh quality. In these regions the aspect ratio is bigger but the quality of the mesh is acceptable.

Special attention was paid around the car and the wake where three refinement boxes were used. Figure 4.8 shows the sizes of refinement boxes. The spacing on the edges of the boxes was set and gradually was refined, as table 4.3 shows. The quality of the meshes was assessed and 6 elements were found to have a maximum skewness of 0.978 in the boundary layer of the engine bay due to the complex geometry, while the maximum angle is 176^0. The resulting grids have good quality according to the brief examination

and numerical stability is expected to be achieved.

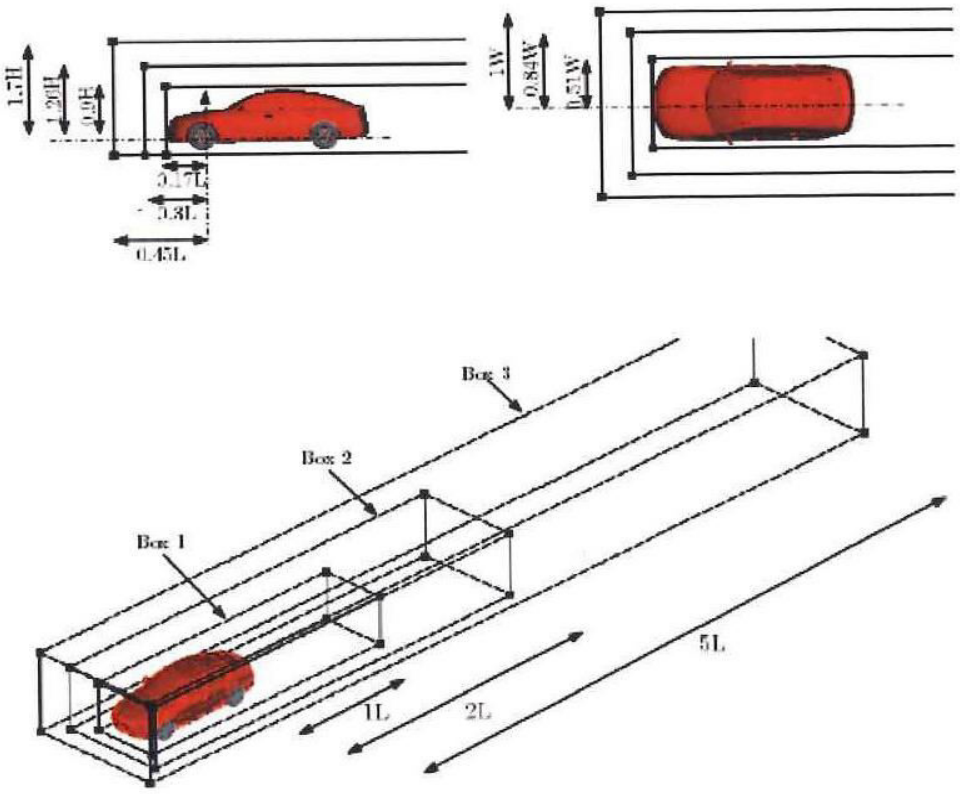

Figure 4.8: Dimensions of refinement boxes

Spacing	Coarse	Medium	Fine
Box 1	100	75	40
Box 2	220	190	130
Box 3	330	270	220

Table 4.3: Spacing in millimetres on the edge of the boxes

The following table provides the number of elements generated for the meshes.

	Coarse	Medium	Fine
Number of layers			
Main Body	17	20	23
Wheels	5	6	7
Number of cells on the boundary layer			
Main Body	14×10^6	20×10^6	26×10^6
Wheels	4.8×10^6	5.3×10^6	6.5×10^6
Number of cells on the volume			
Total elements	30×10^6	39×10^6	50×10^6

Table 4.4: Number of elements in different regions

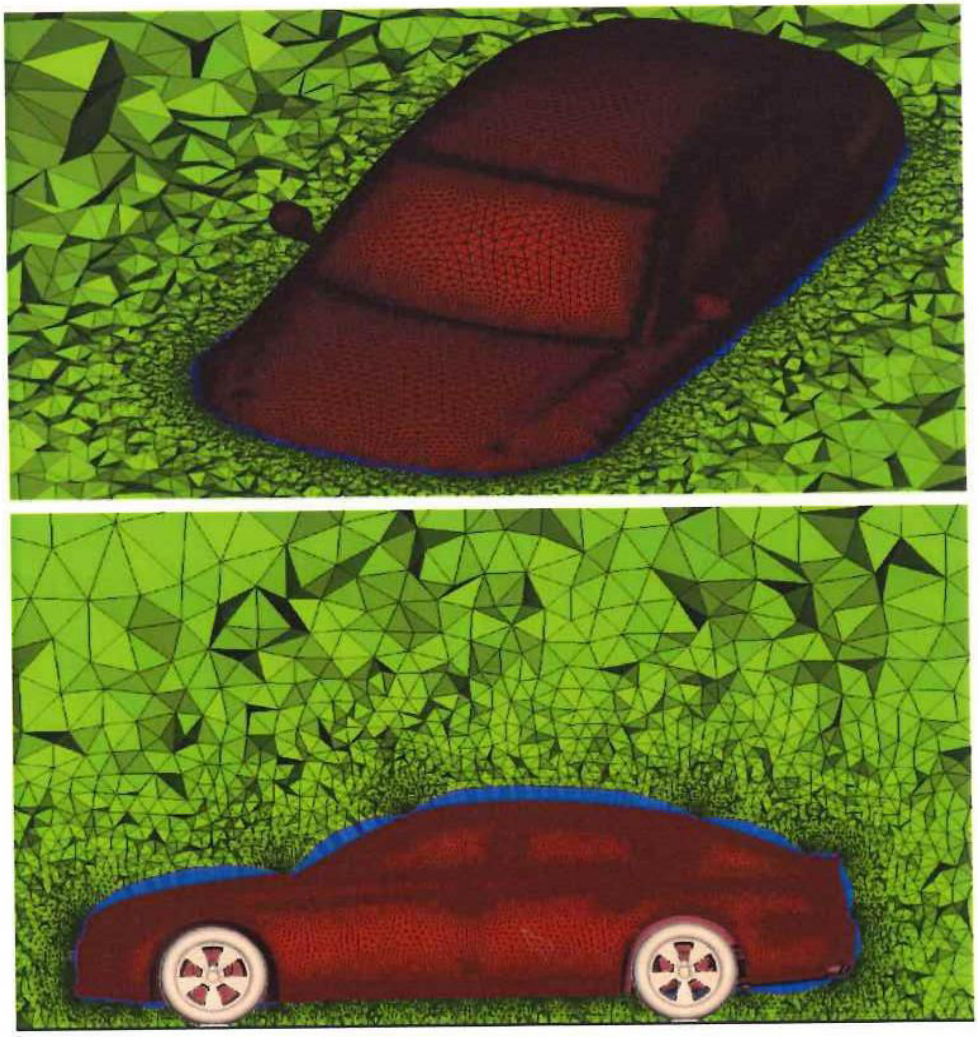

Figure 4.9: Overall mesh generated for the fine grid

Wheel meshing strategy

The MRF and SM techniques require different meshing strategy than the RWBC in order to apply the rotation. Two additional interfaces on each wheel were designed to serve the purposes of the methods since they were necessary to isolate the rotating volumes of the wheels. Figure 4.10 shows the rotating region in which the interfaces are located at its ends.

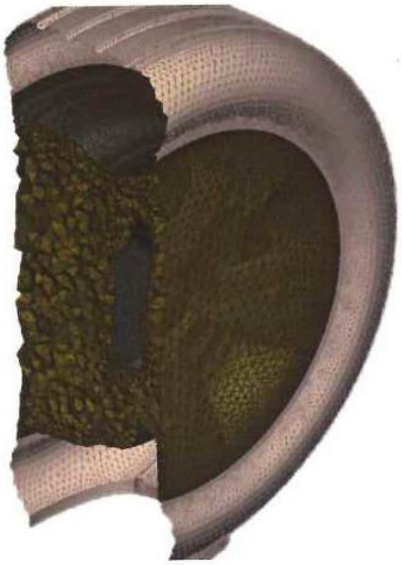

Figure 4.10: Volume mesh of the defined rotating region for MRF and SM methods

4.5 Boundary Conditions

Since the present study investigates two different conditions - wind tunnel and real-world crosswind - the boundary conditions are set accordingly. Previous investigations that implemented a crosswind scenario used two inlets and two outlets. In the same way, two velocity inlets and two pressure outlets were imposed while symmetry was applied to the ceiling. On the other hand, only one inlet and one outlet were needed for the wind tunnel study. The other walls of the domain were modelled as symmetry. For both cases, a no-slip wall moving longitudinally at car speed (26.55411 m/s) was prescribed on the ground. Moreover, no-slip wall was applied to the surfaces of the car except the parts of the wheels where rotating methods were imposed, as described previously. When RWBC was applied, the rotational speed was set to 83.2417 rad/s. Figure 4.11 shows the

differences between the two cases.

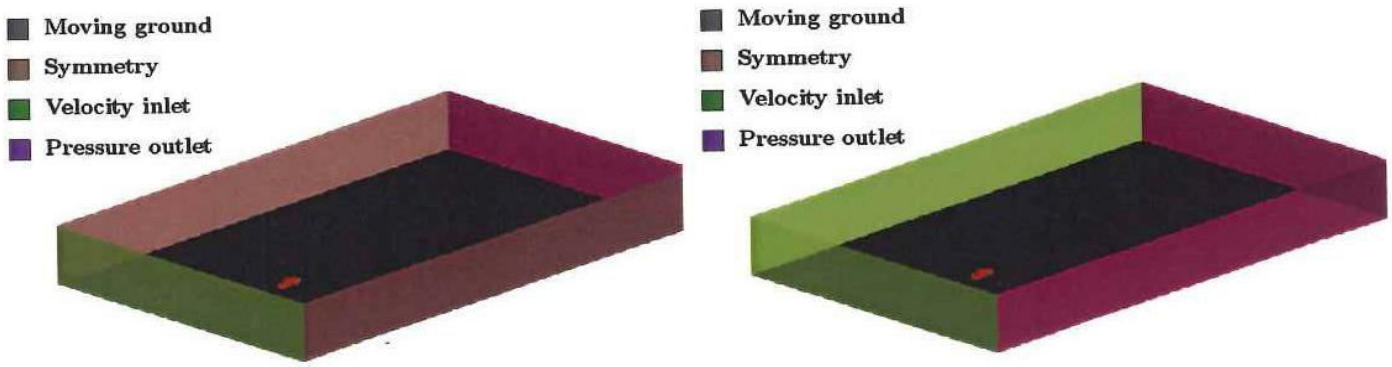

Figure 4.11: Boundary conditions for wind tunnel conditions (left) and real-world conditions (right)

4.5.1 Radiator Modelling

In all cases, the radiator was modelled as porous medium which is a common approach in the automotive sector. The usage of porous modelling produce great results if it is implemented correctly and leads to the reduction of computational cost since a detailed geometry with high resolution mesh is avoided [56]. In this approach, the fluid flow equations are modified and solved with an additional term, S_p. So, the momentum equation is written as:

$$\frac{\partial}{\partial t}(\gamma\rho\vec{u}) + \nabla\cdot(\gamma\rho\vec{u}\vec{u}) = -\gamma\nabla p + \nabla\cdot(\gamma\vec{\tau}) + \gamma\bar{B}_f + S_p \ , \tag{4.5}$$

where

$$S_p = -\left[\frac{\gamma^2\mu}{a}\vec{u} + \gamma^3\frac{C_2}{2}\rho\,|\vec{u}|\,\vec{u}\right] \ , \tag{4.6}$$

where, γ is the porosity, a is the permeability, C_2 is the inertial resistance coefficient and $|\vec{u}|$ is the magnitude of the velocity. The parameters γ, a and C_2 come from the properties of the chosen material. For this study the porosity, the permeability and the inertial coefficient were set to 0.73, 8×10^{-6} and 1818.032 respectively, as these values were used in the work of Kang et al. [57].

4.5.2 Flow conditions

In order to investigate real-life situations, the flow conditions were chosen by statistical analyses from the Department for Transport in United Kingdom. Valuable data was provided focusing on the average vehicle speed on British highways in 2016, which is at 59,4 mph or 26.55411 m/s [58]. So, the car velocity was set to be this value making the present investigation necessary as information regarding the fuel efficiency will be provided for actual conditions. Furthermore, it is assumed that the car travels towards London using the M1 road which is the most used road in England. According to that, the wind speed and direction were selected from averaged measurements conducted by Lapworth and McGregor [59] and the Met Office statistics [60] respectively. So, a crosswind velocity of 7.5 m/s with an angle of 28.9^0 at 10m height was set leading to a yaw angle of 12.26^0.

Wind Tunnel Conditions

In the ideal conditions, the free-stream velocity was equal to the vehicle's speed at 26.55411 m/s and the turbulent properties were kept low. In detail, the turbulence intensity was set to be 0.5 as well as the turbulence length scale. These conditions replicate the ones of wind tunnel where the flow is uniform and turbulent perturbations hardly exist. The resulting Reynolds number is equal to $Re_L = 8.356 \times 10^6$ according to the length of the car, which is quite high as a full scale model is used. It is expected that the drag and lift forces will be smaller in these conditions as there are no significant perturbations in the air to affect them.

Crosswind velocity profile

For this case, a side wind was introduced at a speed of 7.5 m/s which results in a 12.26^0 yaw angle accounting the cruise speed. After many experimentations, it was decided to use high turbulent properties along with an implemented sheared wind profile. The sheared wind interferes with the velocity of the car leading to a higher Reynolds number, $Re_L = 9.716 \times 10^6$, as seen in figure 4.12. Inevitably, the free-stream velocity is increased

as it includes the velocity of the car and the x velocity component of the wind. For the sheared wind profile, the formulation of the atmospheric boundary layer that Deaves and Harris [61] implemented, was used and adjusted for x and y axis:

$$V_x = V_c + V_{w10_x} \frac{ln(z/z_0)}{ln(10/z_0)} , \tag{4.7}$$

$$V_y = V_{w10_y} \frac{ln(z/z_0)}{ln(10/z_0)} , \tag{4.8}$$

where z_0 is the terrain's aerodynamic roughness being equal to 0.03 for open terrains with isolated trees [63]. It is clearly seen that the above formulations are depending on the physical height z.

In order to replicate conditions from a real-world turbulent environment, fluctuations were introduced to the velocity field using turbulence intensities and length scales. The overall turbulence intensity is defined as:

$$I = \sqrt{\frac{1}{3}(I_x^2 + I_y^2 + I_z^2)} , \tag{4.9}$$

where I_x, I_y and I_z are the intensity values. The turbulence length scale L, which is expressed with the same formulation as turbulence intensity 4.9, is a quantity that shows the size of the eddies in the turbulent flow. In the present study, the values for these parameters were selected from the previous investigations of Duncan et al. [35], Wordley and Saunders [64] which are the following:

Turbulence Intensity
$I_x = I_y = 8\%$
$I_z = 0.136 \cdot I_x = 1.1\%$
I=6.56%
Turbulence length scale
$L_x = L_y = 4.6$ m
$L_x = 0.77 \cdot L_x = 3.542$ m
L=4.28 m

Table 4.5: Turbulent properties used for real-world conditions

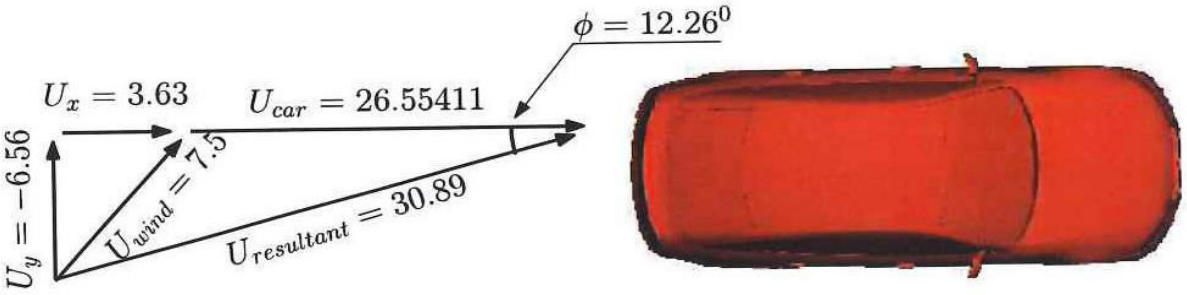

Figure 4.12: Implementation of side wind - Velocity components at 10m height

The following figure shows the velocity profiles in two axes. Since the formulations depend on the height z, the longitudinal and horizontal velocities are increased with the height z. In these conditions, it can be seen that the car experiences higher velocity (up to 29 m/s) than the wind tunnel conditions while the y velocity is increased by 4.5 m/s at the height of the car. It is worth mentioning that the horizontal velocity is implemented in such way so as to act on the car from right to left and thus it propagates on the negative values of Y axis.

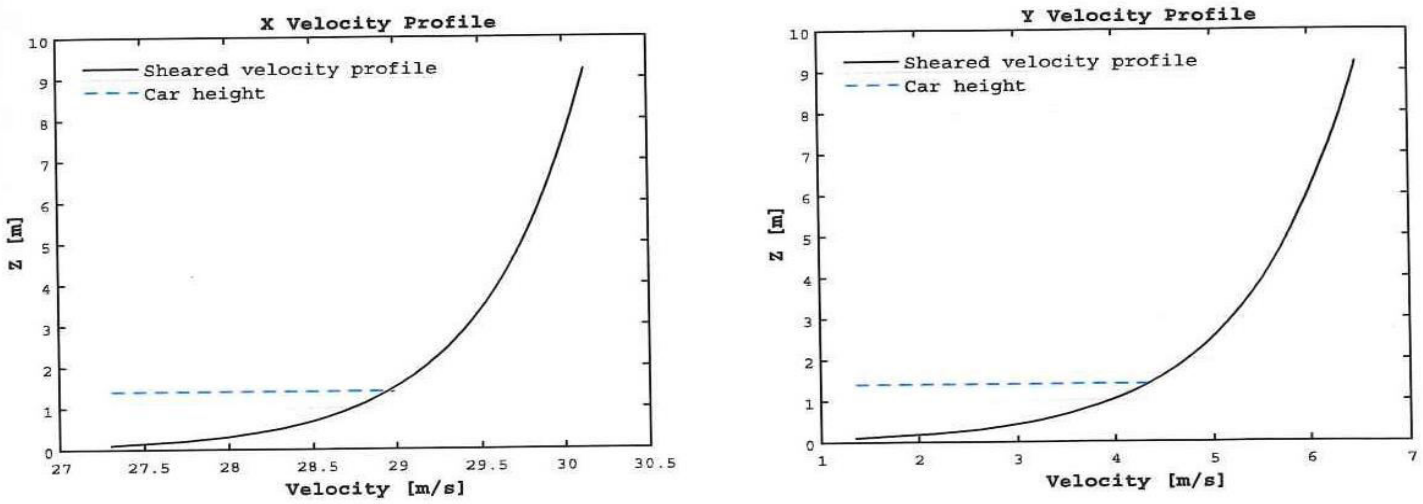

Figure 4.13: Velocity profiles in X and Y axes

4.6 Solver Setup

As mentioned previously, the pressure-based solver of ANSYS Fluent was used and the $k-\omega$ SST turbulence model was chosen due to its high accuracy as seen in the Literature. The pressure-velocity coupling was achieved using the Coupled scheme which is a fully implicit algorithm that solves the momentum and pressure equations together. The pressure gradients are discretized implicitly in the momentum equation providing an efficient and robust coupling [54]. Also, the gradients at the cells were calculated using the Green-Gauss Cell Based method which is the quickest and simplest method since the value of a cell is equal to the arithmetic average of the neighbouring cells' values. Regarding the spatial discretization, Second Order Upwind scheme was used for flow terms while First Order scheme was prescribed for the turbulent quantities for all cases. For the momentum terms, the Bounded Second Order Implicit scheme was integrated providing better stability and accuracy than the Second order Implicit scheme. Finally, the convergence criteria was set to 1×10^{-6} and the unsteady data sampling is discussed in the following section.

4.6.1 Simulation Strategy

Due to the fact that transient simulations are sensitive to initial conditions, the cases were initialized from a steady state and run 1000 iterations. Then, the Unsteady RANS scheme was activated and 7 flow passes were required so as the solution would be fully converged. The same thing applies to the IDDES scheme. Once it was activated, the solution was successfully converged after few flow passes and then data sampling took place for another 8 flow passes.

Since the RANS and URANS methods were not used for obtaining the final solution, First Order schemes were used for the temporal and spatial discretization of all terms apart from the pressure in which Second Order integration was chosen, leading to lower computational cost. For the IDDES method, higher order schemes were used and the overall setup can be seen in table 4.6.

For transient simulations, certain parameters had to be specified that affect strongly the solution. The most influential one is the size of the time step. If this value is high, then small vortices and perturbations can not be captured at all. From the Literature, there is a wide range of this value from 10^{-3} [34], [23], [38] to 8.8×10^{-6} [39]. For the present study, the size of the time step was set to 5.5×10^{-4} which is the same value that Ashton and Alistair [33] used and it is close to the value of 3.5×10^{-4} that was used in the more recent work of Simmonds et al. [30]. In the URANS approach this value was equal to 0.002 since priority was given to the fastest way of convergence and not the solution itself.

To sum up, in all cases the RANS approach was used at the beginning in order to obtain a converged solution and then the URANS and IDDES methods were activate. Due to the change in the time step from one approach to another, 850 time steps were needed in the IDDES approach so as the solution would be converged again. Henceforth, data sampling was enabled and data was averaged over 8 flow passes which corresponds to 1.375s.

	RANS	URANS	IDDES
Coupling p-v	Coupled	Coupled	Coupled
Time steps	1	600	3000
Iterations	1000	10	10
Gradients	Green-Gauss Cell Based	Green-Gauss Cell Based	Green-Gauss Cell Based
Pressure scheme	Second Order	Second Order	Second Order
Momentum scheme	First Order Upwind	First Order Upwind	Bounded Central Differencing
Turbulent eqs. scheme	First Order Upwind	First Order Upwind	First Order Upwind
Temporal scheme	-	First Order Implicit	Bounded Second Order Implicit

Table 4.6: Summary of the setup that was followed throughout all simulations

Chapter 5

Results and Discussion

Experiments have not been conducted for the present conditions, so a comparison analysis can not be undertaken. However, the spacing of the grid was assessed as a grid sensitivity study was conducted. The obtained results are discussed in this section in the form of comparisons of different parameters. Body forces, coefficients and pressure distributions are firstly obtained while the differences between wheel models and flow conditions are discussed critically.

5.1 Grid Sensitivity study

Firstly, the Grid Convergence Index (GCI) method was undertaken in order to value the credibility of this project and to find the amount of confidence in the results. This method was introduced by Roache [62] in 1997 and it provides a consistent way of reporting results with an error band on the grid convergence of the solution. A restriction of this method is the fact that the grid refinement ratio must be constant. Despite the complexity of the unstructured grids, a constant refinement ratio was achieved:

$$r = \frac{h_2}{h_1} = \frac{h_3}{h_2} \approx 1.29 \ . \tag{5.1}$$

This study was performed using the values of drag and lift coefficients. The observed

convergence rate is expressed as:

$$p = \frac{ln(\frac{f_3 - f_2}{f_2 - f_1})}{ln(r)} \quad , \tag{5.2}$$

where f_i is the value of coefficients obtained by different grids with f_1 being the solution obtained by the finest grid. The relative error between the solutions of different meshes is calculated as:

$$\varepsilon_{i,i+1} = \frac{f_i - f_{i+1}}{f_i} \quad . \tag{5.3}$$

The Grid Convergence Index (GCI) for the fine and coarse grids is expressed as:

$$GCI_{fine} = \frac{F_s \left|\varepsilon_{1,2}\right|}{(r^p - 1)} \quad , \tag{5.4}$$

$$GCI_{coarse} = \frac{F_s \left|\varepsilon_{2,3}\right| r^p}{(r^p - 1)} \quad , \tag{5.5}$$

where F_s is a safety factor with a constant value equal to 1.25 given by Roache. Theoretically, as the grid is refined, the discretization errors are reduced approaching asymptotically zero. So, if all values are within the asymptotic range of convergence, the following ratio should be:

$$R = \frac{GCI_{coarse}}{r^p GCI_{fine}} \quad . \tag{5.6}$$

This study was performed using the wind tunnel conditions and the MRF wheel modelling technique. Table 5.1 shows the values obtained by the grids and the results from the GCI study. As mentioned above, lift and drag coefficients were calculated for this study in order to be confident for the convergence of the solution.

Coefficients	Coarse	Medium	Fine	GCI_coarse	GCI_fine	R
Lift	0.0223	0.0188	0.0176	8.33	2.46	0.94
Drag	0.261	0.2786	0.2823	1.89	0.36	1.01

Table 5.1: Values of drag and lift coefficient obtained by different grids

It can be seen that the solutions are well within the asymptotic range of convergence for drag coefficient but not for the lift coefficient. Since the values of lift coefficient are very low and close, this case does not represent the dependency of the grid. On the other hand, the differences in drag values are significant making this case grid dependent. Moreover, finer grids have produced more accurate results as seen from previous studies, and thus the fine mesh was selected for further simulations.

5.2 Body Forces and Distribution

Lift and drag forces are presented in this section using all three wheel modelling techniques and two flow conditions. Due to the fact that the Reynolds number is different in each flow condition, the distribution of forces is obtained by body forces instead of their coefficients. In the realistic scenario, it is expected that the forces will be higher since the turbulent properties are increased and further perturbations are added on the flow.

5.2.1 Comparison of different wheel models

The techniques that were described in section 4.1 are examined in the present section. Even though this work is focused on differences between the MRF and SM methods, the RWBC was used as well for the coarse grid due to limited resources. From the Literature, it can be seen that this method is appropriate for obtaining body forces and coefficients but some flow structures are not present in the flow field [25], [27]. Therefore, only body forces are provided while the flow field is analysed with the MRF and SM techniques. The present section focuses on the differences of wheel modelling techniques while the effect of flow conditions will be discussed in section 5.2.2.

In order to see the bigger picture, the following figure provides the most representative variables from which the effect of each wheel model can be detected. Evidently, it can be seen that each wheel modelling technique affects differently the overall performance of the car. Firstly, no certain pattern can be detected even though the MRF technique

seems to produce results which are in between the RWBC and SM methods. Moreover, each model affects the car in all directions since car's moments change with each wheel modelling technique.

In detail, the drag coefficient is equal to 0.27 approximately for RWBC and SM method while the lift coefficient is close to 0.016 for MRF and SM techniques in the ideal scenario. Furthermore, all coefficients of moments are close with the exception of yaw moment in which the RWBC method produce higher results. The same pattern is detected in the side force coefficient as well. In the realistic case, the MRF and SM methods produce comparable results with the drag coefficient being 0.36 approximately and the side force coefficient taking the value of 0.22 using all models. However, significant differences are detected in the lift coefficient where its value is the lowest with the SM method and highest with the RWBC. All models produce similar results regarding the coefficients of moments but the roll moment has been predicted significantly higher in RWBC method. All in all, the obtained results are comparable but the RWBC showed that great discrepancies can be noticed at specific variables making it more sensitive to certain aspects.

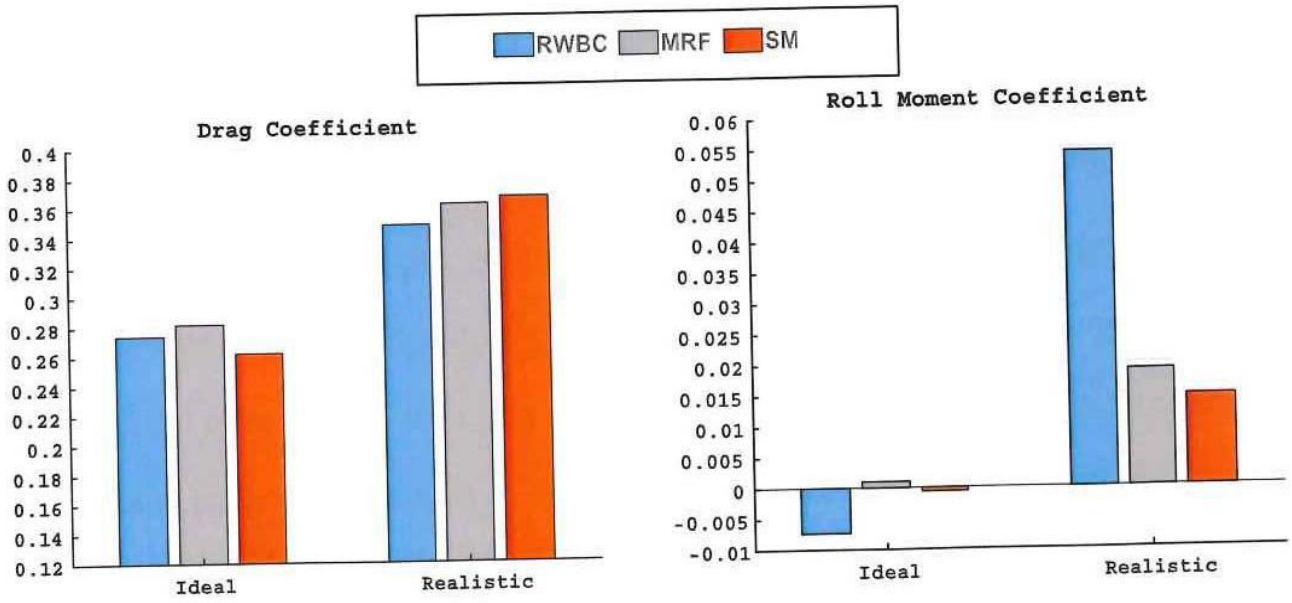

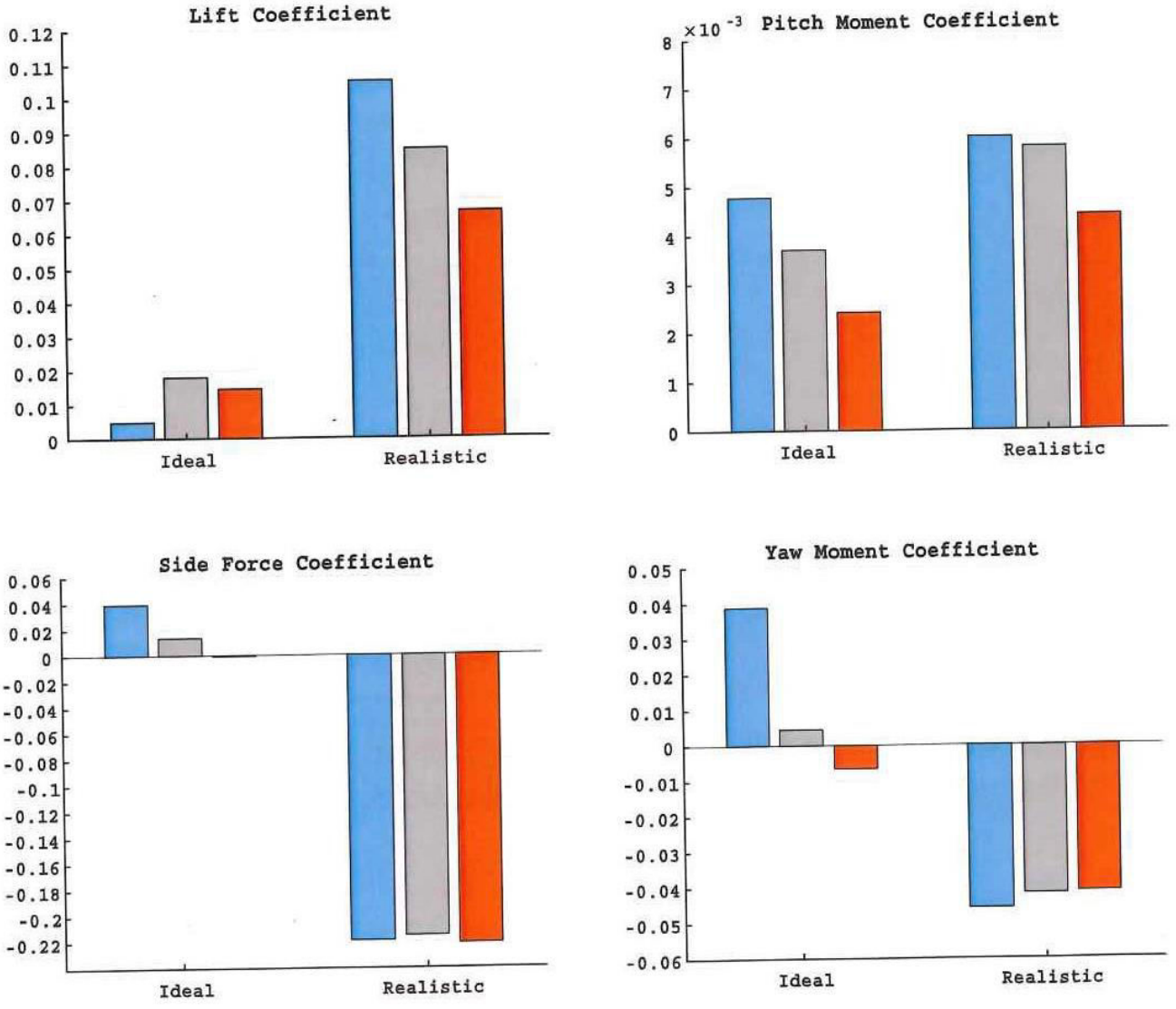

Figure 5.1: Bar charts of body forces, moments and side force coefficients comparing all three modelling techniques

In order to examine the forces in depth and provide more information, the influence of each wheel modelling technique can be noticed by studying each part of the car separately. As mentioned in section 4.3, the car is separated into many regions so as to investigate the behavior of certain parameters. Moreover, providing information regarding the effect of each part is essential on automotive applications. Therefore, the following tables help to understand the influence of each part as well as how significant the differences on the wheels are using each wheel model.

Parts	RWBC	MRF	SM	Deltas		
				$\Delta_{RWBC-MRF}[\%]$	$\Delta_{RWBC-SM}[\%]$	$\Delta_{MRF-SM}[\%]$
Main Body	67.94	66.16	56	17.5	17.6	15.3
Rear End	50.1	52.76	51.87	5	3.4	1.7
Underbody-Engine bay	77	80.1	70.2	4	8.8	12.3
Front right wheel	13.32	14.9	13.63	4.92	2.1	8.7
Front left wheel	14.51	15.65	14.3	7.3	1.5	8.6
Rear right wheel	6.12	7.36	8.87	16.8	31	17
Rear left wheel	7.34	7.73	9.3	5	21	16.9
Mirrors	10.81	12.11	12	10.7	10	9
Total	256.8	264.28	252.1	2.8	1.8	4.6

Table 5.2: **Drag** values of different parts using all wheel models in **ideal** conditions - Obtained absolute relative errors indicate the differences between wheel modelling techniques

Parts	RWBC	MRF	SM	Deltas		
				$\Delta_{RWBC-MRF}[\%]$	$\Delta_{RWBC-SM}[\%]$	$\Delta_{MRF-SM}[\%]$
Main Body	72.86	76.67	76.96	4.9	5.3	0.4
Rear End	71.5	71.51	71.96	0.01	0.6	0.6
Underbody-Engine bay	82.3	85.8	85.9	4	4.2	0.01
Front right wheel	14.74	18.82	16.2	21.7	9	9
Front left wheel	20.54	21.19	21.8	3.1	5.8	2.8
Rear right wheel	16.52	25.65	21.55	48.9	35.6	15.9
Rear left wheel	13.1	16.48	14.6	20.5	39.2	11.4
Mirrors	11.37	11.98	13.52	5.1	22.1	11.4
Total	326.05	339.26	343.48	3.9	5	1.2

Table 5.3: **Drag** values of different parts using all wheel models in **realistic** conditions - Obtained absolute relative errors indicate the differences between wheel modelling techniques

In order to be completely confident with the effect of each wheel model, drag values are presented for both flow conditions. Firstly, it is clearly seen that the MRF and SM methods produce comparable results in the realistic scenario while, on the other hand,

the picture is blurred regarding the ideal conditions as all values are close. This indicates that the RWBC is more sensitive to certain flow conditions than the other two modelling approaches. Secondly, each model affects all parts of the car from the biggest ones, such as the main body, to even the smallest ones, such as the mirrors. The absence of experimental data leads to the inability of calculating the actual errors but the models are compared with each other with the SM method being the most trustworthy one according to previous studies and its "more realistic" behavior.

Going into more depth, the main body, the engine bay and the underbody are strongly affected by the SM method in the ideal case, while the noticed differences are smaller in the wheels. MRF and RWBC methods have similar behavior except in the engine bay and the underbody where the drag is higher with the former technique. Also, the RWBC method agrees well with the SM one regarding the drag values in the front wheels while the difference is significantly increased in the rear ones. The reason lies in the fact that the generated flow fields are unlike and as the flow is propagating to the rear, different drag values are obtained. The same applies on the MRF method but on a smaller level. In the realistic scenario, the drag values are close on the main body, rear end, engine bay and underbody but the RWBC method produce significantly different results on the wheels. The MRF and SM methods seem to behave similarly in these conditions with the biggest differences noticed at the rear wheels. Finally, another proof of unlike generated flow fields is the fact that the drag is predicted lower in the mirrors using the RWBC method than the other two models for both flow conditions.

Parts	RWBC	MRF	SM	Deltas		
				$\Delta_{RWBC-MRF}[\%]$	$\Delta_{RWBC-SM}[\%]$	$\Delta_{MRF-SM}[\%]$
Main Body	264.3	270.5	271.5	2.3	2.65	0.3
Rear End	408.94	412.63	413.6	0.9	1.1	0.2
Underbody-Engine bay	-670.24	-681.1	-758.7	1.6	11.6	10.2
Front right wheel	3.1	3.63	4.92	14.6	36.9	26.2
Front left wheel	2.28	2.92	3.48	21.9	34.5	16
Rear right wheel	2.8	4.53	4.56	38.2	38.6	0.6
Rear left wheel	3.14	4.37	4.1	28.1	23.4	6.2
Mirrors	-2.92	-2.53	-2.1	13.3	28	16.9
Total	4.6	16.8	13.68	72.6	66.3	18.5

Table 5.4: **Lift** values of different parts using all wheel models in **ideal** conditions - Obtained absolute relative errors indicate the differences between wheel modelling techniques

Parts	RWBC	MRF	SM	Deltas		
				$\Delta_{RWBC-MRF}[\%]$	$\Delta_{RWBC-SM}[\%]$	$\Delta_{MRF-SM}[\%]$
Main Body	347.44	347.83	343.18	0.1	1.2	1.3
Rear End	542.83	537.63	541.34	0.9	0.3	0.7
Underbody-Engine bay	-766.2	-820.55	-830.31	6.6	7.7	1.1
Front right wheel	-0.6	0.01	0.73	101.6	182.2	98.6
Front left wheel	1.28	2.93	4.36	56.3	70.6	32.8
Rear right wheel	1.56	5.57	3.62	71.9	56.9	35
Rear left wheel	-0.14	-1.74	-0.7	91.9	80	58.8
Mirrors	-2.74	-1.4	-1.81	52	38	22.6
Total	98.2	79.66	62.32	18.88	36.5	21.77

Table 5.5: **Lift** values of different parts using all wheel models in **realistic** conditions - Obtained absolute relative errors indicate the differences between wheel modelling techniques

As far as the lift values concern, the MRF and SM methods have similar behavior in both flow conditions. All models produced similar results regarding the main body, rear end, engine bay and underbody but significant differences are noticed in the wheels.

Once again, the obtained lift values of the rear wheels using the RWBC are undoubtedly different from the other methods, especially in the realistic scenario. Oddly enough, the lift values in the rear wheels using the MRF method agree well with the ones from the SM method. Even though the relative errors are huge in the wheels in realistic conditions, the values are quite close because they are small numbers. All in all, obtaining the differences in lift values makes it clearer that the MRF and SM methods have produced comparable results while the acted forces on wheels are significantly different in the RWBC method.

The above study proves that the RWBC method can be considered as adequate to produce comparable results especially in the calculation of drag. However, some flow features are not present in this method since it only allows the generation of the appropriate boundary layer around the wheels and thus making it sensitive to flow conditions. The MRF method produce results that agree well with the SM ones in some cases and a more thorough study is undertaken below to obtain their differences. Overall, all parts of the car are affected by the wheel models with the main body being the most affected and the rear end the least one.

5.2.2 Comparison of flow conditions

As mentioned above, two flow conditions were implemented and their differences are discussed in this section. Firstly, figure 5.2 shows how the realistic conditions have affected the car using each wheel modelling method. It is clearly seen that all values have changed dramatically with the side force coefficient being the most affected. Generally, the drag coefficient has increased by 22% approximately while an 80% increase is noticed in the lift coefficient. Since the realistic scenario involved the implementation of a crosswind and the resulted horizontal velocity is five times greater, it was expected that the side force coefficient and yaw moment would be increased radically.

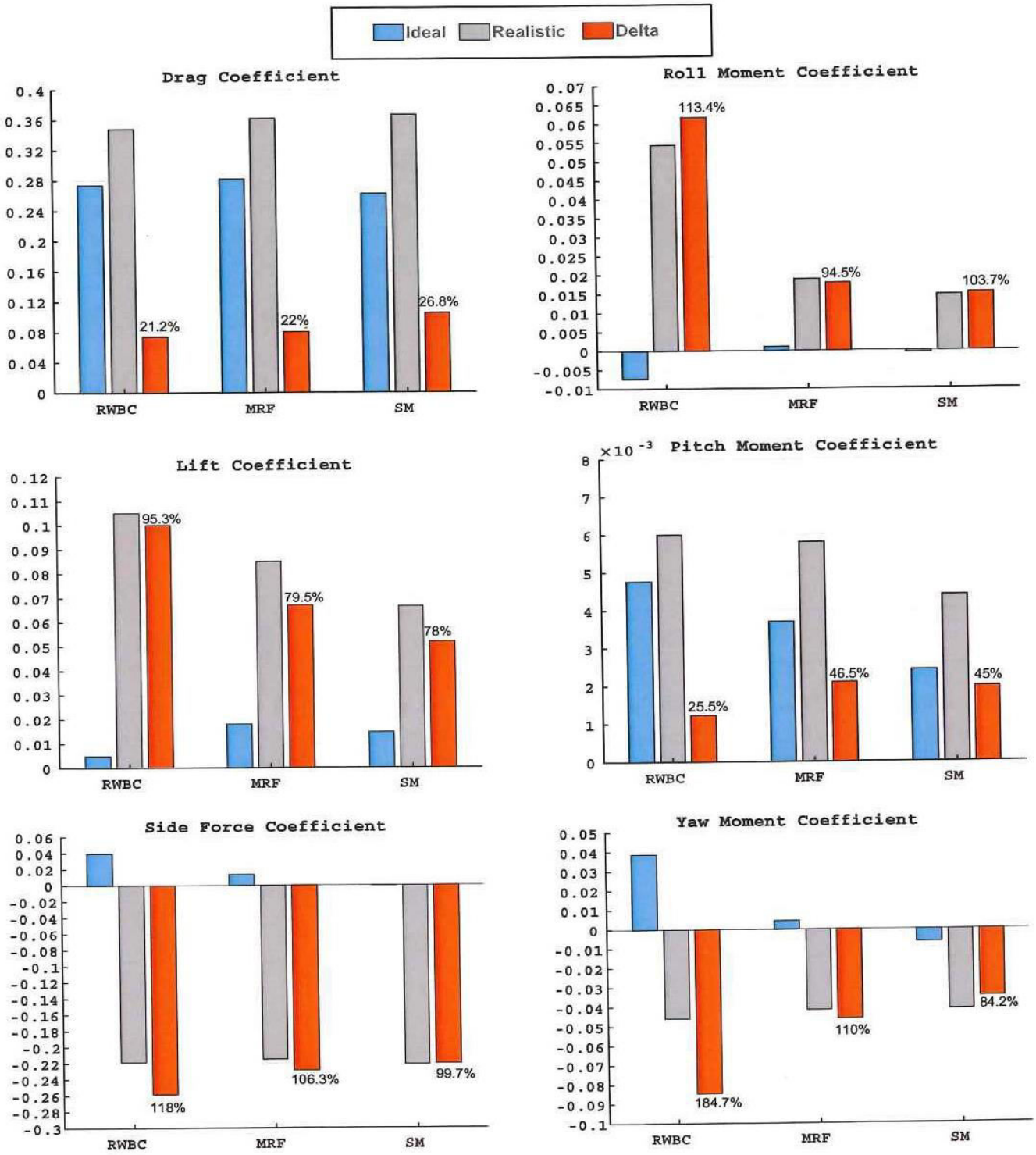

Figure 5.2: Bar charts of body forces, moments and side force coefficients comparing two airflow conditions - The differences are also presented in percentages

Using the RWBC method, the real-world conditions have affected immensely the lift values with an overall increase of 95% being noticed, as seen in table 5.6. The biggest differences are noticed in the front right and rear left wheels while the lift force in the main body and rear end have increased by 1/5 approximately. Also, the rear wheels and rear end seem to have been strongly affected by these conditions as the drag in the formers

have increased greatly while an increase of 30% is noticed in the latter.

Parts	Ideal		Realistic		Deltas	
	Drag	Lift	Drag	Lift	$\Delta_{C_D}[\%]$	$\Delta_{C_L}[\%]$
Main Body	67.9	264.3	72.86	347.44	6.7	23.9
Rear End	50.1	408.94	71.5	542.83	29.9	24.6
Underbody-Engine bay	77	-670.24	82.3	-766.2	6.4	12.5
Front right wheel	13.32	3.1	14.74	-0.6	9.6	119.3
Front left wheel	14.51	2.28	20.54	1.28	29.3	43.8
Rear right wheel	6.12	2.8	16.52	1.56	62.9	44.3
Rear left wheel	7.34	3.14	13.1	-0.14	76	104.4
Mirrors	10.81	-2.92	11.37	-2.74	4.9	6.1
Total	256.8	4.6	326.05	98.2	21.2	95.3

Table 5.6: **Drag** and **Lift** values of different parts using the **RWBC** wheel model in both conditions - Obtained absolute relative errors indicate the differences between flow conditions

Parts	Ideal		Realistic		Deltas	
	Drag	Lift	Drag	Lift	$\Delta_{C_D}[\%]$	$\Delta_{C_L}[\%]$
Main Body	66.16	270.5	76.67	347.83	13.7	22.2
Rear End	52.76	412.63	71.51	537.63	26.2	23.2
Underbody-Engine bay	80.1	-681.1	85.8	-820.55	6.6	17
Front right wheel	14.9	3.63	18.82	0.01	20.8	99.7
Front left wheel	15.65	2.92	21.19	2.93	26.1	3.4
Rear right wheel	7.36	4.53	25.65	5.57	71.3	18.7
Rear left wheel	7.73	4.37	16.48	-1.74	53	139.8
Mirrors	12.11	-2.53	11.98	-1.4	1	44.6
Total	264.28	16.8	339.26	79.66	22.1	78.9

Table 5.7: **Drag** and **Lift** values of different parts using the **MRF** wheel model in both conditions - Obtained absolute relative errors indicate the differences between flow conditions

In the MRF method, the lift force have increased by 78.9% with the main body and rear end contributing the most to it. In detail, an overall 20% increase is noticed in both parts while the front right and rear left wheels have been significantly affected as well. Also, the drag force has been increased greatly and the behavior of the rear end and rear wheels have changed dramatically.

Similar results are obtained by the use of the SM method in which the overall forces have been increased dramatically. An increase of more than 1/4 is noticed in the drag of the main body and rear end while more drag is generated by all wheels. Furthermore, big differences are noticed in the lift generated by the front right and rear left wheels while the rear end's lift have been increased by 1/5 approximately.

Parts	Ideal		Realistic		Deltas	
	Drag	Lift	Drag	Lift	$\Delta_{C_D}[\%]$	$\Delta_{C_L}[\%]$
Main Body	56	271.5	76.96	343.18	27.2	20.9
Rear End	51.87	413.6	71.96	541.34	27.9	23.6
Underbody-Engine bay	70.2	-758.7	85.9	-830.31	18.2	8.6
Front right wheel	13.63	4.92	16.2 ,	0.73	15.8	85.1
Front left wheel	14.3	3.48	21.8	4.36	34.4	20.1
Rear right wheel	8.87	4.56	21.55	3.62	58.8	20.6
Rear left wheel	9.3	4.1	14.6	-0.7	36.3	117
Mirrors	12	-2.1	13.52	-1.81	11.2	13.8
Total	252.1	13.68	343.48	62.32	26.6	78

Table 5.8: **Drag** and **Lift** values of different parts using the **SM** wheel model in both conditions - Obtained absolute relative errors indicate the differences between flow conditions

All in all, the differences between the two conditions are significant with the lift force being strongly affected. In real-world conditions, the body forces of the main body and rear end have been increased for all wheel modelling techniques. Also, a slight increase in the drag generated by the engine bay has been noticed but most importantly the already

negative lift has been reduced even more in the realistic conditions. The reason of this effect is explained in section 5.6. The generated drag of the wheels has been increased overall but important differences are noticed in the lift. The front right tyre produce a lot less lift while negative lift is generated by the rear left tyre using all wheel models. As the crosswind meets the right side of the car first, unsteady turbulent features are formed in the left side and thus affect the left side parts accordingly.

5.2.3 Forces Distribution

In automotive aerodynamics, it is important to detect the forces that different parts generate in order to be able to re-design them appropriately. Therefore, the following figures show the distribution of forces of all parts that constitute the car.

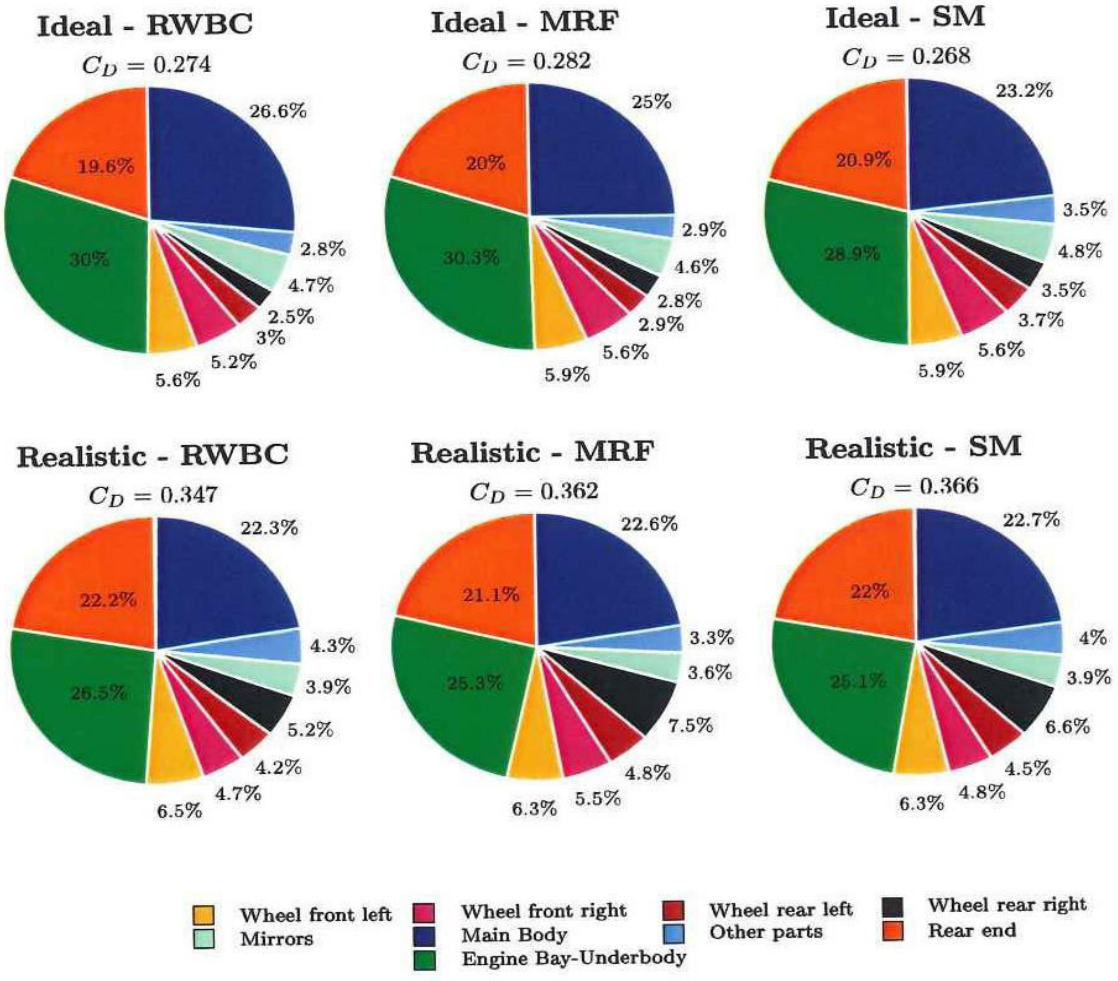

Figure 5.3: Drag force distribution amongst all parts of the car using all wheel modelling techniques as well as two flow conditions

Regarding the drag force, it is clearly seen that the engine bay along with the underbody contributes the most while half of the total drag comes from the main body and rear end combined. In the ideal conditions, the distribution of drag in the wheels is the same in all models but the RWBC model produced results proving that the main body contributes more to the total drag than the other two models. Also, the lowest percentage of engine bay's contribution is noticed in the SM method which is slightly less than the MRF's one. In the realistic scenario, the engine bay contributes less than the ideal case while the contributions of the main body and rear end have been increased marginally. The most important thing that can be noticed is the fact that the front left and rear right wheels generate more drag due to the crosswind's direction and thus their contributions to the overall drag are increased for all wheel models. It is worth mentioning that there are other parts in the car that generate drag such as the grilles, but their values are not as important.

Parts	Ideal			Realistic		
	RWBC	MRF	SM	RWBC	MRF	SM
Main Body	264.3	270.5	271.5	347.44	347.83	343.18
Rear End	408.94	412.63	413.6	542.83	537.63	541.34
Underbody-Engine bay	-670.24	-681.1	-758.7	-766.2	-820.55	-830.31
Total	4.6	16.8	13.68	98.2	79.66	62.32

Table 5.9: **Lift** values of the parts that contribute the most using all wheel models in both conditions

The above table shows the parts that contribute the most to the lift force. As can be seen, a huge amount of lift is generated by the main body and rear end but it is almost neutralized by the engine bay. This happens in all cases for all wheel modelling techniques with the difference being the fact that the values are greater in the realistic conditions. Also, this shows that the contribution of wheels and mirrors is significantly less.

5.3 Computational Cost

It has been proven that the sliding mesh method requires more computational resources than the MRF and RWBC. The following table provides the computational cost of each grid and wheel method. The computational time is given as a function of the time required for the shortest simulation. Indeed, the cost of the SM is almost two times higher than the MRF method while the cost of this method is slightly higher than the RWBC for the same grid.

Grids	RWBC	MRF	SM
Coarse	1	1.15	-
Medium	-	1.83	-
Fine	-	3.21	5.2

Table 5.10: Computational cost

5.4 Pressure coefficient distribution

All of the studies that have investigated the DriVaer, presented plots of pressure coefficient at the walls of the car. The pressure coefficient provides valuable information as flow separation and other features can be detected. So, the distribution of pressure coefficient in different slices is presented in figure 5.4. From the distribution of the upper surfaces, it can be deducted that flow separation occurs in the region where the bonnet meets the windscreen and at the rear window as well. The velocity takes its maximum value at the the end of the windscreen where the C_p is the lowest. The short changes on the distribution in the rear window indicate that the separation of the flow is happening smoothly while no big differences are seen between the two flow conditions. However, the distribution of the pressure coefficient at the sides proves that the flow is accelerated in the last half of the car from the right side and decelerates in the left side showing that the crosswind comes from the right side of the car. As the flow is moving to the rear, the distributions of

the two flow conditions are close.

An important conclusion that can be deducted is the fact that the use of a specific wheel modelling technique affect slightly the flow at the rear window of the car. In the SM method, the flow separation at the rear window happens more abruptly than in the MRF method. Also, the unsteadiness in the distribution at the sides indicate the presence of vortices and turbulent phenomena. Even though SM and MRF methods produce similar results, small differences can be seen as unlike flow fields are generated by the models.

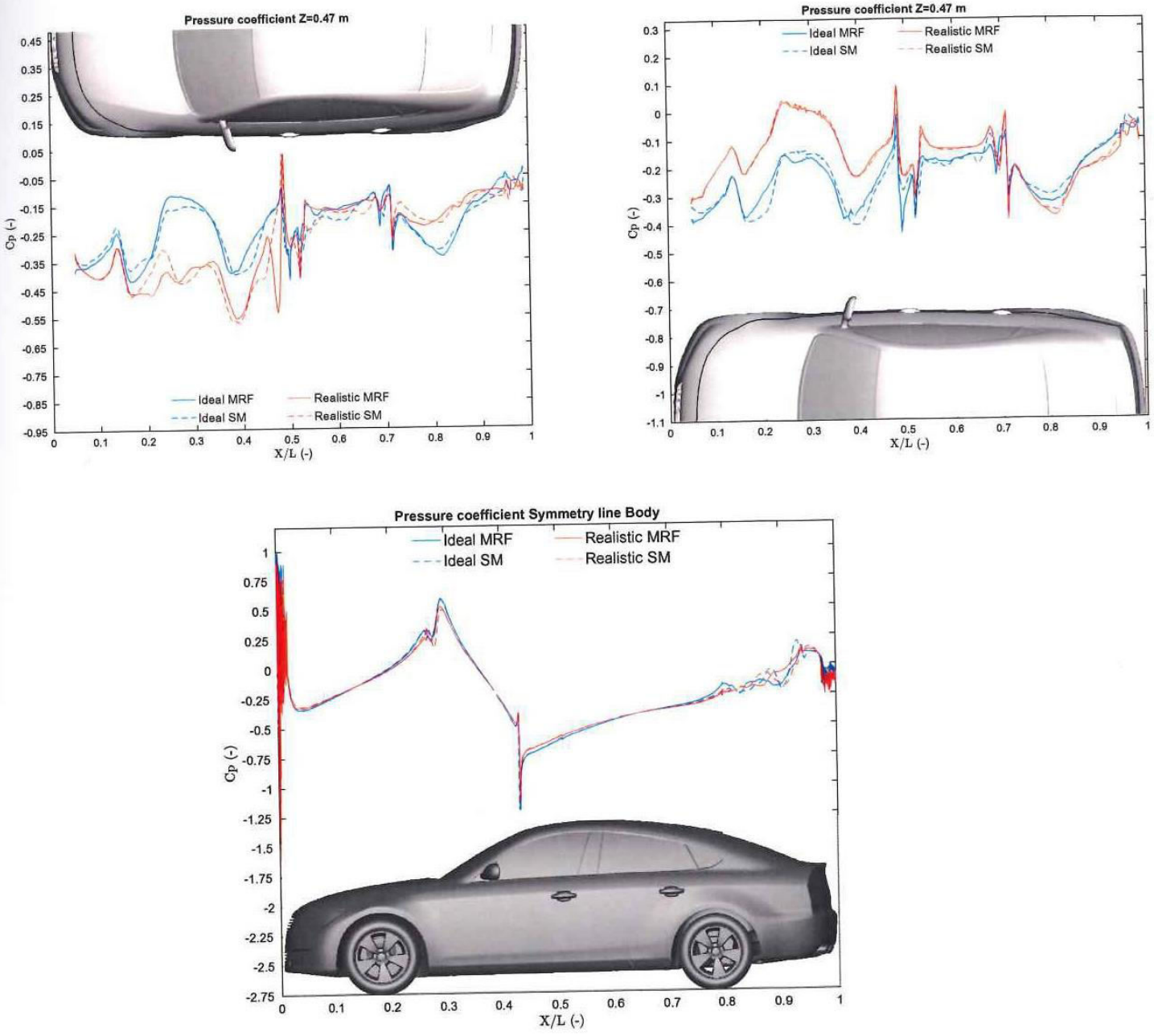

Figure 5.4: Pressure coefficient distribution obtained at slice Z=0.47 in the upper pictures and at the middle of the car in the lower one

5.5 Investigation of wheel models

In order to further study the differences between the wheel modelling techniques, the following figures provide valuable information regarding their differences. Initially, the pressure coefficient obtained at the wheels helps to identify how the flow behaves. As seen in figure 5.5, the distribution of pressure coefficient has been significantly changed at the rims. The rotation of the rim in the SM method can be clearly noticed as the the C_p has taken negative values in some regions of the rim. Also, the influence of the realistic conditions is greatly obtained at the front left wheel where the pressure coefficient is really low and thus justifying the differences obtained above in body forces. Moving to the rear wheels, the pressure is higher since the flow is disturbed and both conditions seem to affect these parts in the same way. However, the most important thing that can be noticed is the fact that the tyres are affected by the wheel model itself as different flow structures generated by each model.

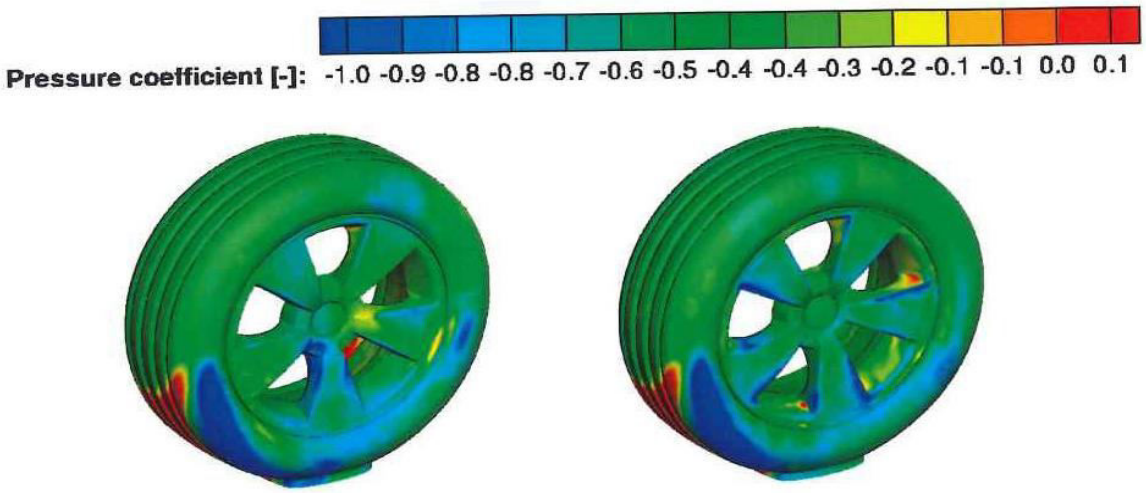

(a) Front left wheel: Ideal conditions with MRF(left) and SM(right) methods

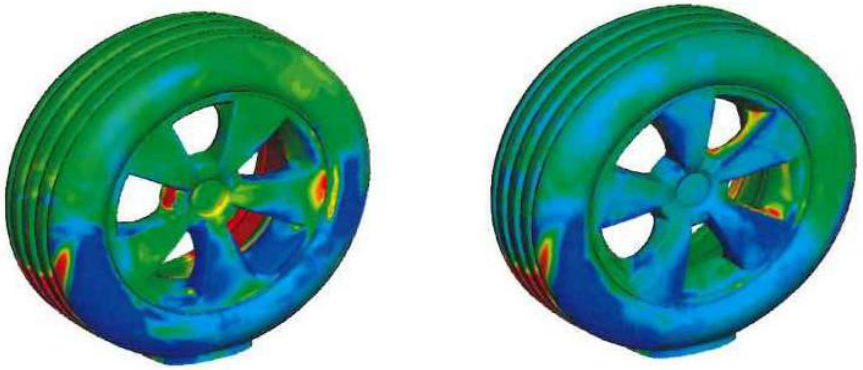

(b) Front left wheel: Realistic conditions with MRF(left) and SM(right) methods

]

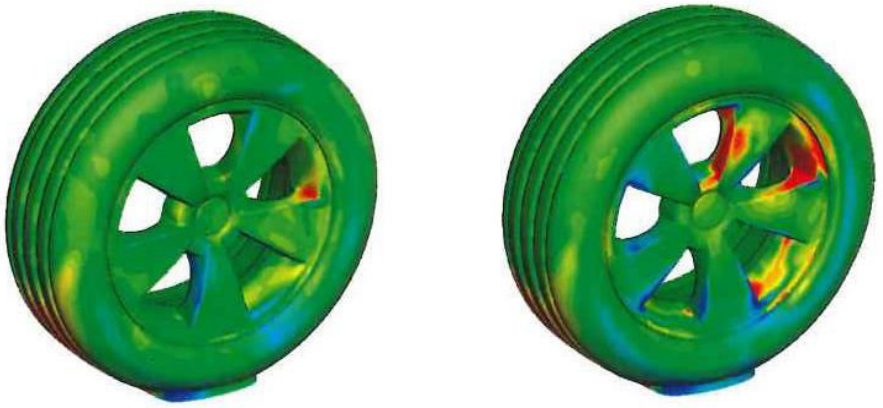

(c) Rear left wheel: Ideal conditions with MRF(left) and SM(right) methods

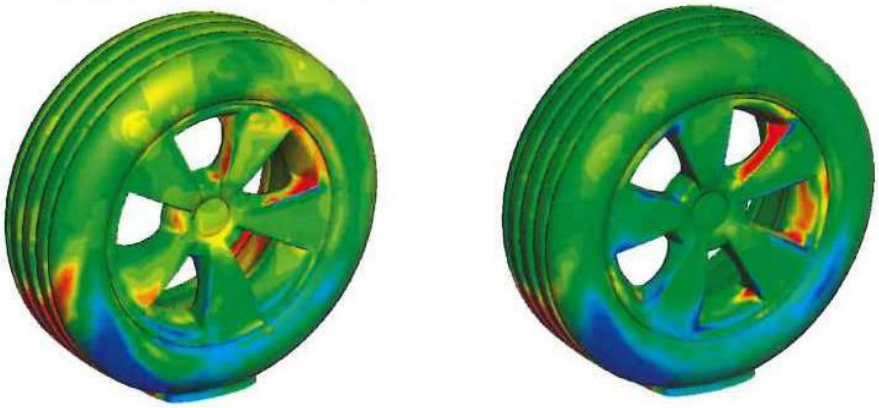

(d) Rear left wheel: Realistic conditions with MRF(left) and SM(right) methods

Figure 5.5: Pressure coefficient distribution at front and rear left wheel using two wheel models and two flow conditions

The following figure shows the velocity magnitude contour in a slice that passes from the centre of the wheels in order to understand better the influence of each wheel model. In both flow conditions, lower velocity field is generated around the front wheel using the SM method as well as less turbulent structures are present in the rear as seen clearly in the ideal conditions in which the wake is slightly lower. Moreover, as mentioned above, the flow structures generated by the wheels seem to dissipate quickly in the realistic conditions which makes the differences between wheel models less significant. The wake of the car is significant longer at these conditions and stronger since the velocity magnitude is equal to 0 in a larger area.

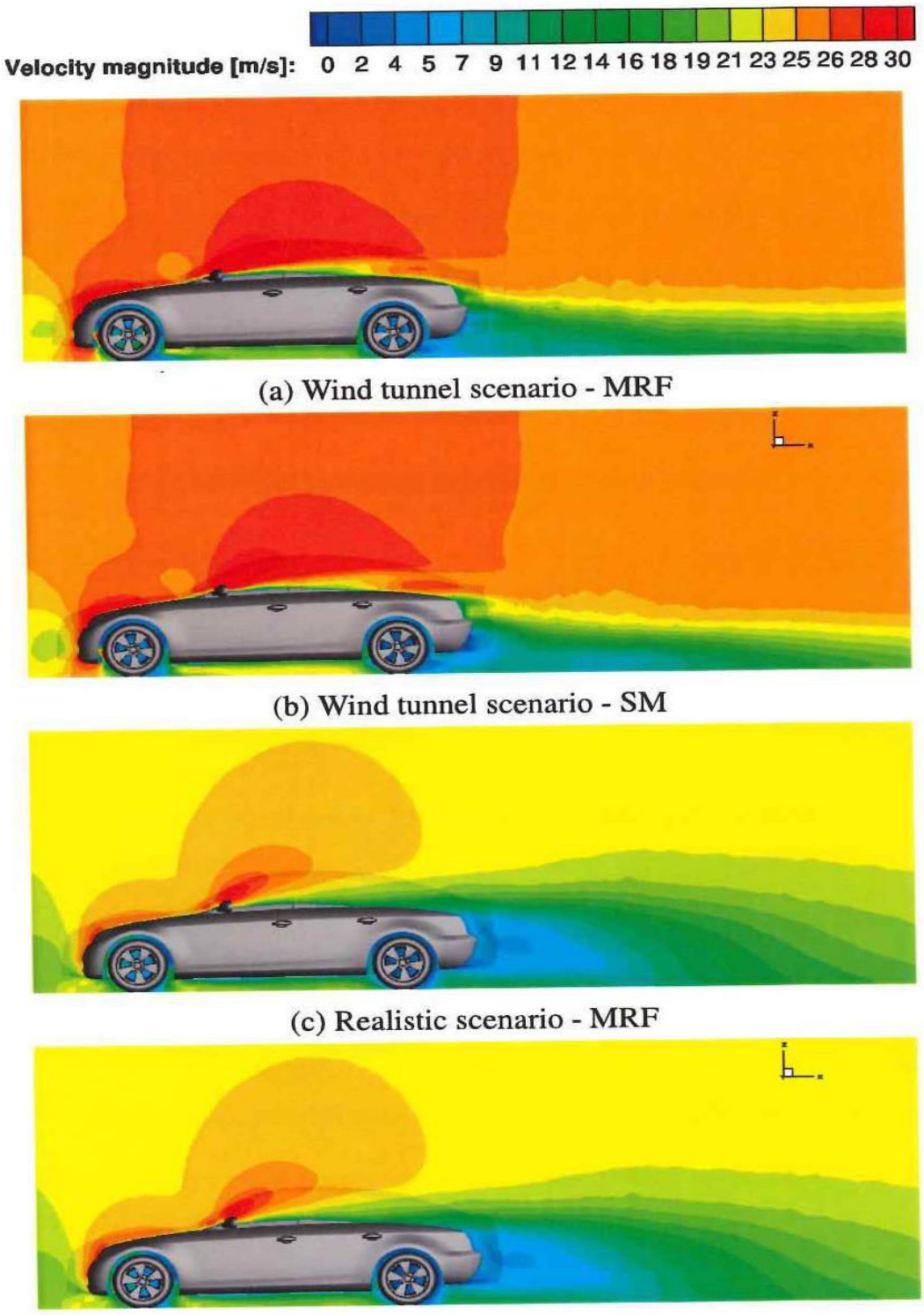

(a) Wind tunnel scenario - MRF

(b) Wind tunnel scenario - SM

(c) Realistic scenario - MRF

(d) Realistic scenario - SM

Figure 5.6: Velocity magnitude contour at Y = -0.76 m - Comparison between MRF and SM method as well as realistic and ideal conditions

A further proof of different generated flow structures by wheel models is seen in the following figure. The skin friction coefficient is presented and basically it shows the force exerted on the car's surfaces. The C_f is high at the rims when the SM method is applied due to the rotation of the mesh. In the MRF method, the flow moves faster towards the

underbody while the C_f at the sides of the car indicate the presence of different flow features. Also, the SM method seems to produce vortices that remain close to the ground and propagate out of the car faster as the flow passes towards the rear while lower values of C_f are detected close to the middle of the rear doors in the MRF method. This suggests that vortices remain attached to the car. Furthermore, the C_f is lower in the realistic scenario as the flow moves slower at the left side because of the direction of the wind but the influence of the wheel models can be noticed.

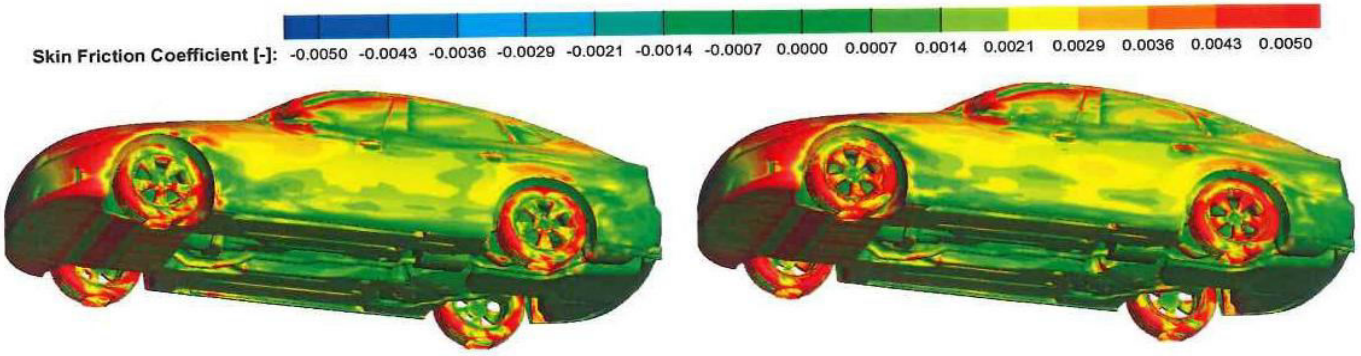

(a) Ideal conditions - MRF(left) and SM(right) methods

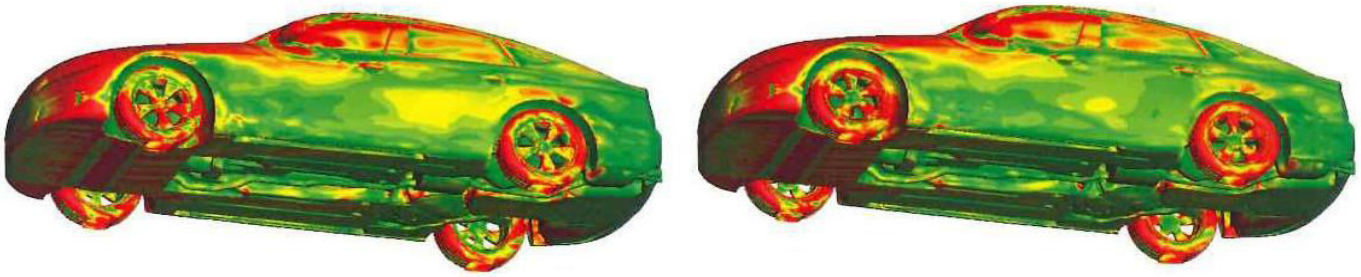

(b) Realistic conditions - MRF(left) and SM(right) methods

Figure 5.7: Skin friction coefficient in the main body and underbody - Comparison between wheel modelling techniques

Finally, the picture is complete when iso-surfaces of pressure coefficient are presented. The more realistic wheel model (SM) seem to produce appropriate flow features due to the rotation of the rims while the MRF method trys to generate similar flow field with small differences. In the ideal scenario, the turbulent flow is close to the ground and the underbody when the SM method is applied while the side of the car is affected greater using the MRF method. In real-world conditions, the turbulent flow takes larger area making the two models to behave similarly. In both conditions, the rear wheels are affected slightly more with the SM method. It is worth mentioning that the lower the values of

total pressure are, the more vorticity is achieved in the flow.

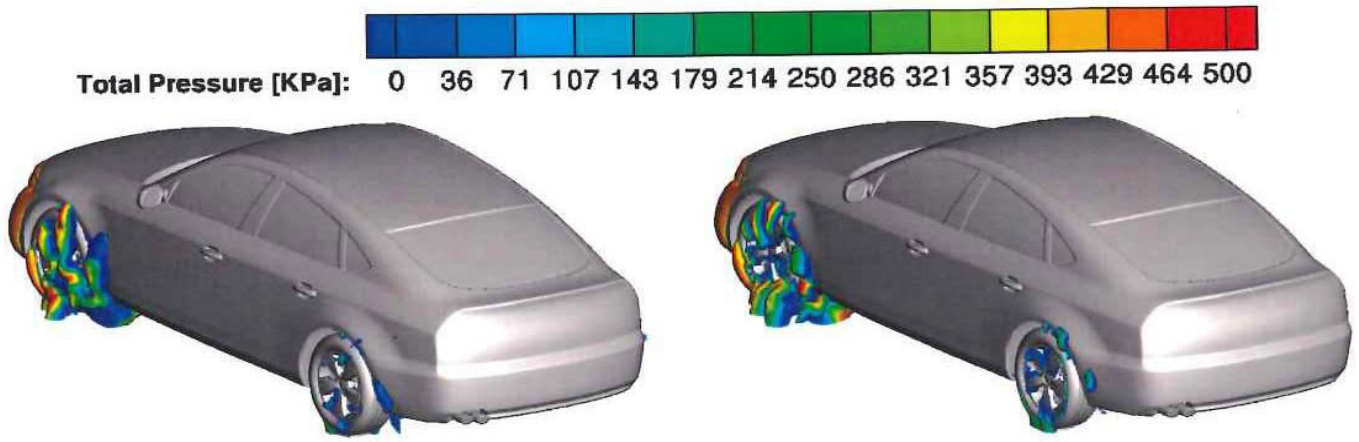

(a) Ideal conditions - MRF(left) and SM(right) methods

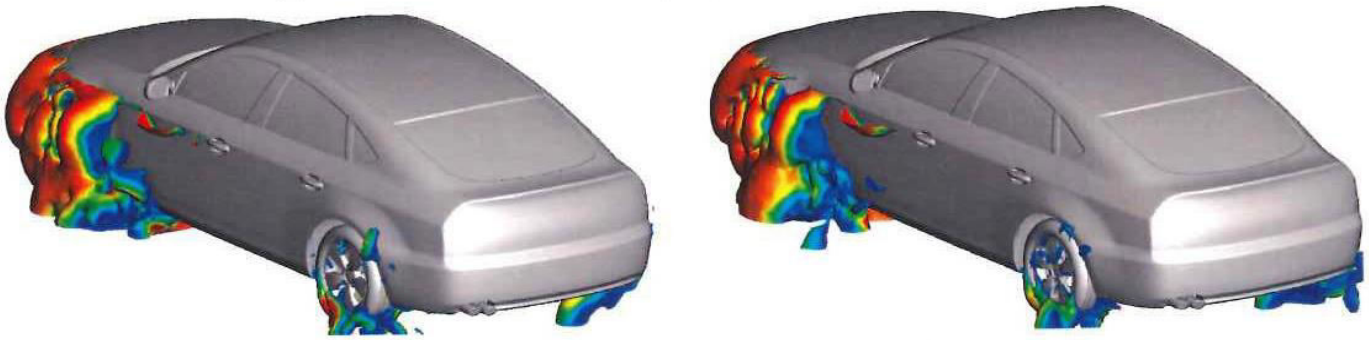

(b) Realistic conditions - MRF(left) and SM(right) methods

Figure 5.8: Pressure coefficient iso-surface of $C_p = -0.45$ with total pressure values highlighting the different features generated by wheel models

To sum up, it has been proven that the MRF and SM methods generate slightly different flow fields with the latter one being the most representative and close-to-reality case. Using the SM technique leads to the fact that the wake of the front wheels is "washed out" propagating away from the car while the turbulent flow is attached to the side of the car in the MRF method. Also, the pressure coefficient distribution at the wheels explains the differences noticed in the body forces. As expected, the flow passes the car slower from the right in the realistic conditions which affect strongly the front wheels but not the rear ones. It is worth noting that the right side is chosen to be presented since flow phenomena are seen easily rather than the other side where the wind causes the turbulent flow to dissipate quickly.

5.6 Cooling Airflow

In this section, a further study is conducted regarding the underhood flows. Firstly, the differences in the drag and lift values are explained in figure 5.9. The drag value of the engine bay has not changed dramatically even though the flow seems to be more turbulent inside the engine bay in the realistic case. The most important aspect however, lies in the fact that this part generate huge amount of negative lift. As seen below, the flow is forced to move upwards by the radiator and engine and thus creating downforce. In the realistic scenario, less flow is passed below the engine and thus a lot more flow moves upwards. This factor causes the difference between the lift values. Finally, it should be mentioned that the velocity magnitude in the radiator is observed at 0.5 m/s approximately.

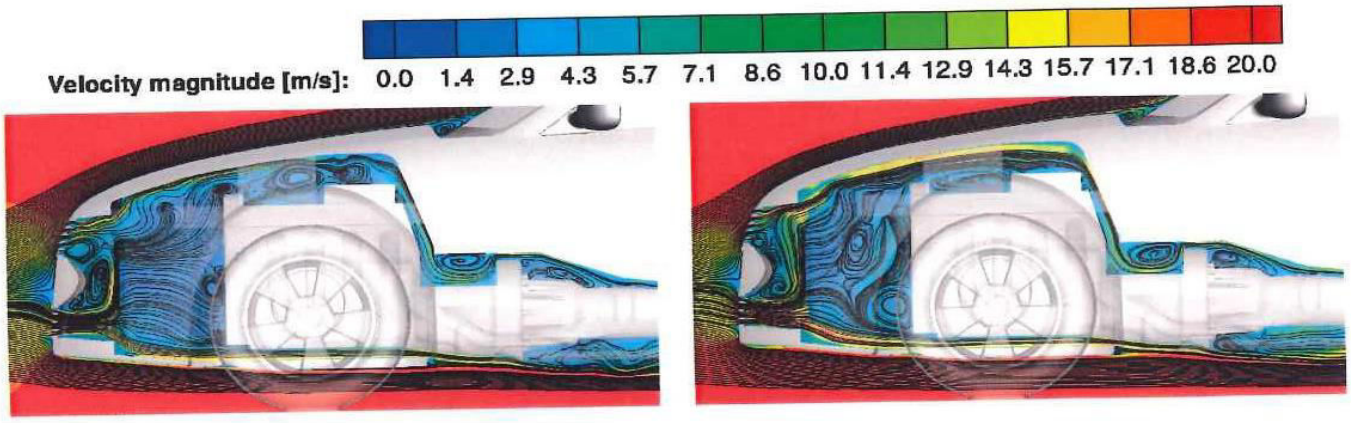

(a) Ideal(left) and realistic(right) scenarios

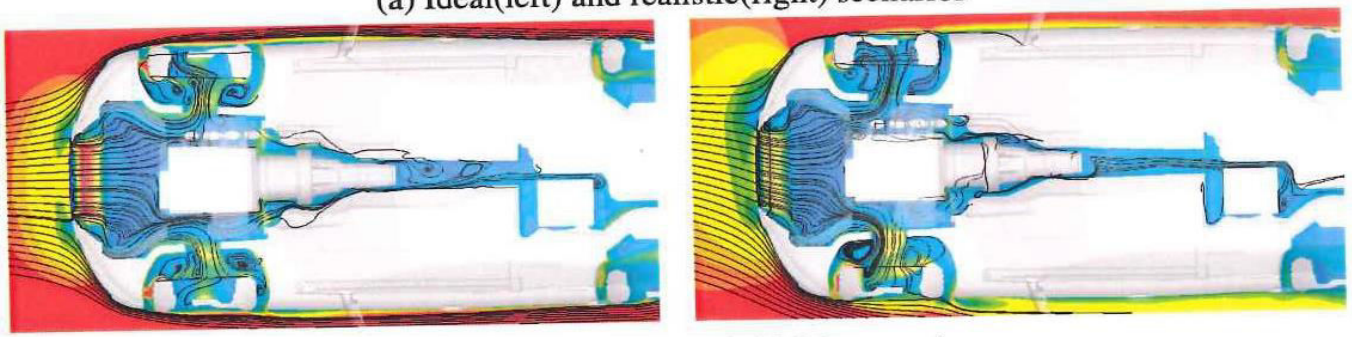

(b) Ideal(left) and realistic(right) scenarios

Figure 5.9: Velocity magnitude at Z=0 and Y=0 slices with streamlines - Flow inside the engine bay indicating the differences between flow conditions

Moreover, the mass flow rate that passes through the engine bay was calculated and results are presented in the following figure. It can be seen that the realistic conditions affect strongly the amount of flow coming out of the engine bay. As previous studies

have proved, more flow goes into the part through the bottom grilles because this part is further in the front. Even more flow passes through the bottom grilles in the realistic case, while an increase of 4% is noticed in the left opening following the direction of the crosswind and explaining the differences noticed in figure 5.8. As expected, less flow comes out from the right opening while in both condition, more than half of the flow passes to the underbody. The SM method is presented in the figure because both models produce similar results.

(a) Wind tunnel scenario

(b) Real-world scenario

Figure 5.10: Percentage values of cooling air split

5.7 Investigation of flow conditions

In this section, the flow field around the car is analysed and differences between the two conditions are highlighted. Firstly, some computational calculations are presented in order to justify the strategy that was followed. Secondly, a comparison analysis is undertaken between the flow conditions presenting the differences obtained at the car's surfaces and flow structures.

Even though the mesh was generated with y^+ calculated to be 1 in the body and 12 in the wheels, the results show that this value is a lot lower. In the rear part of the car, the y^+ is close to 0.1 while only in the mirrors it approaches to 1. The largest area in the wheels has values of y^+ close to 4 and a small region at the front of tyres is noticed to have values around 10.

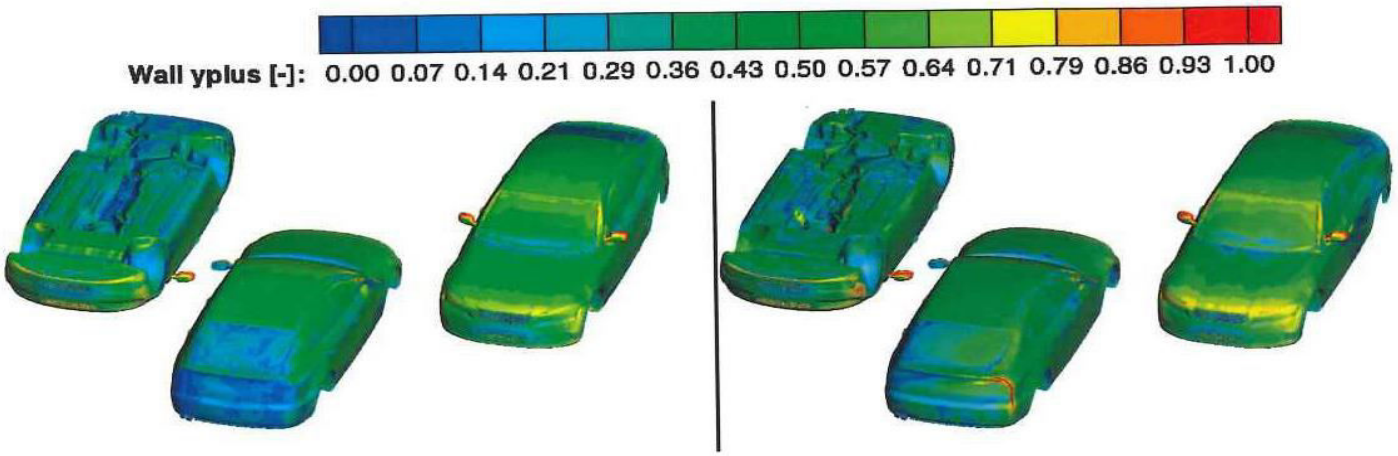

(a) Ideal(left) and realistic(right) scenarios

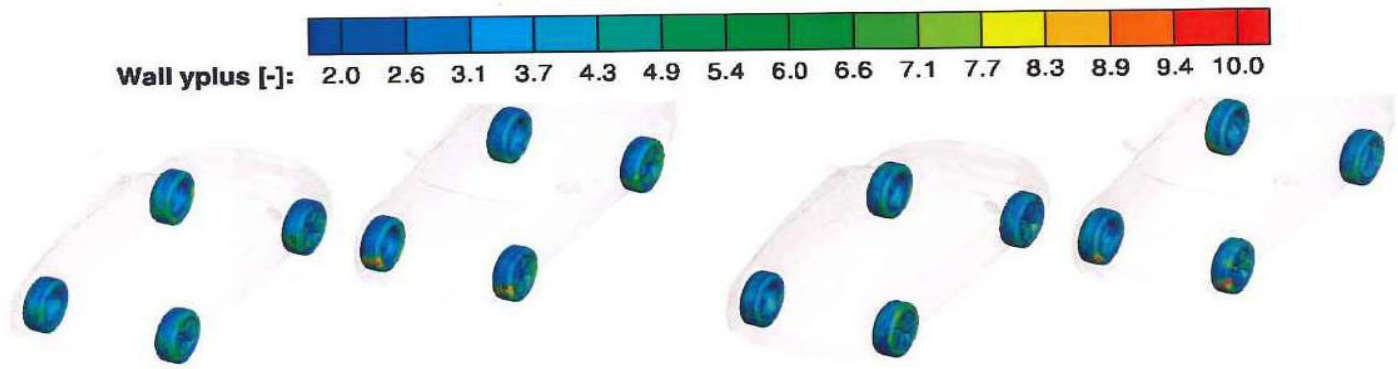

(b) Ideal(left) and realistic(right) scenarios

Figure 5.11: Y^+ distribution in the car and wheels

Since the turbulence intensity has been increased dramatically in real-world conditions, it was considered necessary to obtain the value of the turbulent intensity close to the car. Previous studies have collected results showing that the turbulence intensity had dissipated greatly and a reduced amount reached the car. Figure 5.12 shows the turbulence intensity difference between the two flow conditions. The value of 6.56% was set to the inlet in the realistic conditions and it is seen that the turbulence intensity has dropped

to 5% close to the car. Undoubtedly, the grid affects this value and a higher value would have been obtained if the mesh was finer near the inlet, as has been suggested by previous researchers. Despite that aspect, the difference between the flow conditions is great while an increase is obtained in this value at the wake of the car but only in the ideal case.

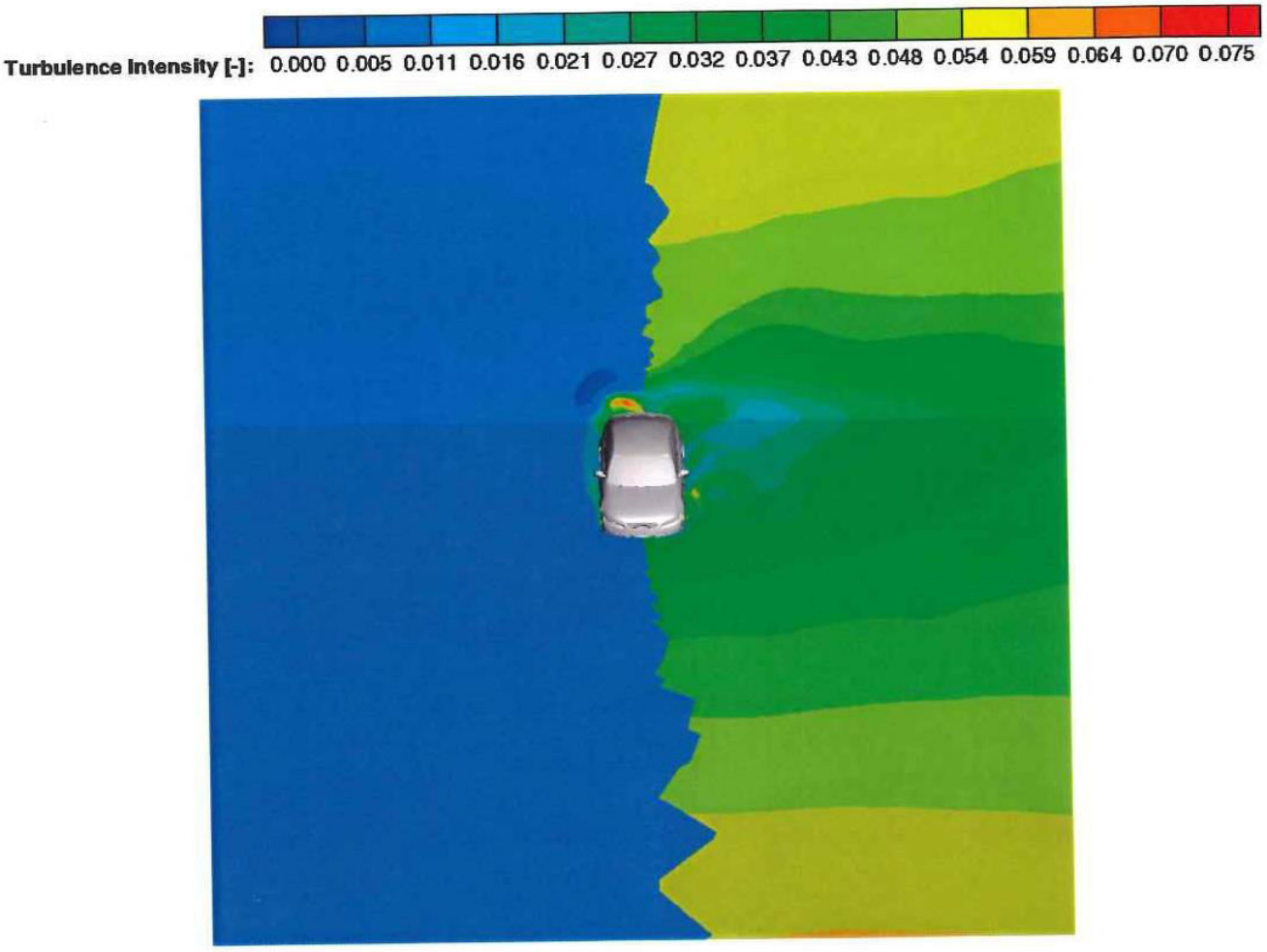

Figure 5.12: Turbulence intensity - Ideal(left) and Realistic(right) scenarios - Comparison between wind tunnel and real-world conditions

The differences between the flow conditions are clearly noticed in the following figure. Since the flow meets the right side first, the pressure in that area is increased while it is decreased on the other side. The wheels seem to be unaffected by the conditions as their rotation is immensely more significant than the rest flow. Also, the wheel models behave similarly at the right side due to the fact that the generated flow fields are greatly disturbed by the crosswind. Flow separation can be detected in the left side at the rear where the wake seems to be propagated in the direction of the wind and thus affects the rear of the car accordingly.

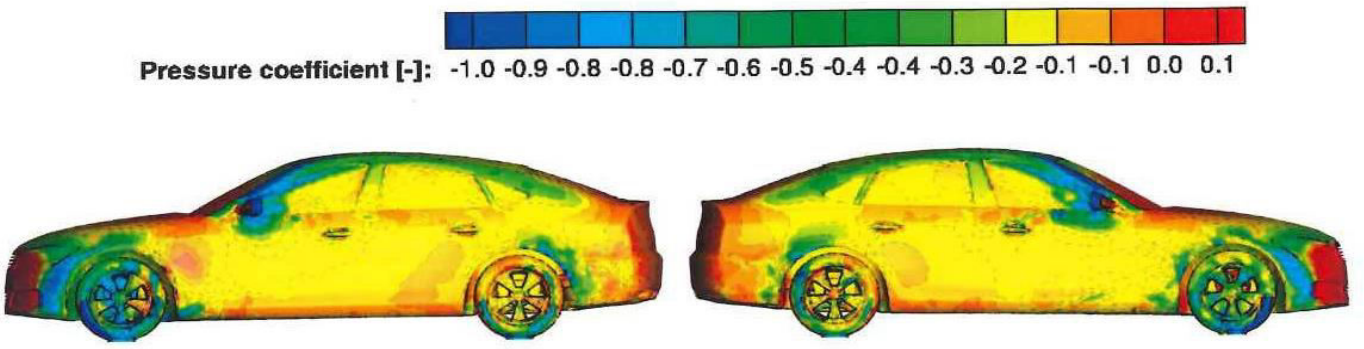

(a) MRF - Ideal conditions

(b) SM - Ideal conditions

(c) MRF - Realistic conditions

(d) SM - Realistic conditions

Figure 5.13: Pressure coefficient distribution on the sides of the car

As seen previously, the flow moves slower at the left side of the car. In order to investigated the differences at the rear of the vehicle, the following figure show the skin friction coefficient of the x component. The rear is affected by the used wheel modelling technique while the flow structures develop differently according to the flow condition. In the ideal case, the A pillar vortices are clearly seen and they are stronger in the SM method. The recirculation of the flow that occurs in the rear window takes is more robust in the SM method while both methods produce similar results in the back of the car.

When realistic conditions are applied, the flow structures have the tendency to follow the direction of the wind. In these conditions, the recirculation area in the rear window is larger with the SM method but it is overall reduced than the ideal case.

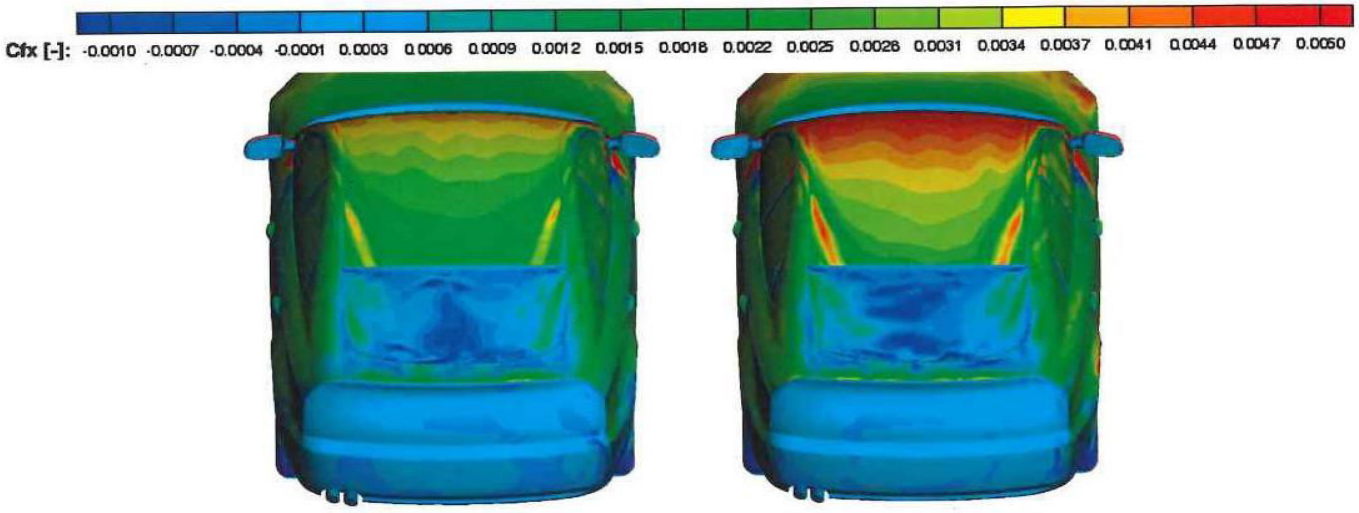

(a) Ideal case - MRF(left) and SM(right) methods

(b) Realistic case - MRF(left) and SM(right) methods

Figure 5.14: Skin friction coefficient using the x component at the rear of the car

The above deductions can also be seen in figure 5.15 where total pressure contours show how the flow structures are propagating. In the ideal scenario, A pillar vortices are formed in the sides of the windscreen and they meet at the rear window. Strong turbulent flow is generated by the mirrors as well and it is propagating to the wake. As mentioned above, the size of the wake of the wheels is affected by the wheel modelling method. In the SM technique, the generated wake from the front wheels propagates away from the car and dissipates while in the MRF method remains attached to the sides and the underbody. On the other hand, the realistic conditions have strongly affected the

generated flow features. In detail, the A pillars do not meet at the rear of the car but they try to move in the direction of the wind. Inevitably, the pressure is higher in the left side of the car while the recirculation area in the rear window is noticed once again but in a smaller lever.

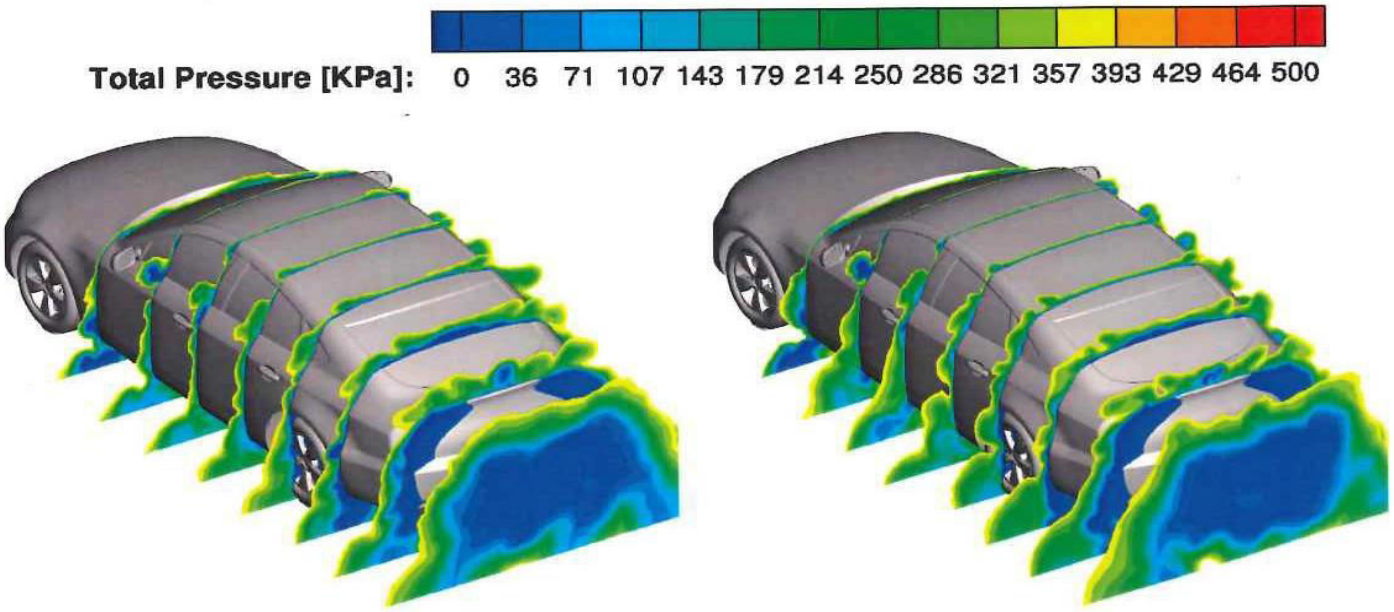

(a) Ideal case - MRF(left) and SM(right) methods

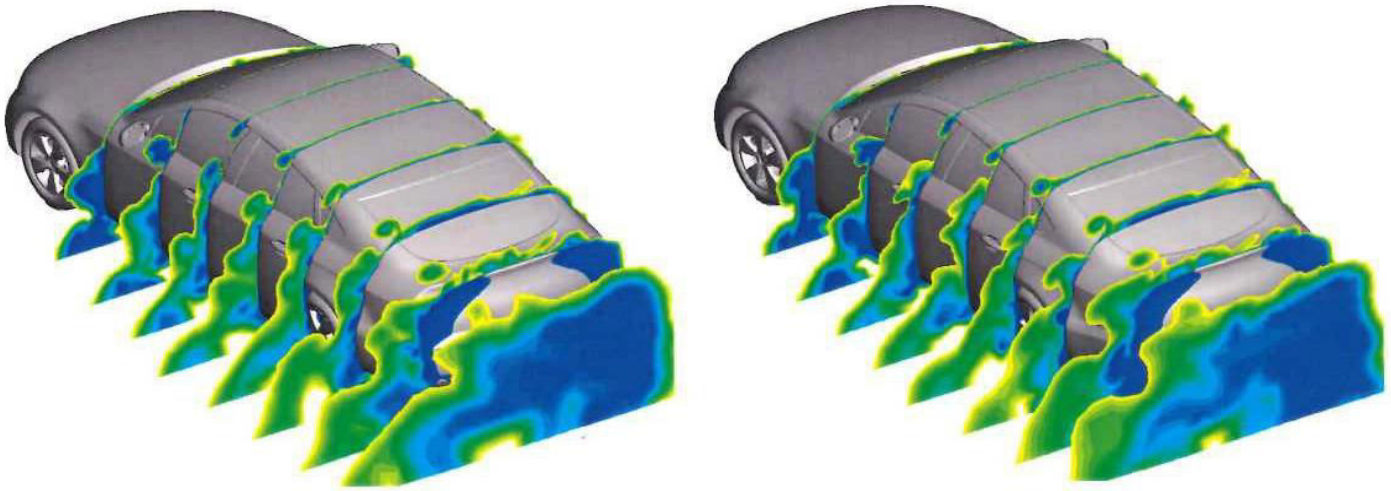

(b) Realistic case - MRF(left) and SM(right) methods

Figure 5.15: Slices in the x axis showing total pressure contours

In the ideal scenario, the flow features resemble the ones from section 2.1.1. In order to obtain the whole picture, the following figure shows the generated flow fields close to the car highlighting the above deductions. Also, the wake is longer in the realistic conditions and it seems that a big anti-clockwise vortex is forming starting from the rear right side.

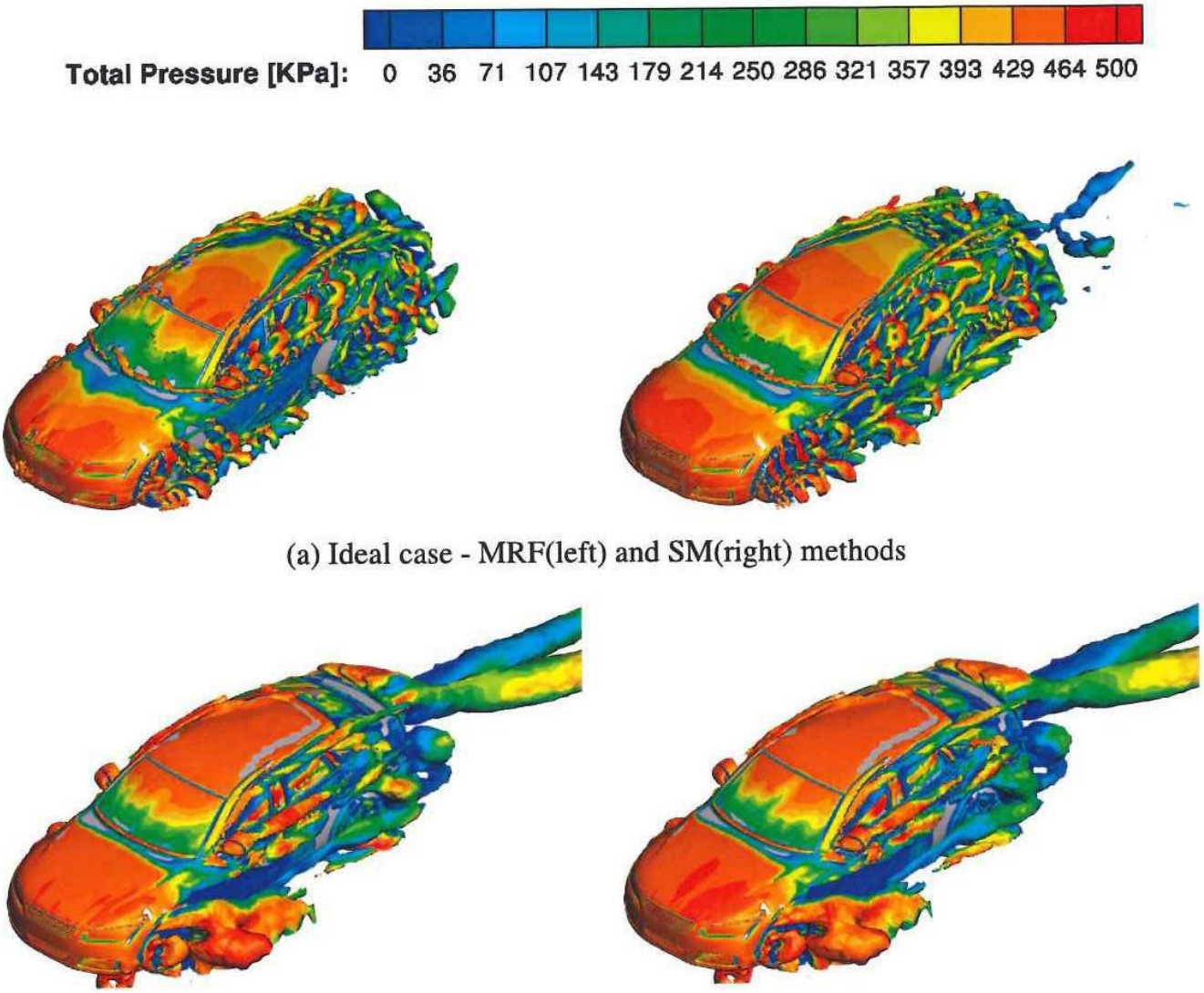

(a) Ideal case - MRF(left) and SM(right) methods

(b) Realistic case - MRF(left) and SM(right) methods

Figure 5.16: Q criterion of 1000 and 100 for ideal and realistic cases respectively showing the flow field close to the car

Finally, the flow features in the wake can be seen in the following figure which helps to identify the propagation of the wake as well as its strength. In the ideal conditions, a symmetric wake is formed which consist of two strong vortices emanating from the A pillar vortices. These vortices are formed 0.5 m approximately behind the car and propagate closer to the ground. In the realistic conditions, the whole wake is moving slightly to the left following the direction of the wind. The two generated vortices are not symmetrical and the right one is more stronger. However, the wake dissipates faster and it is not as strong as the obtained wake in the ideal case.

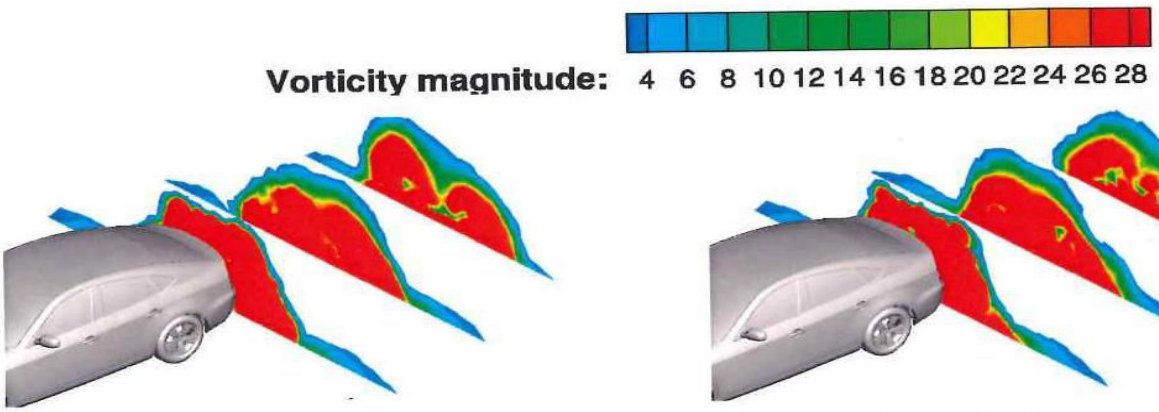

(a) Ideal case - MRF(left) and SM(right) methods

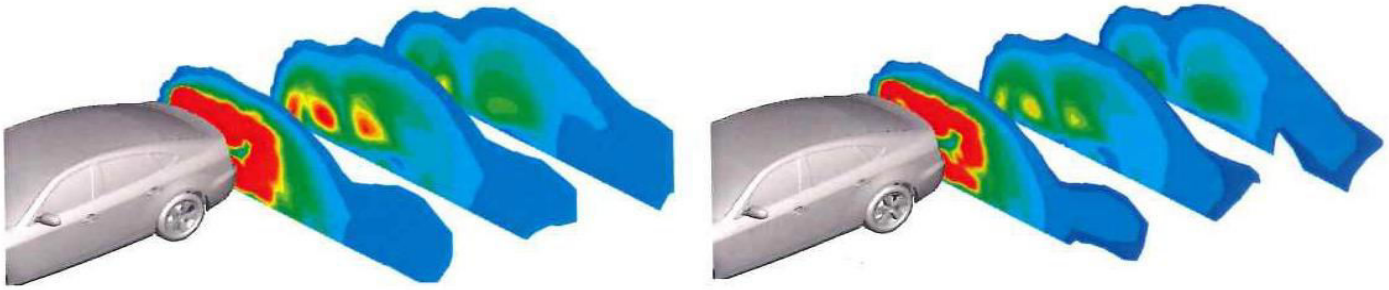

(b) Realistic case - MRF(left) and SM(right) methods

Figure 5.17: Vorticity contours indicating the propagation of the wake

Chapter 6

Conclusions and Future Work

The present work focused on the modelling of the rotating wheels for automotive applications using three models, while investigations regarding the influence of real-world conditions to the overall behavior of the car have been conducted. Transient simulations were undertaken utilizing a scale-resolved scheme (IDDES) for realistic cruise Reynolds number of 8.356×10^6 while the incompressible solver of ANSYS Fluent was used.

Initially, three unstructured grids were generated using the ANSA software. The absence of experimental data means that no errors can be calculated but a Grid Sensitivity Study was conducted to justify that the solution is grid dependent. Firstly, body forces were obtained for all wheel models and flow conditions highlighting the weaknesses of each model. Even though all models predicted drag close, differences are noticed in the lift and the moments. The RWBC produce higher coefficient of moments in the ideal case, while the other two seem to behave similarly. Furthermore, this model is more sensitive to the flow conditions as bigger changes occur. The real-world conditions have strongly affected all parts. The drag was increased by 1/5 approximately while an increase of almost 80% was seen in the lift. Also, since the crosswind results in a 12.26^0 yaw angle, the side force and yaw coefficients have been increased accordingly. As far as the wheels concern, the front right and rear left wheels are significantly influenced by these conditions. Translating these findings to a simpler language, the fuel efficiency is worsened

along with the handling of the vehicle which is the most affected variable.

Forces' distribution was examined since it provides valuable information of how each part affects the overall outcome. As expected, the engine bay and underbody contribute the most to the drag while half of the force comes from the main body and rear end combined. These parts generate the most lift as well but a huge amount of negative lift is generated by the engine bay since the flow is forced to move upwards.

Particular attention was paid to the effect of each wheel model to the overall aerodynamics. Firstly, differences were obtained at the wheels and especially in the rims which rotate in the SM method. The pressure coefficient was lower in some regions of the rims than the MRF method affecting the tyres accordingly. Also, different wakes are generated by the front wheels using each wheel modelling technique and they were detected using the skin friction coefficient and iso-surfaces of pressure coefficient. All in all, the rotation of the rim in the SM method generates turbulent structures which propagate away from the car. On the other hand, the generated flow field using MRF method shows differences and the structures remain attached to the sides of the car and the underbody.

Finally, the influence of the realistic conditions to the already known flow features was examined. Vortices and generally flow structures seem to move in the direction of the wind. The A pillar vortices do not meet in the rear part as in the ideal conditions as they blended in the wake. Also, the wake is weaker and asymmetric in the realistic conditions.

Even though that the investigated wheel modelling techniques have been used widely, the overset mesh has not been tested thoroughly. It is an interesting technique that resolves problems such as the modelling of contact patch. So, it would be exciting to see how this technique behaves compare to the others even though it is known that requires huge computational budget. As far as the flow features generated by the wheels, a frequency analysis can be deducted in order to find the exact location of the vortices and turbulent phenomena produced by each wheel model. Finally, more studies should be involved with real world conditions and influences of light, medium and strong gusts should be

examined.

Bibliography

[1] Morel, Thomas, *Aerodynamic Drag of Bluff Body Shapes Characteristic of Hatch-Back Cars*. 1978 Automotive Engineering Congress and Exposition, SAE International, feb, 1978.

[2] Ahmed, S.R. and Ramm, G. and Faltin, G., *Some salient features of the time-averaged ground vehicle wake*. SAE Technical Papers, 1984, Conference Paper.

[3] Le Good, Geoffrey M. and Garry, Kevin P., *On the Use of Reference Models in Automotive Aerodynamics*. SAE 2004 World Congress and Exhibition, SAE International, mar, 2004.

[4] R. Cooper, Kevin and F. Syms, G and Sovran, G, *Selecting Automotive Diffusers to Maximise Underbody Downforce*. mar, 2000.

[5] Howell, Jeff and Hickman, Derek, *The Influence of Ground Simulation on the Aerodynamics of a Simple Car Model*. SAE International Congress and Exposition, SAE International, feb, 1997.

[6] Garry, K. P. and Cooper, K. R. and Fediw, A. and Wallis, S. B. and Wilsden, D. J., *The Effect on Aerodynamic Drag of the Longitudinal Position of a Road Vehicle Model in a Wind Tunnel Test Section*. International Congress and Exposition, SAE International, mar, 1994.

[7] Carr, G. W. and Stapleford, W. R, *Blockage Effects in Automotive Wind-Tunnel Testing*. SAE International Congress and Exposition, SAE International, mar, 1986.

[8] Cogotti, Antonello, *A Parametric Study on the Ground Effect of a Simplified Car Mode*. International Congress and Exposition, SAE International, feb, 1998.

[9] Heft, Angelina and Indinger, Thomas and Adams, Nikolaus, *Investigation of Unsteady Flow Structures in the Wake of a Realistic Generic Car Mode*. 1978 Automotive Engineering Congress and Exposition, SAE International, jun, 2011.

[10] Heft, Angelina I. and Indinger, Thomas and Adams, Nikolaus A., *Introduction of a New Realistic Generic Car Model for Aerodynamic Investigations*. SAE 2012 World Congress and Exhibition, SAE International, apr, 2012.

[11] Katz, J, *Automotive Aerodynamics*. Automotive Series, SAE International, feb, 2016.

[12] Wong, J.Y., *Theory of Ground Vehicles*. 2008.

[13] Hucho, W.H., *Aerodynamics of Road Vehicles: From Fluid Mechanics to Vehicle Engineering*. 2013.

[14] I. Heft, Angelina and Indinger, Thomas and Adams, Nikolaus, *Experimental and Numerical Investigation of the DrivAer Model*. 1978 Automotive Engineering Congress and Exposition, SAE International, jul, 2012.

[15] MacK, S. and Indinger, T. and Adams, N.A. and Unterlechner, P., *The ground simulation upgrade of the large wind tunnel at the Technische Universitt Mnchen*. SAE Technical Papers, 2012.

[16] Theissen, Pascal and Wojciak, Johannes and Heuler , Kirstin and Demuth, Rainer and Indinger, Thomas and Adams, Nikolaus, *Experimental Investigation of Unsteady Vehicle Aerodynamics under Time-Dependent Flow Conditions - Part 1*. SAE 2011 World Congress and Exhibition, SAE International, apr, 2011.

[17] Wojciak, Johannes and Theissen, Pascal and Heuler, Kirstin and Indinger, Thomas and Adams, Nikolaus and Demuth, Rainer, *Experimental Investigation of Unsteady*

Vehicle Aerodynamics under Time-Dependent Flow Conditions - Part2. SAE 2011 World Congress and Exhibition, SAE International, apr, 2011.

[18] Mack, Steffen and Indinger, Thomas and Adams, Nikolaus and Blume, Stefan and Unterlechner, Peter, *The Interior Design of a 40 Scaled DrivAer Body and First Experimental Results*. SAE International, jun, 2012.

[19] Strangfeld, Christoph and Wieser, Dirk and Schmidt, Hanns-Joachim and Woszidlo, Rene and Nayeri, Christian and Paschereit, Christian, *Experimental Study of Baseline Flow Characteristics for the Realistic Car Model DrivAer*. SAE 2013 World Congress and Exhibition, SAE International, apr, 2013.

[20] Wieser, Dirk and Schmidt, Hanns-Joachim and Mller, Stefan and Strangfeld, Christoph and Nayeri, Christian and Paschereit, Christian, *Experimental Comparison of the Aerodynamic Behavior of Fastback and Notchback DrivAer Models*. SAE International Journal of Passenger Cars - Mechanical Systems, SAE International, apr, 2014.

[21] Wieser, Dirk and Lang, Henning and Nayeri, Christian and Paschereit, Christian, *Manipulation of the Aerodynamic Behavior of the DrivAer Model with Fluidic Oscillators*. SAE International Journal of Passenger Cars - Mechanical Systems, SAE International, apr, 2015.

[22] Miao, L. and Mack, S. and Indinger, T., *Experimental and numerical investigation of automotive aerodynamics using DrivAer model*. Proceedings of the ASME Design Engineering Technical Conference, 2015.

[23] Collin, C. and Mack, S. and Indinger, T. and Mueller, J., *A Numerical and Experimental Evaluation of Open Jet Wind Tunnel Interferences using the DrivAer Reference Model*. SAE International Journal of Passenger Cars - Mechanical Systems, 2016.

[24] Wschle, Alexander, *The Influence of Rotating Wheels on Vehicle Aerodynamics - Numerical and Experimental Investigations*. apr, 2007.

[25] Kandasamy, Satheesh and Duncan, Bradley and Gau, Holger and Maroy, Fabien and Belanger, Alain and Gruen, Norbert and Schufele, Sebastian, *Aerodynamic Performance Assessment of BMW Validation Models using Computational Fluid Dynamics*. SAE 2012 World Congress and Exhibition, SAE International, apr, 2012.

[26] Koitrand, Sofie and Lofdahl, Lennart and Rehnberg, Sven and Gaylard, Adrian, *A Computational Investigation of Ground Simulation for a Saloon Car*. SAE International Journal of Commercial Vehicles, SAE International, apr, 2014.

[27] Yu, Xiaoyan and Jia, Qing and Bao, Di and Yang, Zhigang, *A Comparative Study of Different Wheel Rotating Simulation Methods in Automotive Aerodynamics*. WCX World Congress Experience, SAE International, apr, 2018.

[28] Wittmeier, Felix and Kuthada, Timo, *Open Grille DrivAer Model - First Results*. SAE International Journal of Passenger Cars - Mechanical Systems, SAE International, apr, 2015.

[29] Kuthada, Timo and Wittmeier, Felix and Bock, Benjamin and Schoenleber, Christoph and Link, Alexander, *The Effects of Cooling Air on the Flow Field around a Vehicle*. SAE International Journal of Passenger Cars - Mechanical Systems, SAE International, apr, 2016.

[30] Simmonds, Nicholas and Pitman, John and Tsoutsanis, Panagiotis and Jenkins, Karl and Gaylard, Adrian and Jansen, Wilko, *Complete Body Aerodynamic Study of three Vehicles*. WCX 17: SAE World Congress Experience, SAE International, mar, 2017.

[31] Matsumoto, D. and Haag, L. and Indinger, T., *Investigation of the unsteady external and underhood airflow of the drivaer model by dynamic mode decomposition*

methods. International Journal of Automotive Engineering, SAE International, feb, 2017.

[32] Guilmineau, Emmanuel, *Numerical Simulations of Flow around a Realistic Generic Car Model*. SAE International Journal of Passenger Cars - Mechanical Systems, SAE International, apr, 2014.

[33] Ashton, Neil and Revell, Alistair, *Comparison of RANS and DES Methods for the DrivAer Automotive Body*. SAE 2015 World Congress and Exhibition, SAE International, apr, 2015.

[34] Ashton, Neil and West, *Assessment of RANS and DES methods for realistic automotive models*. Computers and Fluids, 2016.

[35] D. Duncan, Bradley and Fischer, Axel and Kandasamy, Satheesh, *Validation of Lattice-Boltzmann Aerodynamics Simulation for Vehicle Lift Prediction*. 2010.

[36] Cyr, Stephane and Ih, Kang-Duck and Park, Sang-Hyun, *Assessment of RANS and DES methods for realistic automotive models*. SAE 2011 World Congress and Exhibition, SAE International, apr, 2011.

[37] Jakirlic, S. and Kutej, L. and Hanssmann, D. and Basara, B. and Schtz, T. and Tropea, C. *Rear-end shape influence on the aerodynamic properties of a realistic car model: A RANS and hybrid LES/RANS study*. Notes on Numerical Fluid Mechanics and Multidisciplinary Design, 2016.

[38] Jakirlic, Suad and Kutej, Lukas and Hanssmann, Daniel and Basara, Branislav and Tropea, Cameron, *Eddy-resolving Simulations of the Notchback DrivAer Model: Influence of Underbody Geometry and Wheels Rotation on Aerodynamic Behaviour*. SAE 2016 World Congress and Exhibition, SAE International, apr 2016.

[39] D.E. Aljure and J. Calafell and A. Baez and A. Oliva, *Flow over a realistic car model: Wall modeled large eddy simulations assessment and unsteady effects*. Journal of Wind Engineering and Industrial Aerodynamics, 2018.

[40] John, Michael and Buga, Stefan-Daniel and Monti, Indro and Kuthada, Timo and Wittmeier, Felix and Gray, Markus and Laurent, Vincent, *Experimental and Numerical Study of the DrivAer Model Aerodynamics*. apr, 2008.

[41] Peters, Brett C. and Uddin, Mesbah and Bain, Jeremy and Curley, Alex and Henry, Maxwell, *Simulating DrivAer with Structured Finite Difference Overset Grids*. SAE 2015 World Congress and Exhibition, SAE International, apr, 2015.

[42] Forbes, David C. and Page, Gary J. and Passmore, Martin A. and Gaylard, Adrian P., *A Fully Coupled, 6 Degree-of-Freedom, Aerodynamic and Vehicle Handling Crosswind Simulation using the DrivAer Model*. SAE 2015 World Congress and Exhibition, SAE International, apr, 2016.

[43] Gaylard, Adrian P. and Oettle, Nicholas and Gargoloff, Joaquin and Duncan, Bradley, *Evaluation of Non-Uniform Upstream Flow Effects on Vehicle Aerodynamics*. SAE International Journal of Passenger Cars - Mechanical Systems, apr, 2014.

[44] Howell, Jeff and Forbes, David and Passmore, Martin and Page, Gary, *The Effect of a Sheared Crosswind Flow on Car Aerodynamics*. SAE International Journal of Passenger Cars - Mechanical Systems, mar, 2017.

[45] Bradley Duncan and Luca DAlessio and Joaquin Gargoloff and Ales Alajbegovic, *Vehicle aerodynamics impact of on-road turbulence*. Proceedings of the Institution of Mechanical Engineers, Part D: Journal of Automobile Engineering, 2017.

[46] Wendt, J., *Computational Fluid Dynamics: An Introduction*. A von Karman Institute book, 2008.

[47] Toro, E.F., *Riemann Solvers and Numerical Methods for Fluid Dynamics: A Practical Introduction*. Springer Berlin Heidelberg, 2013.

[48] Menter, F.R., *Two-equation eddy-viscosity turbulence models for engineering applications*. AAIAA Journal, 1994.

[49] Spalart, Philippe and Jou, W-H and Strelets, Michael and Allmaras, Steven, *Comments on the Feasibility of LES for Wings, and on a Hybrid RANS/LES Approach*. 1997.

[50] Shur, Michael and Spalart, Philippe and Strelets, Michael and Travin, A, *Detached Eddy Simulation of an Airfoil at High Angle of Attack*. Engineering Turbulence Modelling and Experiments, 1999.

[51] Spalart, P. R. and Deck, S. and Shur, M. L. and Squires, K. D. and Strelets, M. Kh. and Travin, A., *A New Version of Detached-eddy Simulation, Resistant to Ambiguous Grid Densities*. A von Karman Institute book, 2008.

[52] Wendt, J., *A hybrid RANS-LES approach with delayed-DES and wall-modelled LES capabilities*. International Journal of Heat and Fluid Flow, jun, 2008.

[53] Han, Yiyu and Ding, Guohao and He, Yuanyuan and Wu, Jie and le, Jialing, *Assessment of the IDDES method acting as wall-modeled LES in the simulation of spatially developing supersonic flat plate boundary layers*. Engineering Applications of Computational Fluid Mechanics, jun, 2017.

[54] ANSYS Fluent., *Theory Guide*. Release 18.1, ANSYS Inc.

[55] Karamousalidou, A., *WHEEL RIM TYRE CFD MODELLING*. Unpublished, MSc.

[56] Barbaros etin and Kadir G. Guler and Mehmet Haluk Aksel, *Computational Modeling of Vehicle Radiators Using Porous Medium Approach*. Heat Exchangers, IntechOpen, 2017.

[57] Kang, Ning and Mo, Ni Ka and Zheng, Wei Qi, *Three Dimensional Simulation of the Heat Dissipation of an Automotive Radiator Based on Porous Media Method.* International Journal of Heat and Fluid Flow, jun, 2014.

[58] Department for Transport, *Travel time measures for the Strategic Road Network.* Tech. rep, Government of the United Kingdom, London (2017), England: Year EndingMarch 2017.

[59] A. Lapworth, J. McGregor, *Seasonal variation of the prevailing wind direction in Britain.* Weather 63, dec, 2008.

[60] Met Office, *Airfield climate statistics.* https://www.metoffice.gov.uk/aviation/ga/airfield-climate-stats, assessed: 2018-04-26.

[61] Deaves, D.M. and Harris, R.I. and Construction Industry Research and Information Association, *A Mathematical Model of the Structure of Strong Winds.* CIRIA report, 1978.

[62] Roache, P.J., *Verification and Validation in Computational Science and Engineering.* Hermosa, 1998.

[63] Engineering Sciences Data Unit, *Strong Winds in the Atmospheric Boundary Layer.* ESDU series on wind engineering, ESDU International plc, 2008.

[64] Wordley, Scott and Saunders, Jeff, *On-road Turbulence.* SAE International Journal of Passenger Cars - Mechanical Systems, apr, 2008.